A unified SHTC multiphase model of continuum mechanics

Davide Ferrari[1], Ilya Peshkov[1], Evgeniy Romenski[2], and Michael Dumbser[1]

[1]Laboratory of Applied Mathematics, DICAM, University of Trento, via Mesiano 77, 38123 Trento, Italy
[2]Sobolev Institute of Mathematics, 4 Acad. Koptyug avenue, Novosibirsk, Russia

April 2, 2024

The paper is dedicated to the memory of Prof. S.K. Godunov, who made an invaluable contribution to the development of many areas of applied and computational mathematics. The content of this article is largely based on his ideas, which are and will be the basis of research for future generations of mathematicians.

Abstract

In this paper, we present a unified nonequilibrium model of continuum mechanics for compressible multiphase flows. The model, which is formulated within the framework of Symmetric Hyperbolic Thermodynamically Compatible (SHTC) equations, can describe arbitrary number of phases that can be heat conducting *inviscid* and *viscous fluids*, as well as *elasto-plastic solids*. The phases are allowed to have different velocities, pressures, temperatures, and shear stresses, while the material interfaces are treated as diffuse interfaces with the volume fraction playing the role of the interface field. To relate our model to other multiphase approaches, we reformulate the SHTC governing equations in terms of the phase state parameters and put them in the form of Baer-Nunziato-type models. It is the Baer-Nunziato form of the SHTC equations which is then solved numerically using a robust second-order path-conservative MUSCL-Hancock finite volume method on Cartesian meshes. Due to the fact that the obtained governing equations are very challenging we restrict our numerical examples to a simplified version of the model, focusing on the isentropic limit for three-phase mixtures. To address the stiffness properties of the relaxation source terms present in the model, the implemented scheme incorporates a semi-analytical time integration method specifically designed for the non-linear stiff source terms governing the strain relaxation. The validation process involves a wide range of benchmarks and several applications to compressible multiphase problems. Notably, results are presented for multiphase flows in all the relaxation limit cases of the model, including inviscid and viscous Newtonian fluids, as well as non-linear hyperelastic and elastoplastic solids. In all cases, the numerical results demonstrate good agreement with established models, including the Euler or Navier-Stokes equations for fluids and the classical hypo-elastic model with plasticity for solids. Importantly, however, this approach achieves these results within a unified multiphase framework of continuum mechanics.

1 Introduction

In this paper, we further develop the idea of a unified approach to continuum mechanics, which is capable of describing the behavior of all states of matter in a single system of governing equations. Here, we deal with multiphase problems that may include an arbitrary number of phases, such as gases, liquids, and solids and in arbitrary combinations. The approach we chose

Submitted to: *Jounral of Computational Physics*
davide.ferrari@unitn.it, ilya.peshkov@unitn.it, evrom@math.nsc.ru, michael.dumbser@unitn.it

to tackle this problem relies on the continuum mixture theory, which means that all the phases are present in every material volume at all the times [127]. Despite being popular in the fluid mechanics community for many decades now, the mixture approach imposes a big challenge if one tries to generalize it to problems involving the interaction of solids and fluids. The main difficulty is that these two states of matter are generally studied by two distinct communities, using different approaches. And it remained unclear, at least until recently, how to combine these approaches (mathematical models) into a single unified and thremodynamically compatible continuous mixture model.

For example, the Eulerian description of the continuum is the most commonly used to describe the motion of fluids, as they usually undergo large deformations that are not suitable for a Lagrangian description. Instead, in solid mechanics, the Lagrangian description is preferred, which allows very accurate description of the solid body boundaries. Moreover, the fluid and solid mechanics models have different number of degrees of freedom (state variables), e.g. the classical fluid mechanics models do not need to evolve a deformation measure to compute the stress tensor, while the solid mechanics models do. Such incompatibilites in mathematical description have been a major obstacle to the development of a general unified continuum mechanics model for multiphase problems involving fluids and solids. Yet, in some limited cases the mixture theory has been successfully applied to the description of the interaction between fluids and solids, e.g. see [43, 81, 84, 83] and references therein. We also remark that a conventional approach to the description of multiphase flows involving solid-fluid interactions, such as in the Fluid-Structure-Interaction (FSI) problems, is to use a combination of different models, one for each of the phases involved, with additional coupling rules governing the interaction between the different media, and even possibly different numerical schemes and computational meshes for each phase.

In recent years, we have been developing a unified Eulerian model of continuum mechanics [96, 39, 18, 21, 1] that allows to eliminate the mentioned differences between the classical descriptions of fluids and solids. According to this model, a fluid is treated as a special case of an inelastic solid with a severe shear stress relaxation. Therefore, it represents a very solid foundation for building a unified multiphase continuum theory. On the other hand, the unified model belongs to a wider class of equations that we call the Symmetric Hyperbolic Thermodynamically Compatible (SHTC) equations [50, 51, 53, 110, 111, 55, 95]. In particular, the SHTC class includes a multi-fluid model developed by Romenski and co-authors in [109, 108, 104] (the first idea was published in [56, 111]). Therefore, the main motivation for this paper is to combine the two approaches and to develop a unified model of continuum mechanics for multiphase problems with arbitrary composition of the phases that may include inviscid and viscous fluids as well as elastic and inelastic solids. Likewise, to demonstrate the practicality and advantages of such a unified approach for the numerical simulation of fluid-fluid and fluid-structure interaction problems.

It should be noted that despite the long history, the continuous mixture theory still does not have a universally accepted mathematical formulation. It is a hopeless task to try to review all the contributions to the development of the mixture theory, however it worth mentioning the main directions that were taken in order to obtain the balance equations for mixtures to position our approach with respect to the others. One may roughly distinguish three main approaches: the *rational mechanics* approach, *averaging* techniques, and *first-principle*-type approaches. However, let us immediately note that in all these theories, the basic view on the mixture is the same, i.e. the mixture is treated as a system of interpenetrating and interacting continua each of which is described by their own state variables, equations of state, and the evolution of constituents is governed by the phase balance equations similar to that of a single-phase continua but having extra terms describing the interactions between the phases. The main difference between these approaches is the way the balance equations are derived, or more precisely, the way the interaction terms are defined.

The *rational mechanics* approach is a general approach based on some principles mainly put forward by Truesdell, Coleman, and Noll [127, 128, 28], e.g. second law of thermodynamics, objectivity, etc., e.g. see [78]. However, the generality of the approach does not provide specific instructions on how to obtain the balance equations for mixtures in a closed form, i.e. the interaction terms are in general not defined [78, 59, 70, 85, 118, 89, 82, 79]. This explains why closed models can only be found in the literature for application-specific two-phase flows, see e.g. deflagration-to-detonation transition (DDT) in gas-permeable, reactive granular materials [4, 41, 7, 100] and spray modeling [30].

The second approach for the derivation of balance laws for mixtures involves overcoming the discrete nature of the phases that constitute a multiphase mixture through the use of *averaging* techniques. Within averaged approaches, see e.g. [35, 82, 65], the balance equations of each constituent are derived by applying an averaging space and time operation to the equations of motion for different phases separated by interfaces across which the densities, velocities, etc., may jump. The main difficulty of this way of deriving the balance equations is that it is almost impossible to apply in a genuinely multiphysics setting, e.g. mixtures of more than two constituents, different rheology of phases, phase transition, electromagnetic forces (e.g. multispecies plasma), etc.

The third class of mixture theories consists of models whose governing equations can be derived from a first-principle-type approach, e.g. a variational principle (Hamilton's stationary action principle). Indeed, the success of theoretical physics in the twentieth century taught us an important lesson that the most successful theories should admit a variational formulation. However, since we are interested in a macroscopic description of mixtures, such a description is inevitably dissipative, and one cannot expect to derive the full mixture model from a variational principle, but only its non-dissipative, or reversible, part. Therefore, it is crucially important to formulate continuum models in such a way that the reversible and irreversible parts can be clearly separated. This is one of the main ideas behind the theory of Symmetric Hyperbolic Thermodynamically Compatible (SHTC) equations [95] that is used in this paper to obtain the governing equations for multiphase and multilateral flows. In such a theory, the dissipative processes can be formulated only via algebraic (no partial derivatives) relaxation type terms, while the reversible part of SHTC models is presented by the differential part of the time evolution equations. And the latter can be derived from a variational principle. We believe that it is important to have a variational formulation for such complex systems as mixtures, because it allows to couple (define interactions) all parts of the system in a consistent way. It is even more important to have such a formulation in the multiphysics context, where the interactions between the phases are not only mechanical, but also thermal, chemical, electromagnetic, gravitational, etc. It is therefore the main objective of this paper to present a unified model of continuum mechanics for multiphase problems and to test its practicality in numerical simulations of multiphase flows.

Despite being so fundamental in theoretical physics and other branches of continuum mechanics, the variational principle is rarely used to derive governing equations for mixtures. To the best of our knowledge, the few existing variational formulations for mixtures of two fluids were proposed in [48, 57, 95].

We note that there are other first-principle type approaches such as the Hamiltonian formulation of continuum mechanics and non-equilibrium thermodynamics known as GENERIC (General Equations for Reversible-Irreversible Coupling) and put forward by Grmela and Öttinger in [58, 87], see also [90, 95]. Despite the SHTC multiphase models can be also cast into the GENERIC formulation, the GENERIC approach also allows to derive slightly different governing equations for mixtures. A comparison of the two approaches was the subject of [119].

From the numerical view point, compressible multiphase problems also pose a great challenge due to the complexity of the governing equations, various time and length scales, and the presence

of interfaces which require special treatment in many cases. One could divide mesh-based methods into three different families for dealing with multimaterial and multiphase problems: (i) Lagrangian and Arbitrary-Lagrangian-Eulerian (ALE) methods on moving meshes, where free surfaces of the fluid and fluid-fluid or fluid-solid interfaces are accurately resolved by the moving computational grid, see e.g. [71, 16, 69, 14, 10, 46]; (ii) Eulerian methods on fixed meshes with explicit interface reconstruction, such as the volume of fluid method (VOF) originally developed by Hirt and Nichols [62], also see the works of Popinet [99] and Menshov et. al [132, 131, 77] which is also generalized to arbitrary number of immiscible compressible fluids; (iii) Eulerian diffuse interface methods on fixed grids, where the presence of each material is represented by a scalar function, see e.g. [115, 36, 42, 81, 43, 47, 68] and references therein. By its construction, the diffuse interface method is the most natural method to represent interfaces within a continuous mixture model, and it is the method we use in this paper.

In the compressible multiphase community, the Baer-Nunziato (BN) model [4] is one of the most popular mathematical models for describing two-phase flows, and there are many works that solve this model numerically. However, only a very limited number of publications exist on the mathematical and computational issues of BN models for multiphase flows describing *more* than two phases, see e.g. [60, 61, 91]. It is therefore very attractive to demonstrate how the BN-type models can be extended using the SHTC theory to describe nonequilibrium compressible multiphase flows with more than two phases, that could be also solids, and to show how such models can be solved numerically.

Therefore, in this paper we put the SHTC multiphase formulation into a BN-type form. The resulting BN-type model yields a large system of nonlinear Partial Differential Equation (PDE), which includes *highly nonlinear stiff algebraic source terms* as well as *non-conservative* products. The different complexities presented by the PDE system are addressed numerically following a splitting approach, when the homogeneous part of the PDE system is discretized with the aid of a robust second-order explicit MUSCL-Hancock finite volume method on Cartesian meshes[126], combined with a path-conservative technique of Castro and Pares [88, 98] for the treatment of non-conservative products. Because the time scales associated with the relaxation processes are much shorter than those given by the stability condition of the explicit scheme, two different implicit methods are employed to properly treat the relaxation terms. Namely, for the stiff but linear sources related to velocity relaxation, a time integrator based on backward Euler is employed, while the semi-analytical time integration method of Chiocchetti, introduced in [120] for fracture modeling, and further developed in [26, 25, 11], is adopted for the nonlinear stiff source terms governing the relaxation of shear stresses in viscous fluids and plastic solids.

The paper is structured as follows: in Sec. 2 we briefly remind the main features of the SHTC framework, in Sec. 4, we discuss the SHTC formulation for multiphase flows, while the variational derivation is presented in B. Furthermore, in Sec. 5 a BN-form of the SHTC model is presented. Sec. 6 is devoted to the development of a robust numerical scheme capable of addressing the various difficulties inherent in a unified theory of compressible multiphase fluid and solids mechanics. Sec. 7 provides and discusses an extensive collection of numerical experiments, limited to three-phase flows in this paper, with the aim of validating the numerical methods developed in this work, as well as providing some rather unique results related to the behavior of multiphase flows for more than two phases, described through the unified SHTC multiphase model of continuum mechanics. Finally, in Sec. 8 the main achievements of this work are listed and we discuss future research directions regarding numerical algorithms and modelling perspectives within the unified SHTC multiphase model of continuum mechanics.

2 SHTC class of equations

Perhaps, the main challenge in formulating continuum mechanics models for complex phenomena in general and for multiphase flows in particular is associated with the formulation of a closed model that satisfies *a priori* important physical and mathematical properties such as the principles of invariance (Galilean or Lorentz invariance), conservation principle, the principle of causality, the laws of thermodynamics and the possibility of having a well-posed initial value problem (IVP). Methods for constructing equations belonging to the SHTC class allow to build continuum mechanics models that satisfy all these properties. Another general formulation of continuum mechanics that is pursuing the same goals is the Rational Extended Thermodynamics by Müller and Ruggeri [79].

The origin of the SHTC formulation of continuum mechanics can be attributed to the work of Godunov [50], who considered "an interesting class" of nonlinear *overdetermined* conservation laws. In this seminal work, Godunov demonstrated an intricate connection between the *well-posedness* of the IVP for a nonlinear system of conservation laws and principles of thermodynamics. The well-posedness was shown via putting the system into a symmetric hyperbolic quasi-linear form, which was a generalization of Friedrichs' linear symmetric hyperbolic systems [45] to the nonlinear case. That is why we use the name Symmetric Hyperbolic Thermodynamically Compatible systems. However, a very limited number of continuum mechanics models admit a fully conservative formulation (e.g. Euler equations, shallow water equations), which forced Godunov to extend his observations to non-conservative systems such as the ideal magnetohydrodynamics equations [51]. Later, in a series of works [54, 53, 110, 111], Godunov and Romenski extended this idea further and showed that many continuum mechanics models (nonlinear elasticity, binary mixture equations, electrodynamics equations, superfluidity equations, etc.) can be put into an SHTC form. Later, it was also demonstrated that all the SHTC equations admit a variational formulation and can be also viewed as a Hamiltonian formulation of continuum mechanics within the GENERIC framework [95].

As discussed in [53, 95], the SHTC equations have a very peculiar structure, and recently, various numerical schemes were developed to mimic the SHTC structure at the discrete level, see e.g. for a curl-free discretization in [12, 25] and new class of thermodynamically compatible schemes in [20, 21, 19, 1, 125].

In the context of this paper, let us also note that it is possible to formulate a compressible multiphase flow model within the SHTC framework. The seminal ideas about an SHTC theory of mixtures was proposed by Romenski in [110, 111] for the case of two fluids. It was then further developed in a series of works [109, 108, 104] and it was generalized to the case of arbitrary number of constituents in [103]. The SHTC mixture model was already discretized with various numerical schemes, e.g. a MUSCL-Hancock scheme [104, 103], semi-implicit all-Mach number schemes were developed in [74, 73], high-order discontinuous Galerkin and finite-volume schemes in the ADER framework were developed in [102] and a thermodynamically compatible discretization was proposed in [125]. An exact Riemann solver for the barotropic two-fluid SHTC equations was introduced in [124].

An important step in demonstrating the potential of the SHTC theory was done in [96, 39], where the unified model of continuum fluid and solid mechanics within the SHTC framework was proposed, see also its extensions to electrodynamics of moving media [40], non-Newtonian fluids [67, 93], poroelasticity [107, 106], relativistic continuum mechanics [105], flows with surface tension [25, 97]. The mathematical model and its many variants have been referred to differently in these various contexts, from Hyperbolic-Peshkov-Romenski (HPR) or Godunov-Peshkov-Romenski (GPR) in [39, 40, 66] to unified model of continuum mechanics (UMCM) in [11]. In this work, we adopt the generic terminology Unified Continuum Mechanics Model, or when appropriate for brevity UMCM or GPR.

3 Mixture characteristics

3.1 Composition characteristics

We consider a mixture of N constituents which are labeled by Latin indices $a, b, \ldots = 1, \ldots, \mathrm{N}$. Denoting by M and V the total mass and volume of the infinitesimal element of the mixture, respectively, we can write

$$M = \sum_{a=1}^{\mathrm{N}} m_a, \qquad V = \sum_{a=1}^{\mathrm{N}} \nu_a, \tag{1}$$

where m_a is the mass and ν_a is the volume of the a-th constituent in the mixture control volume V. The mixture mass density is then defined as

$$\rho = \frac{M}{V} = \frac{m_1 + m_2 + \ldots + m_{\mathrm{N}}}{V} = \sum_{a=1}^{\mathrm{N}} \varrho_a, \tag{2}$$

where

$$\varrho_a := \frac{m_a}{V} \tag{3}$$

denotes the density of the a-th phase inside the control volume V.

To characterise the volume and mass content of the a-th constituent inside the mixture control volume V, it is also convenient to introduce two non-dimensional scalars: the volume fraction

$$\alpha_a := \frac{\nu_a}{V}, \qquad \sum_{a=1}^{\mathrm{N}} \alpha_a = 1, \tag{4}$$

and the mass fraction

$$c_a := \frac{m_a}{M} = \frac{\varrho_a}{\rho}, \qquad \sum_{a=1}^{\mathrm{N}} c_a = 1. \tag{5}$$

Although ϱ_a represents the true mass density of the a-th constituent inside the control volume V, the equations of state of the constituents are usually given in the single-phase context, i.e. as if the phase a would occupy the entire volume V. Therefore, to use the standard single-phase equations of state, we shall also need the mass density of the a-th phase not of the entire mixture control volume V, but of the partial volume ν_a, i.e.

$$\rho_a = \frac{m_a}{\nu_a} = \frac{m_a V}{\nu_a V} = \frac{\varrho_a}{\alpha_a}. \tag{6}$$

In other words, for phase a, its mass density ρ_a w.r.t. the partial volume ν_a and its mass density ϱ_a w.r.t. the full control volume V are related by

$$\varrho_a = \alpha_a \rho_a. \tag{7}$$

The mixture entropy density $\eta = \rho S$ is defined as

$$\eta := \sum_{a=1}^{\mathrm{N}} \eta_a = \sum_{a=1}^{\mathrm{N}} \varrho_a s_a \tag{8}$$

where s_a is the specific entropy of the a-th phase. Hence, the specific mixture entropy can be computed as

$$S = \frac{\eta}{\rho} = c_1 s_1 + c_2 s_2 + \ldots + c_{\mathrm{N}} s_{\mathrm{N}}. \tag{9}$$

3.2 The kinematic quantities of mixtures

Due to the conservation principle, the total momentum of a control volume is defined as the sum of the momenta of its parts. Thus the linear momentum $\boldsymbol{U} = \{U_k\}$ of the mixture control volume V, where k denotes the component in space, is defined as the sum of the linear momenta $\boldsymbol{u}_a = \{u_{a,k}\} := \varrho_a \boldsymbol{v}_a$ of the constituents

$$\boldsymbol{U} := \boldsymbol{u}_1 + \boldsymbol{u}_2 + \ldots + \boldsymbol{u}_{\mathrm{N}} = \varrho_1 \boldsymbol{v}_1 + \varrho_2 \boldsymbol{v}_2 + \ldots + \varrho_{\mathrm{N}} \boldsymbol{v}_{\mathrm{N}}, \tag{10}$$

where $\boldsymbol{v}_a = \{v_{a,k}\}$ is the velocity of the a-th phase. The velocity $\boldsymbol{V} = \{V_k\} := \boldsymbol{U}/\rho$ of the mixture control volume is therefore defined as the center of mass velocity

$$\boldsymbol{V} := \frac{\boldsymbol{U}}{\rho} = \frac{\varrho_1 \boldsymbol{v}_1 + \varrho_2 \boldsymbol{v}_2 + \ldots + \varrho_{\mathrm{N}} \boldsymbol{v}_{\mathrm{N}}}{\rho} = c_1 \boldsymbol{v}_1 + c_2 \boldsymbol{v}_2 + \ldots + c_{\mathrm{N}} \boldsymbol{v}_{\mathrm{N}}. \tag{11}$$

For the SHTC formulation of the mixture equations, in addition to the mixture momentum $\boldsymbol{U}$, one also needs the relative velocity $\boldsymbol{w}_a = \{w_{a,k}\}$ fields

$$\boldsymbol{w}_a = \boldsymbol{v}_a - \boldsymbol{v}_{\mathrm{N}}, \qquad w_{a,k} = v_{a,k} - v_{\mathrm{N},k}, \qquad k = 1, \ldots, 3. \tag{12}$$

which are defined with respect to the N-th constituent that can be chosen arbitrarily. Whereas, in order to derive a BN-type formulation it is useful to define the relative velocity with respect to the mixture velocity

$$\bar{\boldsymbol{w}}_a := \boldsymbol{v}_a - \boldsymbol{V}, \qquad \bar{w}_{a,k} = v_{a,k} - V_k, \qquad k = 1, \ldots, 3. \tag{13}$$

In the SHTC theory, the relative velocity $\boldsymbol{w}_a$ is the preferred choice because it is dictated by the variational formulation as well as by the systematization of the governing equations.

3.3 Deformation characteristics

In order to describe the elastic and inelastic deformations of a single material in the SHTC framework, one needs to introduce the concept of the *distortion field* $\boldsymbol{A}$, by means of which the evolution of elastic and elastoplastic solids and the dynamics of Newtonian and non-Newtonian fluids can be formulated in the SHTC formalism [55, 96, 92, 67, 93]. In the classical formulation of ideal elastic solids the distortion matrix is interpreted as the inverse of the *deformation gradient tensor*, commonly denoted in the literature as $\boldsymbol{F} = \partial \boldsymbol{x}/\partial \boldsymbol{X}$, or, in index notations $F_{iK} = \partial x_i/\partial X_K$, and hence, $\boldsymbol{A} = \partial \boldsymbol{X}/\partial \boldsymbol{x}$ or $A_{Ki} = \partial X_K/\partial x_i$, for the dynamics of pure elastic solids. Here, as usual, we denote the coordinates of the reference configuration by $\mathbf{X}$ and the coordinates in the current configuration by $\mathbf{x}$. In the case of inelastic deformations (viscous flows, plastic deformations), the distortion field can be interpreted as the inverse of the elastic part $\boldsymbol{F}^{\mathrm{e}}$ of the multiplicative decomposition $\boldsymbol{F} = \boldsymbol{F}^{\mathrm{e}}\boldsymbol{F}^{\mathrm{i}}$ of the deformation gradient into elastic and inelastic part, e.g. see [96, 92]. Note that in the notation of the distortion matrix entries, we distinguish between the Eulerian (lowercase) index i, j, k and the Lagrangian (uppercase) index I, J, K so that the distortion matrix can be seen as a triad of three basis vectors $\boldsymbol{A} = \{\boldsymbol{A}_1, \boldsymbol{A}_2, \boldsymbol{A}_3\}$, where for each $K = 1, 2, 3$, $\boldsymbol{A}_K$ is a 3-vector $\boldsymbol{A}_K = (A_{K1}, A_{K2}, A_{K3})$.

In the general setting, a multiphase medium in the SHTC framework should have multiple distortion fields $\boldsymbol{A}_a$, $a = 1, 2, \ldots, \mathrm{N}$. However, a rigorous derivation of such a model from the variational principle remains beyond our reach, even for the case of a mixture of ideal elastic solids. Therefore, following [107, 106], we present a simplified multiphase model with a single distortion field $\boldsymbol{A}_1 = \boldsymbol{A}_2 = \ldots = \boldsymbol{A}_{\mathrm{N}} = \boldsymbol{A}$. For example, a multiphase single-distortion model was

successfully used in [84, 83] for transient shock-dominated problems in 1D as well in multiple space dimensions. Yet, from our computational experience with the model, especially for the problems with moderate Mach numbers, it has appeared that it is beneficial to evolve individual distortions for every phase. While a rigorous theoretical derivation of the multi-distortion model is still absent, we shall use it in the numerical experiments in Sec.7.

3.4 Heat conduction characteristics

To account for the heat conduction within the SHTC theory, it is necessary to consider another vector field, usually referred to as the thermal impulse. Thus, for each phase, we introduce the vector fields $\boldsymbol{J}_1, \boldsymbol{J}_2, \ldots, \boldsymbol{J}_{\mathrm{N}}$ that characterize the direction and intensity of the heat transfer in each phase.

3.5 SHTC state variables for multiphase flows

Here, we list the set of SHTC state variables for mixtures which are partly different from the conventionally used state variables, for example, in the BN-type formulations, e.g. mixture momentum and relative velocities $\{\boldsymbol{U}, \boldsymbol{w}_a\}$, $a = 1, \ldots, \mathrm{N}-1$ in the SHTC formulation versus phase momenta $\boldsymbol{u}_a$, $a = 1, \ldots, \mathrm{N}$ in the BN-type formulations. The SHTC choice is conditioned by the variational nature of the equations and their symmetrization procedure. Thus, the vector of sought conservative SHTC variables is

$$\mathbf{Q} = (\boldsymbol{U}, \boldsymbol{A}, \rho, \varrho_1, \ldots, \varrho_{\mathrm{N}-1}, \boldsymbol{w}_1, \ldots, \boldsymbol{w}_{\mathrm{N}-1}, \eta_1, \ldots, \eta_{\mathrm{N}}, \boldsymbol{J}_1, \ldots, \boldsymbol{J}_{\mathrm{N}}, \varphi_1, \ldots, \varphi_{\mathrm{N}-1})^T, \tag{14}$$

which is related to the vector of primitive SHTC variables

$$\mathbf{P} = (\boldsymbol{V}, \boldsymbol{A}, \rho, c_1, \ldots, c_{\mathrm{N}-1}, \boldsymbol{w}_1, \ldots, \boldsymbol{w}_{\mathrm{N}-1}, s_1, \ldots, s_{\mathrm{N}}, \boldsymbol{J}_1, \ldots, \boldsymbol{J}_{\mathrm{N}}, \alpha_1, \ldots, \alpha_{\mathrm{N}-1})^T, \tag{15}$$

as

$$\varphi_a = \rho\alpha_a, \qquad \boldsymbol{U} = \rho\boldsymbol{V}, \qquad \varrho_a = \rho c_a \qquad \eta_a = \rho c_a s_a. \tag{16}$$

One should pay attention to that φ_{N}, ϱ_{N}, and $\boldsymbol{w}_{\mathrm{N}}$ are excluded from the set of state variables because they can be expressed as

$$\varphi_{\mathrm{N}} = \rho - \varphi_1 - \ldots - \varphi_{\mathrm{N}-1}, \qquad \varrho_{\mathrm{N}} = \rho - \varrho_1 - \ldots - \varrho_{\mathrm{N}-1}, \qquad \boldsymbol{w}_{\mathrm{N}} = 0, \tag{17}$$

likewise their primitive counterparts

$$\alpha_{\mathrm{N}} = 1 - \alpha_1 - \ldots - \alpha_{\mathrm{N}-1}, \qquad c_{\mathrm{N}} = 1 - c_1 - \ldots - c_{\mathrm{N}-1}, \qquad \boldsymbol{w}_{\mathrm{N}} = 0. \tag{18}$$

4 SHTC governing equations for multiphase flows

The SHTC equations for two-fluid mixtures were proposed by Romenski in [110, 111] (and later developed in [108, 108, 104]) based on the special structure of the SHTC class of equations proposed in [54, 53]. A variational formulation of the SHTC two-fluid model was discussed in [95], and its extension to the case of arbitrary number of fluid phases was presented in [103], and extension to the case of mixtures of solid-fluid mixtures in the context of flows in porous media was given in [107, 106].

In this section, we recall the single-distortion two-phase model [103, 107, 106] and extend it to the setting of an arbitrary number of fluid and solid constituents. We also give its variational formulation in B. We then generalize the single-distortion model to a multi-distortion multiphase

model whose rigorous theoretical derivation from a variational principle is still lacking and will be subject of future research.

Moreover, in this work, the SHTC multiphase model is extended with the additional physical effects such as heat conduction, viscosity of the fluid constituents, and plasticity of the solid ones. Specifically, in this generalization of the SHTC mixture theory, the viscosity and plasticity are incorporated via the unified hyperbolic model of continuum mechanics [55, 96, 39], and the heat conduction is modeled via the hyperbolic heat equations [76, 12, 105], and thus retaining the first-order hyperbolic form of the equations.

4.1 Non-dissipative multiphase single-distortion model

Ignoring for the moment all the dissipative processes, the single-distortion multiphase SHTC model reads (summation over repeated spatial $i, k, \ldots = 1, 2, 3$ and phase $a, b = 1, 2, \ldots, \mathrm{N}$ indices is implied)

$$\frac{\partial U_i}{\partial t} + \frac{\partial \left(U_i V_k + P\delta_{ik} + A_{Jk}\mathcal{E}_{A_{Ji}} + w_{a,i}\mathcal{E}_{w_{a,k}} + J_{a,i}\mathcal{E}_{J_{a,k}} \right)}{\partial x_k} = 0, \tag{19a}$$

$$\frac{\partial A_{Jk}}{\partial t} + \frac{\partial A_{Jl} V_l}{\partial x_k} + V_i \left(\frac{\partial A_{Jk}}{\partial x_i} - \frac{\partial A_{Ji}}{\partial x_k} \right) = 0, \tag{19b}$$

$$\frac{\partial \varrho_a}{\partial t} + \frac{\partial \left(\varrho_a V_k + \mathcal{E}_{w_{a,k}} \right)}{\partial x_k} = 0, \qquad a{=}1, \ldots, \mathrm{N}{-}1, \tag{19c}$$

$$\frac{\partial w_{a,k}}{\partial t} + \frac{\partial \left(w_{a,l} V_l + \mathcal{E}_{\varrho_a} \right)}{\partial x_k} + V_i \left(\frac{\partial w_{a,k}}{\partial x_i} - \frac{\partial w_{a,i}}{\partial x_k} \right) = 0, \qquad a{=}1, \ldots, \mathrm{N}{-}1, \tag{19d}$$

$$\frac{\partial \eta_a}{\partial t} + \frac{\partial \left(\eta_a V_k + \mathcal{E}_{J_{a,k}} \right)}{\partial x_k} = 0, \qquad a{=}1, \ldots, \mathrm{N}, \tag{19e}$$

$$\frac{\partial J_{a,k}}{\partial t} + \frac{\partial \left(J_{a,l} V_l + \mathcal{E}_{\eta_a} \right)}{\partial x_k} + V_i \left(\frac{\partial J_{a,k}}{\partial x_i} - \frac{\partial J_{a,i}}{\partial x_k} \right) = 0, \qquad a{=}1, \ldots, \mathrm{N}, \tag{19f}$$

$$\frac{\partial \rho}{\partial t} + \frac{\partial \left(\rho V_k \right)}{\partial x_k} = 0, \tag{19g}$$

$$\frac{\partial \varphi_a}{\partial t} + \frac{\partial \left(\varphi_a V_k \right)}{\partial x_k} = 0, \qquad a{=}1, \ldots, \mathrm{N}{-}1, \tag{19h}$$

where

$$P(\mathbf{Q}) := U_i \mathcal{E}_{U_i} + \rho \mathcal{E}_\rho + \varrho_a \mathcal{E}_{\varrho_a} + \eta_a \mathcal{E}_{\eta_a} + \varphi_a \mathcal{E}_{\varphi_a} - \mathcal{E} \tag{20}$$

is the total thermodynamic mixture pressure. We note that, as usual, the thermodynamic pressure P accounts only for contributions from the internal energies of the constituents (see (40)–(43)), and, in general, is different from the total mechanical pressure.

As one can see, the fluxes (19a), (19c), and (19e) are defined in terms of the derivatives of the energy potential $\mathcal{E}(\mathbf{Q})$ with respect to the state vector $\mathbf{Q}$. Hence, to complete the model formulation, one needs to specify the energy and compute all the derivatives $\partial\mathcal{E}/\partial\mathbf{Q} = (\mathcal{E}_{U_i}, \mathcal{E}_{A_{Ji}}, \mathcal{E}_\rho, \mathcal{E}_{\varrho_a}, \mathcal{E}_{w_{ak}}, \mathcal{E}_{\eta_a}, \mathcal{E}_{\boldsymbol{J}_a}, \mathcal{E}_{\varphi_a})$, which we do in the following section.

4.2 Closure relations

In this section, we summarize all the formulas for partial derivatives of the energy potential required in the formulation of the SHTC multiphase model.

According to the principle of energy conservation, the total energy density $\mathcal{E}$ of the mixture, in the control volume V, can be defined as the sum of the energy densities $\mathcal{E}_a = \varepsilon_a^{\mathrm{i}} + \varepsilon_a^{\mathrm{e}} + \varepsilon_a^{\mathrm{t}} + \varepsilon_a^{\mathrm{k}}$ of its constituents

$$\mathcal{E}(\mathbf{Q}) = \sum_{a=1}^{\mathrm{N}} \mathcal{E}_a, \tag{21}$$

where, for each phase $a = 1, 2, \ldots, \mathrm{N}$, $\varepsilon_a^{\mathrm{i}}(\rho, \varrho_a, \varphi_a, \eta_a)$ is the internal energy, $\varepsilon_a^{\mathrm{e}}(\varrho_a, \boldsymbol{A})$ is the elastic energy, $\varepsilon_a^{\mathrm{t}}(\varrho_a, \boldsymbol{J}_a)$ is the energy associated to the thermal impulse, and $\varepsilon_a^{\mathrm{k}}(\varrho_a, \boldsymbol{u}_a)$ is the kinetic energy.

4.2.1 Internal energy, ε^{i}

The SHTC state variables (14) are dictated by the variational formulation of the governing equations. However, these might be not the optimal choice of variables when it comes to expressing the fluxes in terms of the conventional fluid characteristics such as pressure, temperature, etc. Therefore, it is useful to express the total energy density of the mixture through two parametrizations. The first one is in terms of the state vector $\mathbf{Q}$ in (14), and the second one in terms of the individual phase state parameters ρ_a and s_a. The latter, only concerns the internal energies $\varepsilon_a^{\mathrm{i}}$. Thus, we shall use the following notations

$$\varepsilon_a^{\mathrm{i}}(\rho, \varrho_a, \varphi_a, \eta_a) = \hat{\varepsilon}_a^{\mathrm{i}}(\rho_a, s_a) = \varrho_a \hat{e}_a^{\mathrm{i}}(\rho_a, s_a) = \varrho_a \hat{e}_a^{\mathrm{i}}\left(\frac{\varrho_a \rho}{\varphi_a}, \frac{\eta_a}{\varrho_a}\right), \qquad a = 1, 2, \ldots, \mathrm{N}-1 \tag{22}$$

and for $a = \mathrm{N}$

$$\hat{\varepsilon}_{\mathrm{N}}^{\mathrm{i}}(\rho_{\mathrm{N}}, s_{\mathrm{N}}) = \left(\rho - \sum_{a=1}^{\mathrm{N}-1} \varrho_a\right) \hat{e}_{\mathrm{N}}^{\mathrm{i}}\left(\frac{\rho\left(\rho - \sum_{a=1}^{\mathrm{N}-1} \varrho_a\right)}{\rho - \sum_{a=1}^{\mathrm{N}-1} \varphi_a}, \frac{\eta_{\mathrm{N}}}{\rho - \sum_{a=1}^{\mathrm{N}-1} \varrho_a}\right). \tag{23}$$

With this parametrization of the internal energies, the phase pressures and temperatures are defined as

$$p_a := \rho_a^2 \frac{\partial \hat{e}_a^{\mathrm{i}}}{\partial \rho_a}, \qquad T_a := \frac{\partial \hat{e}_a^{\mathrm{i}}}{\partial s_a}. \tag{24}$$

In this work, several test problems for multiphase flows of interacting gases, liquids, and solids will be presented. Each of these states of matter has its own equation of state which are described below. We remark that it is not the goal of the paper to provide a comprehensive list of equations of state for all possible materials, but rather to illustrate the flexibility of the SHTC model in handling different types of materials.

- For the gas phases, the equation of state of perfect gases is used in the form

$$\hat{e}_a^{\mathrm{i}}(\rho_a, s_a) = \frac{\mathrm{Co}_a^2}{\gamma_a(\gamma_a - 1)} \left(\frac{\rho_a}{\rho \mathrm{o}_a}\right)^{\gamma_a - 1} e^{s_a/\mathrm{Cv}_a}, \tag{25}$$

  where $\rho \mathrm{o}_a$ is the reference density, γ_a is the adiabatic exponent, Co_a is the velocity of sound at normal atmospheric conditions, Cv_a is the specific heat capacity at constant volume. Then, according to (24), the pressure and temperature are computed as

$$p_a = \rho_a^2 \frac{\partial \hat{e}_a}{\partial \rho_a} = \frac{\rho \mathrm{o}_a \mathrm{Co}_a^2}{\gamma_a} \left(\frac{\rho_a}{\rho \mathrm{o}_a}\right)^{\gamma_a} e^{s_a/\mathrm{Cv}_a}, \tag{26}$$

$$T_a = \frac{\partial \hat{e}_a}{\partial s_a} = \frac{\mathrm{Co}_a^2}{\mathrm{Cv}_a \gamma_a (\gamma_a - 1)} \left(\frac{\rho_a}{\rho \mathrm{o}_a} \right)^{\gamma_a - 1} e^{s_a / \mathrm{Cv}_a}, \tag{27}$$

and the phase velocity of sound C_a can be computed as

$$\mathrm{C}_a^2 := \frac{\partial p_a}{\partial \rho_a} = \mathrm{Co}_a^2 \left(\frac{\rho_a}{\rho \mathrm{o}_a} \right)^{\gamma_a - 1} e^{s_a / \mathrm{Cv}_a}. \tag{28}$$

- For the liquid and solid phases, the stiffened gas equation of state will be used in the form

$$\hat{e}_a^{\mathrm{i}}(\rho_a, s_a) = \frac{\mathrm{Co}_a^2}{\gamma_a (\gamma_a - 1)} \left(\frac{\rho_a}{\rho \mathrm{o}_a} \right)^{\gamma_a - 1} e^{s_a / \mathrm{Cv}_a} + \frac{\rho \mathrm{o}_a \mathrm{Co}_a^2 - \gamma_a p \mathrm{o}_a}{\gamma_a \rho_a}, \tag{29}$$

denoting with $p\mathrm{o}_a$ the reference (atmospheric) pressure. In this case, the pressure and temperature are given by

$$p_a = \rho_a^2 \frac{\partial \hat{e}_a}{\partial \rho_a} = \frac{\rho \mathrm{o}_a \mathrm{Co}_a^2}{\gamma_a} \left(\frac{\rho_a}{\rho \mathrm{o}_a} \right)^{\gamma_a} e^{s_a / \mathrm{Cv}_a} - \frac{\rho \mathrm{o}_a \mathrm{Co}_a^2 - \gamma_a p_{0a}}{\gamma_a}, \tag{30}$$

$$T_a = \frac{\partial \hat{e}_a}{\partial s_a} = \frac{\mathrm{Co}_a^2}{\mathrm{Cv}_a \gamma_a (\gamma_a - 1)} \left(\frac{\rho_a}{\rho \mathrm{o}_a} \right)^{\gamma_a - 1} e^{s_a / \mathrm{Cv}_a} \tag{31}$$

and the phase adiabatic sound speed C_a results in

$$\mathrm{C}_a^2 := \frac{\partial p_a}{\partial \rho_a} = \mathrm{Co}_a^2 \left(\frac{\rho_a}{\rho \mathrm{o}_a} \right)^{\gamma_a - 1} e^{s_a / \mathrm{Cv}_a}. \tag{32}$$

4.2.2 Elastic energy, ε^{e}

We recall that according to the unified model of continuum mechanics [96], the Navier-Stokes equations can be considered as a the stiff relaxation limit of the SHTC viscoelastic model [39], and thus, like in elastic solids, their response to shear deformations is characterized by the elastic energy.

In this work, the part of the energy density associated with the elastic-shear stress, ε^{e}, is assumed to be proportional to the second invariant of the deviator $\mathrm{dev} G_{a,ij} = G_{a,ij} - (G_{a,kk}/3)\delta_{ij}$ of the metric tensor of elastic deformations $G_{a,ij} = A_{a,Ji} A_{a,Jj}$, and reads

$$\varepsilon_a^{\mathrm{e}}(\varrho_a, \boldsymbol{A}_a) = \frac{1}{4} \varrho_a \mathrm{Cs}_a^2 \ \left(\mathrm{dev} G_{a,ik} \mathrm{dev} G_{a,ki} \right), \tag{33}$$

where Cs_a is a parameter representing the propagation speed of small-amplitude shear waves in a-th phase, and here it is referred to as *shear sound velocity*.

At the moment, an SHTC formulation for multiphase flows with different distortion fields $\boldsymbol{A}_a$ is unknown, and in the theoretical part, we assume a single-distortion approximation $\boldsymbol{A} = \boldsymbol{A}_1 = \boldsymbol{A}_2 = \ldots = \boldsymbol{A}_{\mathrm{N}}$. In particular, it is unclear with which velocity the individual phase distortion fields $\boldsymbol{A}_a$ should be transported — the mixture or phase velocity. Therefore, our initial intention was to use the single-distortion approximation. However, in numerous numerical experiments, we found out that the single-distortion approximation is not sufficient for obtaining good results in low-Mach problems. Instead, the best results were obtained for the case when the phase distortions $\boldsymbol{A}_a$ are assumed to be different and evolved according to different equations with phase velocities being the transport velocities, see Sec.5.2.

4.2.3 Thermal energy, ε^{t}

The energy associated to the heat conduction can be taken as

$$\varepsilon_a^{\mathrm{t}}(\varrho_a, \boldsymbol{J}_a) = \varrho_a \frac{1}{2}\mathrm{Ch}_a^2 \; J_{a,k} J_{a,k}, \tag{34}$$

where Ch is a parameter representing the propagation of small-amplitude thermal perturbations. Note that one could use other forms for $\varepsilon_a^{\mathrm{t}}$, see e.g. [33]

4.2.4 Kinetic energy, ε^{k}

The phase kinetic energy

$$\varepsilon_a^{\mathrm{k}} = \frac{1}{2\varrho_a}\|\boldsymbol{u}_a\|^2, \tag{35}$$

is defined in terms of the phase momenta $\boldsymbol{u}_a$. However, to compute the partial derivatives $\partial\mathcal{E}/\partial\mathbf{Q}$, after some algebra, it can be also expressed in terms of the SHTC variables $\mathbf{Q}$ as

$$\sum_{a=1}^{\mathrm{N}} \varepsilon_a^{\mathrm{k}} = \frac{1}{2\rho}\sum_{k=1}^{3} U_k^2 + W(\rho, \varrho_1, \ldots, \varrho_{\mathrm{N}-1}, \boldsymbol{w}_1, \ldots, \boldsymbol{w}_{\mathrm{N}-1}) \tag{36}$$

where the kinetic energy of relative motion W is defined as

$$W(\rho, \varrho_1, \ldots, \varrho_{\mathrm{N}-1}, \boldsymbol{w}_a, \ldots, \boldsymbol{w}_{\mathrm{N}-1}) := \frac{1}{2}\sum_{k=1}^{3}\sum_{a=1}^{\mathrm{N}-1} \varrho_a w_{a,k}^2 - \frac{1}{2\rho}\sum_{k=1}^{3}\left(\sum_{a=1}^{\mathrm{N}-1}\varrho_a w_{a,k}\right)^2. \tag{37}$$

4.2.5 Thermodynamic forces

Keping in mind that

$$\varrho_{\mathrm{N}} = \rho - \sum_{a=1}^{\mathrm{N}-1}\varrho_a \quad \text{and} \quad \varphi_{\mathrm{N}} = \rho - \sum_{a=1}^{\mathrm{N}-1}\varphi_a, \tag{38}$$

the partial derivatives of the energy potential $\mathcal{E}$ with respect to the state vector $\mathbf{Q}$ are given by

$$\frac{\partial\mathcal{E}}{\partial U_i} = \frac{1}{\rho}U_i = V_i, \tag{39a}$$

$$\frac{\partial\mathcal{E}}{\partial A_{Jk}} = \sum_{a=1}^{\mathrm{N}}\frac{\partial\varepsilon_a^{\mathrm{e}}}{\partial A_{Jk}} = \sum_{a=1}^{\mathrm{N}}\varrho_a \mathrm{Cs}_a^2 A_{Ji}\mathrm{dev}G_{ik}, \tag{39b}$$

$$\frac{\partial\mathcal{E}}{\partial\rho} = \sum_{a=1}^{\mathrm{N}-1}\frac{\partial\hat{\varepsilon}_a^{\mathrm{i}}}{\partial\rho_a}\frac{\varrho_a}{\varphi_a} + \frac{\partial\hat{\varepsilon}_{\mathrm{N}}^{\mathrm{i}}}{\partial\rho_{\mathrm{N}}}\left(\frac{\rho\varphi_{\mathrm{N}} - \rho\varrho_{\mathrm{N}} + \varrho_{\mathrm{N}}\varphi_{\mathrm{N}}}{\varphi_{\mathrm{N}}^2}\right) - \frac{\partial\hat{\varepsilon}_{\mathrm{N}}^{\mathrm{i}}}{\partial s_{\mathrm{N}}}\frac{\eta_{\mathrm{N}}}{\varrho_{\mathrm{N}}^2} + \frac{\varepsilon_{\mathrm{N}}^{\mathrm{e}}}{\varrho_{\mathrm{N}}} + \frac{\varepsilon_{\mathrm{N}}^{\mathrm{t}}}{\varrho_{\mathrm{N}}} + \tag{39c}$$

$$\frac{1}{2\rho^2}\sum_{k=1}^{3}\sum_{a=1}^{\mathrm{N}}(\varrho_a w_{a,k})^2 - \frac{1}{2\rho^2}\sum_{k=1}^{3}U_k^2, \tag{39d}$$

$$\frac{\partial\mathcal{E}}{\partial\varphi_a} = -\frac{\varrho_a\rho}{\varphi_a^2}\frac{\partial\hat{\varepsilon}_a^{\mathrm{i}}}{\partial\rho_a} + \frac{\varrho_{\mathrm{N}}\rho}{\varphi_{\mathrm{N}}^2}\frac{\partial\hat{\varepsilon}_{\mathrm{N}}^{\mathrm{i}}}{\partial\mathrm{N}} = -\frac{1}{\rho}\left(\rho_a^2\frac{\partial\hat{e}_a}{\partial\rho_a} - \rho_{\mathrm{N}}^2\frac{\partial\hat{e}_{\mathrm{N}}}{\partial\rho_{\mathrm{N}}}\right) = -\frac{p_a - p_{\mathrm{N}}}{\rho}, \qquad a = 1, \ldots, N-1, \tag{39e}$$

$$\frac{\partial \mathcal{E}}{\partial \varrho_a} = \frac{\rho}{\varphi_a}\frac{\partial \hat{\varepsilon}^{\mathrm{i}}_a}{\partial \rho_a} - \frac{\eta_a}{\varrho_a^2}\frac{\partial \hat{\varepsilon}^{\mathrm{i}}_a}{\partial s_a} - \frac{\rho}{\varphi_{\mathrm{N}}}\frac{\partial \hat{\varepsilon}^{\mathrm{i}}_{\mathrm{N}}}{\partial \rho_{\mathrm{N}}} + \frac{\eta_{\mathrm{N}}}{\varrho_{\mathrm{N}}^2}\frac{\partial \hat{\varepsilon}^{\mathrm{i}}_{\mathrm{N}}}{\partial s_{\mathrm{N}}} + \frac{\varepsilon^{\mathrm{e}}_a}{\varrho_a} - \frac{\varepsilon^{\mathrm{e}}_{\mathrm{N}}}{\varrho_{\mathrm{N}}} + \frac{\varepsilon^{\mathrm{t}}_a}{\varrho_a} - \frac{\varepsilon^{\mathrm{t}}_{\mathrm{N}}}{\varrho_{\mathrm{N}}} +$$

$$\frac{1}{2}\sum_{k=1}^{3} w_{a,k}^2 - \frac{1}{\rho}\sum_{k=1}^{3}\sum_{b=1}^{\mathrm{N}-1} \varrho_b w_{b,k} w_{a,k}, \quad a = 1, \ldots, N-1, \tag{39f}$$

$$\frac{\partial \mathcal{E}}{\partial w_{a,k}} = \varrho_a w_{a,k} - \frac{\varrho_a}{\rho}\sum_{b=1}^{\mathrm{N}-1} \varrho_b w_{b,k} = \varrho_a (v_{a,k} - V_k) = \varrho_a \bar{w}_{a,k}, \qquad a = 1, \ldots, N-1, \tag{39g}$$

$$\frac{\partial \mathcal{E}}{\partial \eta_a} = \frac{1}{\varrho_a}\frac{\partial \hat{\varepsilon}^{\mathrm{i}}_a}{\partial s_a} = \frac{\partial \hat{e}^{\mathrm{i}}_a}{\partial s_a} = T_a, \tag{39h}$$

$$\frac{\partial \mathcal{E}}{\partial J_{a,k}} = \frac{\partial \varepsilon^{\mathrm{t}}}{\partial J_{a,k}} = \varrho_a \mathrm{Ch}_a^2 J_{a,k}. \tag{39i}$$

In particular, with formulas (39), one can show that the mixture pressure (20) can be computed as the following sum

$$P = \sum_{a=1}^{\mathrm{N}} \left(\rho_a \frac{\partial \hat{\varepsilon}^{\mathrm{i}}_a}{\partial \rho_a} - \hat{\varepsilon}^{\mathrm{i}}_a \right) \tag{40}$$

which suggests that the quantities

$$P_a := \rho_a \frac{\partial \hat{\varepsilon}^{\mathrm{i}}_a}{\partial \rho_a} - \hat{\varepsilon}^{\mathrm{i}}_a \tag{41}$$

can be called the partial phase pressures. Moreover, due to the fact $\rho_a \frac{\partial \hat{\varepsilon}^{\mathrm{i}}_a}{\partial \rho_a} - \hat{\varepsilon}^{\mathrm{i}}_a = \alpha_a \rho_a^2 \frac{\partial \hat{e}^{\mathrm{i}}_a}{\partial \rho_a}$, the partial phase pressures P_a and the single phase pressures (24) are related by

$$P_a = \alpha_a p_a. \tag{42}$$

In other words, according to the SHTC formulation for multiphase flows, the mixture pressure can be computed as

$$P = P_1 + \ldots + P_{\mathrm{N}} = \alpha_1 p_1 + \ldots + \alpha_{\mathrm{N}} p_{\mathrm{N}}, \tag{43}$$

which is also known as Dalton's law of partial pressures in mixtures.

$$\frac{\partial \mathcal{E}}{\partial \varrho_a} = \mu_a - \mu_{\mathrm{N}} + e^{\mathrm{e}}_a - e^{\mathrm{e}}_{\mathrm{N}} + e^{\mathrm{t}}_a - e^{\mathrm{t}}_{\mathrm{N}} + \sum_{k=1}^{3} w_{a,k}\left(\bar{w}_{a,k} - \frac{1}{2} w_{a,k}\right), \tag{44}$$

where

$$\mu_a := e^{\mathrm{i}}_a + \frac{p_a}{\rho_a} - s_a T_a = \frac{\partial \varepsilon^{\mathrm{i}}_a}{\partial \varrho_a} \tag{45}$$

is the chemical potential of the a-th constituent, and $e^{\mathrm{e}}_a = \varepsilon^{\mathrm{e}}_a / \varrho_a$, $e^{\mathrm{t}}_a = \varepsilon^{\mathrm{t}}_a / \varrho_a$.

4.3 Irreversible dynamics, dissipative processes

In the SHTC theory, a dissipative process is associated with the irreversible part of the time evolution equations that increases the entropy of the system and that is modeled via algebraic relaxation source terms [95]. They are defined in terms of the gradients of the energy $\mathcal{E}_{\mathbf{Q}}$, (i.e. in terms of the conjugate state variables), thus the irreversible part of the SHTC equations can be called the gradient dynamics [95, 90].

The following, at the moment, arbitrary functions of the conjugate state variables

$$Z_{Jk}(\mathcal{E}_{\mathbf{Q}}), \quad \Lambda_{a,k}(\mathcal{E}_{\mathbf{Q}}), \quad \chi_a(\mathcal{E}_{\mathbf{Q}}), \quad \Gamma_{a,k}(\mathcal{E}_{\mathbf{Q}}), \quad \pi_a(\mathcal{E}_{\mathbf{Q}}), \quad \Phi_a(\mathcal{E}_{\mathbf{Q}}), \tag{46}$$

can be added in the right-hand side of the system equations (19)

$$\frac{\partial U_i}{\partial t} + \frac{\partial \left(U_i V_k + P\delta_{ik} + A_{Ji}\mathcal{E}_{A_{Jk}} + w_{a,i}\mathcal{E}_{w_{a,k}} + J_{b,i}\mathcal{E}_{J_{b,k}}\right)}{\partial x_k} = 0, \tag{47a}$$

$$\frac{\partial A_{Jk}}{\partial t} + \frac{\partial A_{Jl}V_l}{\partial x_k} + V_i\left(\frac{\partial A_{Jk}}{\partial x_i} - \frac{\partial A_{Ji}}{\partial x_k}\right) = Z_{Jk}, \tag{47b}$$

$$\frac{\partial \varrho_a}{\partial t} + \frac{\partial \left(\varrho_a V_k + \mathcal{E}_{w_{a,k}}\right)}{\partial x_k} = \chi_a, \qquad a{=}1,\ldots,\mathrm{N}{-}1, \tag{47c}$$

$$\frac{\partial w_{a,k}}{\partial t} + \frac{\partial \left(w_{a,l}V_l + \mathcal{E}_{\varrho_a}\right)}{\partial x_k} + V_i\left(\frac{\partial w_{a,k}}{\partial x_i} - \frac{\partial w_{a,i}}{\partial x_k}\right) = \Lambda_{a,k}, \qquad a{=}1,\ldots,\mathrm{N}{-}1, \tag{47d}$$

$$\frac{\partial \eta_a}{\partial t} + \frac{\partial \left(\eta_a V_k + \mathcal{E}_{J_{a,k}}\right)}{\partial x_k} = \pi_a + \Pi_a, \qquad a{=}1,\ldots,\mathrm{N}, \tag{47e}$$

$$\frac{\partial J_{a,k}}{\partial t} + \frac{\partial \left(J_{a,l}V_l + \mathcal{E}_{\eta_a}\right)}{\partial x_k} + V_i\left(\frac{\partial J_{a,k}}{\partial x_i} - \frac{\partial J_{a,i}}{\partial x_k}\right) = \Gamma_{a,k}, \qquad a{=}1,\ldots,\mathrm{N}, \tag{47f}$$

$$\frac{\partial \rho}{\partial t} + \frac{\partial \left(\rho V_k\right)}{\partial x_k} = 0, \tag{47g}$$

$$\frac{\partial \varphi_a}{\partial t} + \frac{\partial \left(\varphi_a V_k\right)}{\partial x_k} = \Phi_a, \qquad a{=}1,\ldots,\mathrm{N}{-}1, \tag{47h}$$

In what follows, we specify the form of the source terms in (46) for the SHTC mixture model, and explain their physical meaning.

4.3.1 Strain relaxation, Z_{Jk}

The strain relaxation source term Z_{Jk}

$$Z_{Jk} := -\frac{1}{\rho}\Upsilon\mathcal{E}_{A_{Jk}}, \tag{48}$$

where Υ is a positive relaxation scaling function. For the elastic energy chosen in this paper, $\mathcal{E}_{A_{Jk}}$ takes the form

$$\mathcal{E}_{A_{Jk}} = \sum_{a=1}^{\mathrm{N}} \frac{\partial \varepsilon_a^{\mathrm{e}}}{\partial A_{Jk}} = A_{Ji}\mathrm{dev}G_{ik}\sum_{a=1}^{\mathrm{N}}\varrho_a \mathrm{Cs}_a^2 = \rho A_{Ji}\mathrm{dev}G_{ik}\sum_{a=1}^{\mathrm{N}} c_a \mathrm{Cs}_a^2, \quad \Upsilon = \frac{3}{\tau^{\mathrm{e}}}\left(\sum_{a=1}^{\mathrm{N}} c_a \mathrm{Cs}_a^2\right)^{-1}\det(\boldsymbol{A})^{5/3}. \tag{49}$$

The scaling parameter Υ is chosen in such a form so that to respect Newton's law of viscosity with a constant shear viscosity in the limit $\tau^{\mathrm{e}} \to 0$ [96, 39], where τ^{e} is the so-called *strain relaxation time*, which governs the rate at which the strain, in a given control volume, is dissipated. When $\tau^{\mathrm{e}} = 0$, the thermodynamic force $\mathcal{E}_{A_{Jk}}$ vanishes instantaneously ($\mathcal{E}_{A_{Jk}} = 0$) and hence, the shear stress as well $A_{Jk}\mathcal{E}_{A_{Ji}} = 0$, and therefore, inviscid flow is retrieved. On the other hand, for $\tau^{\mathrm{e}} = \infty$ there is no relaxation, and the behavior of a pure elastic solid is retrieved. For intermediate values $0 < \tau^{\mathrm{e}} < \infty$, the medium is neither ideal fluid nor elastic solid, but a viscoelastic material, and with

a proper choice of the function $\tau^{\mathrm{e}}(\mathbf{Q})$ various material responses can be recovered, e.g. Newtonian [96, 39] for $\tau^{\mathrm{e}} = const$ with the kinematic viscosity (for the elastic energy in the form (33))

$$\nu = \frac{1}{6}\mathrm{Cs}^2\tau^{\mathrm{e}}, \tag{50}$$

non-Newtonian fluids [67], viscoplastic Bingham-type fluids [93], elastoplastic solids [55, 92].

4.3.2 Interfacial friction, $\Lambda_{a,k}$, and thermal impulse dissipation, $\Gamma_{a,k}$

The second dissipative process relevant to multiphase flows is the interfacial friction. Accounting for this process results in relaxation of the phase velocities $\boldsymbol{v}_a$ towards a common value, which in turn leads to the relaxation of the relative velocities $\boldsymbol{w}_a$ towards zero.

The relaxation source terms in the thermal impulse equations are introduced to model the heat conduction process within a given phase and between the constituents. It has appeared that to get the heat conducting BN-type model as a relaxation limit of the SHTC multiphase equations, one needs to couple the relaxation of the phase velocities with the relaxation of the thermal impulse. Thus, following [108, 125], the relaxation source terms $\Lambda_{a,k}$ and $\Gamma_{a,k}$ are introduced in the phase velocity and thermal impulse equations, respectively, as

$$\Lambda_{a,k} := -\frac{1}{\rho}\sum_{b=1}^{\mathrm{N}-1}\lambda_{ab,k}\mathcal{E}_{w_{b,k}} - \frac{1}{\rho}\sum_{b=1}^{\mathrm{N}}\zeta_{ab,k}\mathcal{E}_{J_{b,k}}, \qquad \mathcal{E}_{w_{b,k}} = \frac{\partial\mathcal{E}}{\partial w_{b,k}} = \varrho_b(v_{b,k} - V_k), \tag{51a}$$

$$\Gamma_{a,k} := -\frac{1}{\rho}\sum_{b=1}^{\mathrm{N}-1}\zeta_{ba,k}\mathcal{E}_{w_{b,k}} - \frac{1}{\rho}\gamma_{a,k}\mathcal{E}_{J_{a,k}}, \qquad \mathcal{E}_{J_{bk}} = \varrho_b\frac{\partial e_b^{\mathrm{t}}}{\partial J_{b,k}} = \varrho_b\mathrm{Ch}_b^2 J_{b,k}, \tag{51b}$$

where the kinetic coefficients $\lambda_{ab,k} = \lambda_{ab,k}(\mathbf{Q})$ are the entries of three ($k = 1, 2, 3$) symmetric positive semi-definite matrices, and

$$\gamma_{a,k} = \frac{1}{\tau_{a,k}^{\mathrm{t}}\mathrm{Ch}_a^2} \geq 0 \tag{52}$$

where $\tau_{a,k}^{\mathrm{t}}$ are the relaxation time scales governing the heat conduction process within the a-th constituent. Moreover, in accordance with the Onsager principle, we chose the matrices of dissipative kinetic coefficients to be symmetric, for consistency with the first and second laws of thermodynamics, we must require that the following three matrices ($k = 1, 2, 3$)

$$\boldsymbol{\Psi}_k = \begin{pmatrix} \boldsymbol{\lambda}_k & \boldsymbol{\zeta}_k \\ \boldsymbol{\zeta}_k^T & \boldsymbol{\gamma}_k \end{pmatrix} \geq 0, \tag{53}$$

are positive semi-definite, where $\boldsymbol{\lambda}_k$ and $\boldsymbol{\zeta}_k$ are the $(\mathrm{N}-1)\times(\mathrm{N}-1)$ and $(\mathrm{N}-1)\times\mathrm{N}$ matrices with the entries $\lambda_{ab,k}$ and $\zeta_{ab,k}$, respectively, and $\boldsymbol{\gamma}_k$ are the diagonal matrices with the entries $\gamma_{a,k}$ on the diagonal.

4.3.3 Kinetics of phase transformation, χ_a

For the sake of completeness, we also mention how the kinetics of phase transformation can be introduced into the SHTC mixture equations. In order to achieve this, it is necessary to introduce the sources χ_a into the phase mass balance equations, which are defined as

$$\chi_a := -\rho\sum_{b=1}^{\mathrm{N}-1}\chi_{ab}\mathcal{E}_{\varrho_b}, \qquad \sum_{a=1}^{\mathrm{N}}\chi_a = 0, \tag{54}$$

where $\mathcal{E}_{\varrho_a}$ is given in (39f), or (44), and the kinetic coefficients $\chi_{ab} = \chi_{ab}(\mathbf{Q})$ form a symmetric positive semi-definite matrix.

4.3.4 Temperature relaxation, π_a

The source terms π_a in the phase entropy equations are defined as

$$\pi_a := -\varrho_a \frac{\mathcal{E}_{\eta_a} - \sum_{b=1}^{\mathrm{N}} \frac{\varrho_b}{\rho} \mathcal{E}_{\eta_b}}{\tau \mathcal{E}_{\eta_a}} = \varrho_a \frac{T_a - \sum_{b=1}^{\mathrm{N}} c_b T_b}{\tau T_a}, \tag{55}$$

and they model the phase temperature relaxation towards the common temperature

$$T := \sum_{a=1}^{\mathrm{N}} c_a T_a \tag{56}$$

which can be called the temperature of the mixture control volume. Here, $\tau < 0$ is the relaxation parameter that characterizes the rate at which the temperature equilibrium $T_1 = \ldots = T_{\mathrm{N}} = T$ is approached by the system.

4.3.5 Pressure relaxation, Φ_a

Finally, the dissipative process related to the pressure relaxation towards a common pressure are introduced as source terms in the volume fraction balance laws of the phases by the functions

$$\Phi_a := -\rho \sum_{b=1}^{\mathrm{N}-1} \varphi_{ab} \mathcal{E}_{\varphi_b}, \qquad \mathcal{E}_{\varphi_a} = \frac{\partial \mathcal{E}}{\partial \varphi_a} = -\frac{p_a - p_{\mathrm{N}}}{\rho}, \tag{57}$$

where $\varphi_{ab} = \varphi_{ab}(\mathbf{Q})$ are the kinetic coefficients which again are the entries of a symmetric positive semi-definite matrix.

4.3.6 Entropy production terms, Π_a

The remaining undefined dissipative terms, the entropy production terms Π_a, $a = 1, \ldots, \mathrm{N}$, serve the goal of making the system compatible with the two laws of thermodynamics. Therefore, to fulfill the first and second law of thermodynamics (see (60) and (63) for details), Π_a must be defined as

$$\Pi_a := \frac{1}{\mathcal{E}_{\eta_a}} \left(\hat{\Pi}_a + c_a \tilde{\Pi} \right) \tag{58a}$$

where

$$\hat{\Pi}_a := \sum_{k=1}^{3} \frac{1}{\gamma_{a,k}} \left[\left(\gamma_{a,k} \mathcal{E}_{J_{a,k}} + \sum_{b=1}^{\mathrm{N}-1} \zeta_{ba,k} \mathcal{E}_{w_{b,k}} \right)^2 - \left(\sum_{b=1}^{\mathrm{N}-1} \zeta_{ba,k} \mathcal{E}_{w_{b,k}} \right)^2 + \sum_{b=1}^{\mathrm{N}-1} \zeta_{ba,k}^2 \mathcal{E}_{w_{b,k}}^2 \right], \tag{58b}$$

$$\tilde{\Pi} := \frac{1}{\rho} \mathcal{E}_{A_{Ji}} \Upsilon \mathcal{E}_{A_{Jk}} + \sum_{b=1}^{\mathrm{N}-1} \sum_{c=1}^{\mathrm{N}-1} \left(\sum_{k=1}^{3} \left(\mathcal{E}_{w_{c,k}} \lambda_{cb,k} \mathcal{E}_{w_{b,k}} - \frac{1}{\gamma_{c,k}} \mathcal{E}_{w_{b,k}}^2 \zeta_{bc,k}^2 \right) + \rho \mathcal{E}_{\varrho_b} \chi_{bc} \mathcal{E}_{\varrho_c} + \rho \mathcal{E}_{\varphi_b} \varphi_{bc} \mathcal{E}_{\varphi_c} \right). \tag{58c}$$

Remark that the positive sign of each $\Pi_a \geq 0$ is guaranteed for the case when the coupling coefficients $\zeta_{ab,k}$ in (51) vanish. In this case, (58) is the sum of quadratic forms with positive semi-definite matrices of coefficients, $\lambda_{ab,k}$, χ_{ab}, φ_{bc}, and hence $\Pi_a \geq 0$. Apparently, for sufficiently small $\zeta_{ab,k}$ we also have $\Pi_a \geq 0$ (because $\hat{\Pi}_a \geq 0$ and $\tilde{\Pi} \geq 0$), but such inequalities cannot be guarantied for arbitrary $\zeta_{ab,k}$. Yet, even if the production terms $\Pi_a \geq 0$, the phase entropies may decrease due to the presence of the temperature relaxation terms π_a that makes the sign of $\Pi_a - \pi_a$, in general, indefinite. This of course doesn't contradict the second law because the mixture constituents are not isolated systems. However, as discussed in the next section, this choice of Π_a guarantees the fulfillment of the second law of thermodynamics for the entire mixture.

4.3.7 Thermodynamic equilibrium

The dissipative source terms Φ_a, $\Lambda_{a,k}$, $\Gamma_{a,k}$ and χ_a are defined in such a way that they diminish the thermodynamic forces $\mathcal{E}_{\varphi_a}$, $\mathcal{E}_{w_{a,k}}$, $\mathcal{E}_{J_{a,k}}$, $\mathcal{E}_{A_{Jk}}$, and $\mathcal{E}_{\chi_a}$, i.e they lead the mixture towards a thermodynamic equilibrium state at which these forces must vanish $\mathcal{E}_{\varphi_a} = 0$, $\mathcal{E}_{w_{a,k}} = 0$, $\mathcal{E}_{J_{a,k}} = 0$, $\mathcal{E}_{A_{Jk}} = 0$, and $\mathcal{E}_{\chi_a} = 0$, while the temperature relaxation terms π_a tend to make the phase temperatures equal.

4.4 Consistency with the first and second laws of thermodynamics

One may notice that the total energy conservation law (first law of thermodynamics) is not listed within the set of equations (47). In fact, one of the main features of all the SHTC models [54, 53, 110, 111, 95] is that the energy conservation law

$$\frac{\partial \mathcal{E}}{\partial t} + \frac{\partial}{\partial x_k}\left(V_k \mathcal{E} + V_k(P\delta_{ik} + w_{a,i}\mathcal{E}_{w_{a,k}} + A_{Ji}\mathcal{E}_{A_{Jk}}) + \mathcal{E}_{\varrho_a}\mathcal{E}_{w_{a,k}} + \mathcal{E}_{\eta_a}\mathcal{E}_{J_{a,k}}\right) = 0 \tag{59}$$

is automatically fulfilled for smooth solutions of system (47). In other words, the energy conservation law is a consequence of the governing equations and can be obtained as a linear combination of the governing equations (47) multiplied with the corresponding factors (the thermodynamic conjugate variables or main-field variables [79]). Thus, Eq.(59) can be obtained as the following linear combination of equations (47) multiplied by the corresponding factors

$$\begin{aligned}(59) \equiv \mathcal{E}_{U_i} \cdot (47a) + \mathcal{E}_{A_{Jk}} \cdot (47b) + \mathcal{E}_{\varrho_a} \cdot (47c) + \mathcal{E}_{w_{a,k}} \cdot (47d) + \mathcal{E}_{\eta_a} \cdot (47e) + \mathcal{E}_{J_{a,k}} \cdot (47f) + \\ + \mathcal{E}_{\rho} \cdot (47g) + \mathcal{E}_{\varphi_a} \cdot (47h).\end{aligned} \tag{60}$$

However, we can obtain zero in the right hand-side of (59) by these means only if we define the phase entropy production terms Π_a as in (58). Note that the temperature relaxation terms π_a are defined in such a way that they sum up to zero in (60):

$$\sum_{a=1}^{\mathrm{N}} \mathcal{E}_{\eta_a} \pi_a = \sum_{a=1}^{\mathrm{N}} T_a \pi_a = 0. \tag{61}$$

As we have already mentioned, if the relaxation processes discussed in the previous section are taken into account, our choice (58) of the phase entropy production terms Π_a cannot guarantee positive sign of $\Pi_a - \pi_a$. However, the mixture itself (in the absence of exchange with the exterior) is an isolated system and the second law must hold. Thus, our choice of the phase entropy production terms Π_a not only guarantees the energy conservation law for the entire mixture (the first law of thermodynamics) but also the second law. Indeed, the mixture entropy density is defined as

$$\eta = \eta_1 + \ldots + \eta_{\mathrm{N}} \tag{62}$$

and fulfills the entropy balance law

$$\frac{\partial \eta}{\partial t} + \frac{\partial (\eta V_a)}{\partial x_k} = \Pi + \pi \geq 0, \tag{63a}$$

which is the sum of the phase entropy balance laws, and where the mixture entropy production Π and π are defined as

$$\Pi := \sum_{a=1}^{\mathrm{N}} \Pi_a = \sum_{a=1}^{\mathrm{N}} \hat{\Pi}_a + \left(\frac{c_1}{T_1} + \ldots + \frac{c_{\mathrm{N}}}{T_{\mathrm{N}}} \right) \tilde{\Pi} \geq 0, \tag{63b}$$

$$\pi = -\sum_{a=1}^{\mathrm{N}} \pi_a = \frac{1}{2} \mathrm{tr} \left(\boldsymbol{M}^{\mathrm{T}} \boldsymbol{M} \right) \geq 0, \tag{63c}$$

with $\boldsymbol{M}$ being a symmetric matrix with the entries

$$M_{ab} = \sqrt{\frac{\varrho_a \varrho_b}{\rho \tau} \frac{(T_a - T_b)^2}{T_a T_b}}, \qquad a, b = 1, \ldots, \mathrm{N}. \tag{64}$$

The sign on the right hand side of (63b), and hence the signe of the overall mixture entropy production in (63), is guaranteed only for sufficiently small coupling coefficients $\zeta_{ab,k}$ in (51).

5 Baer-Nunziato form of the multiphase SHTC equations

As anticipated in the introduction, it is of particular interest to compare the structure of the proposed SHTC multiphase model (47) with the other approaches. However, the SHTC state variables dictated by its variational nature are different from those traditionally used in the popular Baer-Nunziato (BN) model [4], or in the conventional formulation of balance laws for multiphase flows [78, 59, 118, 89, 82]. Therefore, to make the comparison possible, we first need to put the SHTC equations in a form that is similar to the conventional way of writing multiphase models, i.e. in terms of the phase mass, momentum, and energy balance laws.

It is of particular interest to relate the SHTC formulation to the well-known Baer-Nunziato (BN) model [4], which was studied and used for example in [113, 2, 3, 117, 32, 116]. However, to the best of our knowledge, there is no extension of the original two-fluid non-equilibrium (two-pressure, two-velocity) BN model to the case of an arbitrary number of phases, and therefore, a direct comparison is impossible. The authors are only aware of non-equilibrium BN-type models for three phases, see [60, 61]. An interesting alternative compressible multiphase model for a general number of N phases was recently presented and discussed in [64], but it does not take a BN-type form and thus is not directly comparable to the formulation considered here. Nevertheless, it is interesting to put the SHTC model in a form that is similar to the BN model to make such a comparison possible in the future. Moreover, the BN form of the SHTC model and not the original SHTC equations is discretized in this paper as it was our original intention to compare the SHTC model with the BN model in the context of numerical simulations.

Let us first remind the structure of the BN model. In its original formulation [4] it is a two-phase model specifically designed for applications describing the deflagration-to-detonation (DDT) transition in reactive, gas-permeable granular materials. However, nowadays this model is usually referred to by considering only the homogeneous part of the original system, i.e., without the algebraic phase interaction terms, see e.g. [3, 113, 117, 38, 101]. The complete two-fluid seven-equation Baer-Nunziato model, without algebraic source terms, is a first-order system of nonlinear

PDEs, which in our notations, see Section 3.1, reads

$$\frac{\partial \varrho_a}{\partial t} + \frac{\partial u_{a,k}}{\partial x_k} = 0, \tag{65a}$$

$$\frac{\partial u_{a,i}}{\partial t} + \frac{\partial}{\partial x_k}\left(u_{a,i}v_{a,k} + P_a\delta_{ki}\right) = \sum_{b=1}^{\mathrm{N}} p_{\mathrm{I},ab}\frac{\partial \alpha_b}{\partial x_i}, \tag{65b}$$

$$\frac{\partial \mathcal{E}_a}{\partial t} + \frac{\partial}{\partial x_k}\left(v_{a,k}\mathcal{E}_a + v_{a,k}P_a\right) = -\sum_{b=1}^{\mathrm{N}} p_{\mathrm{I},ab}\frac{\partial \alpha_b}{\partial t}, \tag{65c}$$

$$\frac{\partial \alpha_a}{\partial t} + v_{\mathrm{I},a,k}\frac{\partial \alpha_a}{\partial x_k} = 0 \tag{65d}$$

where the subscript $a = 1, 2$ lables the phase. As it is well known, the BN model requires a proper choice of the interface velocity $\boldsymbol{v}_{\mathrm{I,a}} = \{v_{\mathrm{I,a},k}\}$ and the interface pressure $p_{\mathrm{I,ab}}$ [114]. Such a structure of the governing equations for multiphase flows, in the form of mass, momentum, and energy balance laws for each phase, is referred to as the *BN-type form*.

5.1 A BN-type form of the SHTC multiphase model

To compare the structure of the multiphase SHTC model (47) with the BN-type structure, the system of PDEs in (47) is rewritten in terms of the phase mass and momentum. We deliberately keep all the dissipative source terms of the SHTC model in the BN-type form, as we believe that this is will be useful in the future once the multiphase extension of the BN model will be obtained. In the following, we collect the individual phase related terms on the left-hand side, while the *interphase exchange terms* and the terms arising from the dissipative processes considered in 4.3 are collected on the right-hand side.

5.1.1 The phase mass balance equations

The evolution equations in (47c) can be immediately rewritten in a more traditional form using the definition of the mixture velocity V_k and the expression of $\mathcal{E}_{w_{a,k}}$, given in (39g):

$$\frac{\partial \varrho_a}{\partial t} + \frac{\partial\left(\varrho_a v_{a,k}\right)}{\partial x_k} = \chi_a. \tag{66}$$

5.1.2 The phase volume fraction equations

The phase volume fraction equations can be retrieved from the equations (47h), using the conservation of total mass and balance laws of the phase densities (66), and read

$$\frac{\partial \alpha_a}{\partial t} + V_k\frac{\partial \alpha_a}{\partial x_k} = \frac{1}{\rho}\Phi_a. \tag{67}$$

Thus, comparing with the BN model, one can conclude that the interface velocity $v_{\mathrm{I},k}$ of the BN model is replaced by the mixture velocity V_k in the SHTC model, as was already noticed in [109, 108].

5.1.3 The phase momentum equations

The balance laws for the phase momenta can be obtained from the mixture momentum conservation and relative velocity equations in the following way. Let $\mathcal{D}_i^U$ represents the mixture

momentum equation (47a), $\mathcal{D}^{w}_{a,i}$ represents the relative velocity equations (47d), and $\mathcal{D}^{u}_{a,i}$ represents the sought phase momentum equations. Then, the phase momentum balance equations can be obtained as

$$\mathcal{D}^{u}_{a,i} = \frac{\varrho_a}{\rho}\mathcal{D}^{U}_{i} - \frac{\varrho_a}{\rho}\sum_{b=1}^{\mathrm{N}} \varrho_b \mathcal{D}^{w}_{b,i} + \varrho_a \mathcal{D}^{w}_{a,i}. \tag{68}$$

After lengthy but rather straightforward manipulations of the terms in (68), the individual phase momentum balance equations can be written as

$$\frac{\partial u_{a,i}}{\partial t} + \frac{\partial (u_{a,i} v_{a,k} + P_a \delta_{ki} + \sigma^{\mathrm{e}}_{a,ki} + \sigma^{\mathrm{t}}_{a,ki})}{\partial x_k} = -c_a \sum_{b=1}^{\mathrm{N}} p_b \frac{\partial \alpha_b}{\partial x_i} + p_a \frac{\partial \alpha_a}{\partial x_i} \tag{69a}$$

$$-c_a \sum_{b=1}^{\mathrm{N}} \varrho_b \bar{w}_{b,k} \omega_{b,k,i} + \varrho_a \bar{w}_{a,k} \omega_{a,k,i} \tag{69b}$$

$$- c_a \sum_{b=1}^{\mathrm{N}} \varrho_b s_b \frac{\partial T_b}{\partial x_i} + \varrho_a s_a \frac{\partial T_a}{\partial x_i} \tag{69c}$$

$$- c_a \sum_{b=1}^{\mathrm{N}} \frac{\partial \left(\sigma^{\mathrm{e}}_{b,ki} + \sigma^{\mathrm{t}}_{b,ki} \right)}{\partial x_k} + \frac{\partial \left(\sigma^{\mathrm{e}}_{a,ki} + \sigma^{\mathrm{t}}_{a,ki} \right)}{\partial x_k} \tag{69d}$$

$$+ c_a \sum_{b=1}^{\mathrm{N}} \varrho_b \frac{\partial (e^{\mathrm{e}}_b + e^{\mathrm{t}}_b)}{\partial x_i} - \varrho_a \frac{\partial (e^{\mathrm{e}}_a + e^{\mathrm{t}}_a)}{\partial x_i} \tag{69e}$$

$$- c_a \sum_{b=1}^{\mathrm{N}} \varrho_b \Lambda_{b,i} + \varrho_a \Lambda_{a,i} \tag{69f}$$

$$- c_a \sum_{b=1}^{\mathrm{N}} v_{b,i} \chi_b + v_{a,i} \chi_a, \tag{69g}$$

where

$$\sigma^{\mathrm{e}}_{a,ki} := A_{Ji} \frac{\partial \mathcal{E}_a}{\partial A_{Jk}}, \qquad \sigma^{\mathrm{t}}_{a,ki} := J_{a,i} \frac{\partial \mathcal{E}_a}{\partial J_{a,k}}, \qquad \omega_{a,k,i} := \frac{\partial w_{a,i}}{\partial x_k} - \frac{\partial w_{a,k}}{\partial x_i} \tag{70}$$

and $e^{\mathrm{e}}_a = \varepsilon^{\mathrm{e}}_a / \varrho_a$, $e^{\mathrm{t}}_a = \varepsilon^{\mathrm{t}}_a / \varrho_a$, and $\bar{w}_{a,k}$ was previously defined in (13). Here, the presence of the phase transformation terms χ_a is due to the appearance of $\partial \varrho_a / \partial t$ and the need to replace them by their expressions from (66).

The phase momentum equations (69) derived from the SHTC mixture equations can be compared with those of the original BN model in order to understand some differences between the two approaches. Of course, the main differences are related to the phase interaction terms that are collected on the right hand side of (69). Thus, the main difference concerns the fact that in the momentum equations (69) derived from the SHTC mixture theory, no closure problem arises for the interface quantities $p_{\mathrm{I},ab}$ and $v_{\mathrm{I},a,k}$ as in the BN model, as already noticed in [109, 108]. The second difference concerns the presence of the gradients of the relative velocities (lift forces) (69b) and temperature gradients (69c) that are not present in the BN model.

Overall, one can notice that the phase interaction terms are rather complicated and take into account all physical processes occurring in the mixture, including elastic and thermal stresses (69d), interfacial friction (69f), and the phase transformation (69g).

5.1.4 The phase energy equations

The phase energy balance laws can be obtained from the conservation equations of mixture momentum, relative velocity and entropy, similarly to the phase momentum equations, after a lengthy manipulation. However, this procedure is not illustrated in this work, since the energy equations depend directly on the momenta PDEs, and the latter already fulfill the comparative purpose of this section by making the interphase terms clear.

5.2 Multi-distortion extension of the BN formulation of SHTC equations

According to the unified model of continuum mechanics [96] and SHTC formulation for multiphase flows [108, 103], a true non-equilibrium multiphase model should have, in general, different pressures, temperatures, velocities, distortion fields, and etc. for each phase. However, at the moment, we only know how to derive the SHTC multiphase model for the case when the phase distortions are equal, $\boldsymbol{A}_1 = \boldsymbol{A}_2 = \ldots = \boldsymbol{A}_{\mathrm{N}} = \boldsymbol{A}$. Therefore, in this section we discuss a heuristic extension of the SHTC multiphase model in its BN form (69) to the case of different phase distortions $\boldsymbol{A}_a$, and this formulation was used to obtain all the numerical results presented in Section 7.

Let us note that the single-distortion formulation still might be a reasonable approximation in many situations, for example, in high-energy transient problems like in [84, 83]. However, according to our experience, the single-distortion formulation is not suitable for low-Mach long-time fluid-structure interaction problems considered in Section 7. Note that a multiphase single-velocity multi-distortion model was already proposed in [81] in which the distortion fields $\boldsymbol{A}_a$ were transported by the mixture velocity, which is a natural choice for a single-velocity approximation. In our multi-velocity model we opt for the advection of the distortion fields by the phase velocities.

Thus, to extend (69) to the multi-distortion formulation, we employ a heuristic approach and simply introduce the phase distortion fields $\boldsymbol{A}_a = \{A_{a,Jk}\}$ for each phase $a = 1, \ldots, \mathrm{N}$ and assume that each $\boldsymbol{A}_a$ is advected by the phase velocity $\boldsymbol{v}_a$, i.e. we add to system (69) the following equations for the phase distortion fields:

$$\frac{\partial A_{a,Jk}}{\partial t} + \frac{\partial \left(A_{a,Jl} v_{a,l}\right)}{\partial x_k} + v_{a,i}\left(\frac{\partial A_{a,Jk}}{\partial x_i} - \frac{\partial A_{a,Ji}}{\partial x_k}\right) = Z_{a,Jk}. \tag{71}$$

Further modifications concern the elastic stress $\sigma^{\mathrm{e}}_{a,ki}$ and thermodynamically conjugate variables of the phase distortion fields, which (for the elastic energies $\varepsilon^{\mathrm{e}}_a$ used in this paper) are computed as

$$\sigma^{\mathrm{e}}_{a,ki} = A_{a,Ji}\mathcal{E}_{A_{a,Jk}} = A_{a,Ji}\frac{\partial \varepsilon^{\mathrm{e}}_a}{\partial A_{a,Jk}}, \qquad \frac{\partial \varepsilon^{\mathrm{e}}_a}{\partial A_{a,Jk}} = \varrho_a \mathrm{Cs}_a^2 A_{a,Ji}\mathrm{dev}G_{a,ik}. \tag{72}$$

Finally, the strain dissipation source term $Z_{a,Jk}$ in (71) is defined as

$$Z_{a,Jk} := -\frac{1}{\varrho_a}\Upsilon_a \mathcal{E}_{A_{a,Jk}}, \qquad \Upsilon_a = \frac{3}{\tau^{\mathrm{e}}_a}\mathrm{Cs}_a^{-2}\det(\boldsymbol{A}_a)^{5/3}, \tag{73}$$

with τ^{e}_a being the strain relaxation time of phase a, and in general is assumed being different for each phase. This timescale defines the stiff nature of the strain relaxation source term towards an equilibrium state of material deformation, e.g.

1. for $\tau^{\mathrm{e}}_a = 0$, the so-called stiff relaxation limit is achieved instantaneously and therefore inviscid flow is retrieved;

2. for sufficiently small τ_a^{e} with respect to the flow timescale, the model reproduces the Navier-Stokes equations of viscous fluids, for the chosen shear energy, it can be computed to fit the kinematic viscosity ν_a of a fluid as $\tau_a^{\mathrm{e}} = 6\nu_a/\mathrm{Cs}_a^2$;

3. for $\tau_a^{\mathrm{e}} = \infty$ the relaxation is absent and the behavior of a pure elastic solid is retrieved.

The relaxation time τ_a^{e}, in general is a function of the state variables. In the multiphase context, it is useful to define it as a function of the volume fraction α_a for each phase, by means of a smooth logarithmic interpolation, which can be computed as follows

$$\tau_a^{\mathrm{e}} = (\tau_a^{\mathrm{e}})^{\xi}\ \tau_{\mathrm{o}}^{1-\xi}, \tag{74}$$

where ξ can be evaluated by

$$\delta\alpha = \frac{\alpha_a - \alpha_{\mathrm{m}}}{\alpha_{\mathrm{M}} - \alpha_{\mathrm{m}}}, \quad \delta\alpha = \max\big(0, \min(1, \delta\alpha)\big), \quad \xi = \delta\alpha^2(3 - 2\delta\alpha), \tag{75}$$

which results in a smooth transition from τ_a^{e} to τ_{o}, where τ_{o} is usually assumed to be a small constant like 10^{-14}. Then, α_{M} and α_{m} represent the extrema at which this operator makes the transition. In this way, where a phase is not present, the *strain is dissipated instantaneously*, as for a prefect fluid, and no stresses are generated in the respective momentum conservation equation. This rescaling of the relaxation time is well suited to multimaterial problems, and in the rest of the paper is referred to as *vanishing ghost solid relaxation time*.

5.3 Three phase SHTC model in the BN-type form

As the BN model is one of the most popular mathematical models for describing two-phase flows, there are many works in which BN-type equations are solved numerically. However, only a very limited number of publications exist on the mathematical and computational issues of BN models for flows with *more* than two phases [60, 61]. It is therefore very attractive to numerically address the BN-type SHTC multiphase model presented in the previous section 5, which has been also generalized to fluid and solid mechanics in this work.

The BN-type form of the SHTC equations (69), (71) admits an arbitrary number of phases, but in this paper, the numerical tests are restricted to three-phase problems in one and two dimensions. Moreover, we further simplify equations (69) by assuming isothermal conditions, absence of heat conduction and phase transitions, and isotropic phase velocity relaxation.

Such an approximation is reasonable for low-Mach number flows, i.e. shock waves are either totally absent, or very weak. Thus, instead of considering the phase energy balance laws, we assume the conservation of phase entropies on shocks, and consider phase entropy balance equations, which have a much simpler structure than the phase energy balance laws. Therefore, the *phase entropy equations* can be retrieved from the SHTC equations (47e), using the conservation of total mass (47g), and read

$$\frac{\partial s_a}{\partial t} + V_k \frac{\partial s_a}{\partial x_k} = \Pi_a - \pi_a. \tag{76}$$

Then, neglecting the phase pressure relaxation towards a common pressure for all the phases ($\Phi_a = 0$), assuming the absence of phase transformation ($\chi_a = 0$), temperature relaxation ($\pi_a = 0$), and assuming the isotropy of the phase velocity relaxation process ($\lambda_{ab,k}$ becomes λ_a, $a = 1, 2, 3$), the mathematical model that is solved numerically in this paper reads

$$\frac{\partial \varrho_a}{\partial t} + \frac{\partial u_{a,k}}{\partial x_k} = 0 \tag{77a}$$

$$\frac{\partial u_{a,i}}{\partial t} + \frac{\partial}{\partial x_k}\left(u_{a,i}v_{a,k} + P_a\delta_{i,k} - \sigma^{\mathrm{e}}_{a,ik}\right) = -c_a\sum_{b=1}^{\mathrm{N}} p_b\frac{\partial \alpha_b}{\partial x_i} + p_a\frac{\partial \alpha_a}{\partial x_i} \tag{77b}$$

$$- c_a\sum_{b=1}^{\mathrm{N}} \varrho_b\bar{w}_{b,k}\omega_{b,k,i} + \varrho_a\bar{w}_{a,k}\omega_{a,k,i} \tag{77c}$$

$$+ c_a\sum_{b=1}^{\mathrm{N}} \lambda_b\varrho_b\left(v_{b,i} - V_i\right) - \lambda_a\varrho_a\left(v_{a,i} - V_i\right), \tag{77d}$$

$$\frac{\partial s_a}{\partial t} + V_k\frac{\partial s_a}{\partial x_k} = \frac{\lambda_a}{T_a}c_a\left(v_{a,k} - V_k\right)^2, \tag{77e}$$

$$\frac{\partial \alpha_a}{\partial t} + V_k\frac{\partial \alpha_a}{\partial x_k} = 0, \tag{77f}$$

$$\frac{\partial A_{a,Jk}}{\partial t} + \frac{\partial\left(A_{a,Jl}v_{a,l}\right)}{\partial x_k} + v_{a,i}\left(\frac{\partial A_{a,Jk}}{\partial x_i} - \frac{\partial A_{a,Ji}}{\partial x_k}\right) = Z_{a,Jk}. \tag{77g}$$

In order to simplify notation for discussing the numerical method, we introduce a compact matrix-vector notation so that system (77) can be written as

$$\partial_t\mathbf{Q} + \nabla\cdot\mathbf{F}(\mathbf{Q}) + \mathbf{B}(\mathbf{Q})\cdot\nabla\mathbf{Q} = \mathbf{S}(\mathbf{Q}) \tag{78}$$

with $\mathbf{Q} = \{\mathbf{Q}_1, \mathbf{Q}_2, \mathbf{Q}_3\}$ being the vector of conservative state variables, and $\mathbf{Q}_a$ being the conservative variables for each phase $a = 1, 2, 3$:

$$\mathbf{Q}_a = (\varrho_a, \boldsymbol{u}_a, s_a, \alpha_a, \boldsymbol{A}_{a,1}, \boldsymbol{A}_{a,2}, \boldsymbol{A}_{a,3}), \tag{79}$$

where we use the fact that each distortion matrix $\boldsymbol{A}_a$ is in fact a triad of three basis vectors, i.e. $\boldsymbol{A}_a = \{\boldsymbol{A}_{a,1}, \boldsymbol{A}_{a,2}, \boldsymbol{A}_{a,3}\}$ and for each $J = 1, 2, 3$, $\boldsymbol{A}_{a,J} = \{A_{a,J1}, A_{a,J2}, A_{a,J3}\}$ is a 3-vector.

The flux tensor $\mathbf{F}(\mathbf{Q})$ in (78) is decoupled with respect to the phases, i.e. $\mathbf{F}(\mathbf{Q}) = \{\mathbf{F}_1(\mathbf{Q}_1), \mathbf{F}_2(\mathbf{Q}_2), \mathbf{F}_3(\mathbf{Q}_3)\}$, and can be written as the sum of several contributions as follows

$$\mathbf{F}_a(\mathbf{Q}_a) = \mathbf{F}^{\mathrm{c}}_a(\mathbf{Q}_a) + \mathbf{F}^{\mathrm{p}}_a(\mathbf{Q}_a) + \mathbf{F}^{\mathrm{s}}_a(\mathbf{Q}_a) + \mathbf{F}^{\mathrm{d}}_a(\mathbf{Q}_a), \tag{80}$$

where each term depends only on $\mathbf{Q}_a$ and is defined as

$$\mathbf{F}^{\mathrm{c}}_a(\mathbf{Q}_a) = \begin{pmatrix} \boldsymbol{u}_a \\ \boldsymbol{u}_a\otimes\boldsymbol{v}_a \\ \mathbf{0}_{3\times1} \\ \mathbf{0}_{3\times1} \\ \mathbf{0}_{3\times1} \\ \mathbf{0}_{3\times1} \\ \mathbf{0}_{3\times1} \end{pmatrix}, \quad \mathbf{F}^{\mathrm{p}}_a(\mathbf{Q}_a) = \begin{pmatrix} \mathbf{0}_{3\times1} \\ P_a\boldsymbol{I} \\ \mathbf{0}_{3\times1} \\ \mathbf{0}_{3\times1} \\ \mathbf{0}_{3\times1} \\ \mathbf{0}_{3\times1} \\ \mathbf{0}_{3\times1} \end{pmatrix}, \quad \mathbf{F}^{\mathrm{s}}_a(\mathbf{Q}_a) = \begin{pmatrix} \mathbf{0}_{3\times1} \\ \boldsymbol{\sigma}^{\mathrm{e}}_a \\ \mathbf{0}_{3\times1} \\ \mathbf{0}_{3\times1} \\ \mathbf{0}_{3\times1} \\ \mathbf{0}_{3\times1} \\ \mathbf{0}_{3\times1} \end{pmatrix}, \quad \mathbf{F}^{\mathrm{d}}_a(\mathbf{Q}_a) = \begin{pmatrix} \mathbf{0}_{3\times1} \\ \mathbf{0}_{3\times3} \\ \mathbf{0}_{3\times1} \\ \mathbf{0}_{3\times1} \\ \boldsymbol{A}_{a,1}\boldsymbol{v}_a\boldsymbol{I} \\ \boldsymbol{A}_{a,2}\boldsymbol{v}_a\boldsymbol{I} \\ \boldsymbol{A}_{a,3}\boldsymbol{v}_a\boldsymbol{I} \end{pmatrix}, \tag{81}$$

Thus, tensor $\mathbf{F}^{\mathrm{c}}_a(\mathbf{Q}_a)$ contains the convective terms for the mass and momentum balance equations, $\mathbf{F}^{\mathrm{p}}_A(\mathbf{Q}_a)$ is the phase related pressure flux tensor, $\mathbf{F}^{\mathrm{s}}_a(\mathbf{Q}_a)$ is the flux tensor containing contribution due to shear viscous and elastic stresses, while $\mathbf{F}^{\mathrm{d}}_a(\mathbf{Q}_a)$ contains advective terms from the distortion PDE.

The so-called non-conservative matrix-vector product in (78) contains the phase coupling terms and can be presented as a sum of the following contributions

$$\mathbf{B}(\mathbf{Q})\cdot\nabla\mathbf{Q} = \left[\mathbf{B}^{\mathrm{c}}(\mathbf{Q}) + \mathbf{B}^{\mathrm{p}}(\mathbf{Q}) + \mathbf{B}^{\mathrm{w}}(\mathbf{Q}) + \mathbf{B}^{\mathrm{d}}(\mathbf{Q})\right]\cdot\nabla\mathbf{Q}, \tag{82}$$

where the convective part is given by (components restricted to phase a)

$$\left(\mathbf{B}^{\mathrm{c}}(\mathbf{Q})\cdot\nabla\mathbf{Q}\right)_a = (0,\mathbf{0},\boldsymbol{V}\cdot\nabla s_a,\boldsymbol{V}\cdot\nabla\alpha_a,\mathbf{0},\mathbf{0},\mathbf{0}), \tag{83}$$

while the non-conservative products related to the multiphase and multi-material nature of the model read

$$\left(\mathbf{B}^{\mathrm{p}}(\mathbf{Q})\cdot\nabla\mathbf{Q}\right)_a = \left(0, c_a\sum_{b=1}^{\mathrm{N}} p_b\nabla\alpha_b - p_a\nabla\alpha_a, 0, 0, \mathbf{0}, \mathbf{0}, \mathbf{0}\right), \tag{84}$$

$$\left(\mathbf{B}^{\mathrm{w}}(\mathbf{Q})\cdot\nabla\mathbf{Q}\right)_a = \left(0, c_a\sum_{b=1}^{\mathrm{N}} \varrho_b(\nabla\boldsymbol{v}_b-\nabla\boldsymbol{v}_b^T)(\boldsymbol{v}_b-\boldsymbol{V}) - \varrho_a(\nabla\boldsymbol{v}_a-\nabla\boldsymbol{v}_a^T)(\boldsymbol{v}_a-\boldsymbol{V}), 0, 0, \mathbf{0}, \mathbf{0}, \mathbf{0}\right), \tag{85}$$

$$\left(\mathbf{B}^{\mathrm{d}}(\mathbf{Q})\cdot\nabla\mathbf{Q}\right)_a = \left(0,\mathbf{0},0,0,\left(\nabla\boldsymbol{A}_{a,1}-\nabla\boldsymbol{A}_{a,1}^T\right)\boldsymbol{v}_a,\left(\nabla\boldsymbol{A}_{a,2}-\nabla\boldsymbol{A}_{a,2}^T\right)\boldsymbol{v}_a,\left(\nabla\boldsymbol{A}_{a,3}-\nabla\boldsymbol{A}_{a,3}^T\right)\boldsymbol{v}_a\right). \tag{86}$$

The source term vector $\mathbf{S}(\mathbf{Q})$ can be written as the sum of two different vectors that will be discretized by two different approaches,

$$\mathbf{S}(\mathbf{Q}) = \mathbf{S}^{\mathrm{w}}(\mathbf{Q}) + \mathbf{S}^{\mathrm{s}}(\mathbf{Q}), \tag{87}$$

where $\mathbf{S}^{\mathrm{v}}(\mathbf{Q})$ is stiff but linear in $\mathbf{Q}$ (relative velocity relaxation), while $\mathbf{S}^{\mathrm{s}}(\mathbf{Q})$ is related to the strain relaxation source terms of the distortion matrix, which is nonlinear and can be extremely stiff. These source term vectors read

$$\mathbf{S}^{\mathrm{w}}(\mathbf{Q}_a) = \begin{pmatrix} 0 \\ c_a\sum_{b=1}^{\mathrm{N}}\lambda_b\varrho_b\left(\boldsymbol{v}_b-\boldsymbol{V}\right) - \lambda_a\varrho_a\left(\boldsymbol{v}_a-\boldsymbol{V}\right) \\ 0 \\ \frac{\lambda_a}{T_a}c_a\left(\boldsymbol{v}_a-\boldsymbol{V}\right)^2 \\ \mathbf{0} \\ \mathbf{0} \\ \mathbf{0} \end{pmatrix}, \quad \mathbf{S}^{\mathrm{s}}(\mathbf{Q}_a) = \begin{pmatrix} 0 \\ 0 \\ 0 \\ 0 \\ \mathbf{Z}_{a,1} \\ \mathbf{Z}_{a,2} \\ \mathbf{Z}_{a,3} \end{pmatrix}, \tag{88}$$

where $\boldsymbol{Z}_a = \{\boldsymbol{Z}_{a,1}, \boldsymbol{Z}_{a,2}, \boldsymbol{Z}_{a,3}\}$ is the phase strain relaxation matrix defined in (73).

Furthermore, to better address some of the specific issues usually encountered in the numerical solution of multiphase flow models, it is convenient to introduce the so-called primitive variables. For example, in the multiphase context and high-order FV schemes, the use of only conservative variables, such as ϱ_a and $\boldsymbol{u}_a$, may result in non-physical discontinuities in the reconstructed velocity and density fields, as well as violations of the positivity constraint in the reconstructed mass fraction values [27]. Whereas, a reconstruction in the primitive variable space, for a second-order MUSCL-Hancock TVD scheme, significantly mitigates these problems, see e.g. [80, 130, 27] and references therein.

Therefore, alongside with the vector of conservative variables $\mathbf{Q} = (\mathbf{Q}_a, \mathbf{Q}_2, \mathbf{Q}_3)$ we consider the vector of primitive variables $\mathbf{V} = (\mathbf{V}_1, \mathbf{V}_2, \mathbf{V}_3)$, where for each phase $a = 1, 2, 3$,

$$\mathbf{Q}_a = (\varrho_a, \boldsymbol{u}_a, s_a, \alpha_a, \boldsymbol{A}_a), \qquad \mathbf{V}_a = (\rho_a, \boldsymbol{v}_a, p_a, \alpha_a, \boldsymbol{A}_a), \tag{89}$$

The *primitive-to-conservative* transformation operator will be denoted by $\mathcal{C}$ and its complementary *conservative-to-primitive* by $\mathcal{P}$, i.e.

$$\mathbf{V}_a(x,y) = \mathcal{P}[\mathbf{Q}_a(x,y)], \qquad \text{and} \qquad \mathbf{Q}_a(x,y) = \mathcal{C}[\mathbf{V}_a(x,y)]. \tag{90}$$

In the mixture context, these operators must be defined with care to avoid division by zero when a phase vanishes. In the following, we illustrate how these conversion operators are defined in

our numerical method to address this issue and to satisfy the unit sum constraints on the volume fractions.

First, a sum of the volume fractions over the phases is evaluated

$$\alpha_{tot} = \sum_{a=1}^{\mathrm{N}} \alpha_a, \tag{91}$$

from which a preliminary phase volume fraction is computed as

$$\alpha_a^* = \max(\epsilon, \min\left(1, \alpha_a/\alpha_{tot}^*\right)), \tag{92}$$

where $\epsilon = 10^{-14}$ is a small constant introduced to avoid division by zero in the following formula. Then the conservative-to-primitive $\mathcal{P}$ operator reads

$$\mathcal{P}[\mathbf{Q}_a] = \begin{pmatrix} \varrho_a/\alpha_a^* \\ \boldsymbol{u}_a \varrho_a/(\varrho_a^2 + \epsilon^2) \\ P[\varrho_a/\alpha_a^*, s_a] \\ \max(\epsilon, \min\left(1, \alpha_a/\alpha_{tot}^*\right)) \\ \boldsymbol{A}_a \end{pmatrix}, \tag{93}$$

where $P[\varrho_a/\alpha_a^*, s_a]$ is the pressure function that can be defined according to the EOS chosen for the phase.

6 Explicit FV scheme for compressible multiphase fluid and solid mechanics

In this section, we describe the way we adapt the well-known Finite-Volume (FV) MUSCL-Hancock method [129, 126] for addressing the challenges encountered while solving the BN form of the SHTC multifluid model 5.3. The multiphase system is restricted to at most three phases. However, they can be freely chosen as gaseous, viscous or inviscid liquid, or elastoplastic solid, e.g. the multiphase system can be a gas-liquid-solid system or gas-solid-solid system, etc. The phase interfaces are treated in the spirit of the *diffuse interface approach*, thanks to the suitable mathematical description of the interfaces through the volume fractions α_a.

Due to the presence of source terms in (77), the MUSCL-Hancock scheme will be implemented in an *operator splitting* manner. Moreover, to address the stiff character of the relaxation source terms, a specially designed implicit discretization of the sources is incorporated at both the predictor and corrector stages of the scheme. To address the presence of the non-conservative product terms in (77), a path-conservative variant of the MUSCL-Hancock scheme is employed.

6.1 Data representation and reconstruction, slope limiting

The computational domain $\Omega \subset \mathbb{R}^2$ is partitioned in Cartesian elements, denoted by

$$\Omega_{ij} = \left[x_i - \frac{\Delta x_i}{2}, x_i + \frac{\Delta x_i}{2}\right] \times \left[y_j - \frac{\Delta y_j}{2}, y_j + \frac{\Delta y_j}{2}\right], \tag{94}$$

where the indices i and j go from 1 to the total number of elements in each direction. From now on, to avoid possible confusion of spatial and discretization indices, we shall use x for the direction x_1, and y for the direction x_2.

The discrete solution of the conservative and primitive state variables for a generic element Ω_{ij} at time t^n is denoted by $\mathbf{Q}_{i,j}^n$ and $\mathbf{V}_{ij}^n$, and which are defined as volume (area) averaged values, i.e.

$$\mathbf{Q}_{i,j}^n = \frac{1}{|\Omega_{ij}|}\int_{\Omega_{ij}} \mathbf{Q}(x,y,t^n)d\Omega, \qquad \mathbf{V}_{i,j}^n = \frac{1}{|\Omega_{ij}|}\int_{\Omega_{ij}} \mathbf{V}(x,y,t^n)d\Omega. \tag{95}$$

In order to achieve a second-order accuracy, it is necessary to perform a data reconstruction that, for each cell, yields a first-degree polynomial representation of the state variables, named $\mathbf{Q}_{ij}^r(x,y,t)$ and $\mathbf{V}_{ij}^r(x,y,t)$.

A cell-local primitive variable polynomial reconstruction $\mathbf{V}_{ij}^r(x,y,t)$ is now reconstructed, for each element Ω_{ij}, from the discrete primitive state vector $\mathbf{V}_{ij}^n$ at time t^n. For each Cartesian cell Ω_{ij}, a jump in primitive variables through each edge can be evaluated. These are then combined in a non-linear fashion in order to obtain a slope in the x and y-direction respectively and to guarantee non-oscillatory properties of the resulting scheme. For instance, in the x-direction, left and right jumps are evaluated as

$$\Delta\mathbf{V}_L = \mathbf{V}_{i,j}^n - \mathbf{V}_{i-1,j}^n \qquad \text{and} \qquad \Delta\mathbf{V}_R = \mathbf{V}_{i+1,j}^n - \mathbf{V}_{i,j}^n, \tag{96}$$

respectively. These are then combined in a non-linear fashion to obtain a preliminary slope $\widetilde{\Delta\mathbf{V}}_i$ by means of a slope limiter. In our implmentation, we use a limiter that is usually referred to as the *Generalised minmod slope limiter*, and is given by

$$\widetilde{\Delta\mathbf{V}}_i = \frac{\Delta\mathbf{V}_R\ \max\left[\,0,\ \min\left(\,\beta\Delta\mathbf{V}_R^2,\ \Delta\mathbf{V}_R\Delta\mathbf{V}_L\right)\right]}{2\ \Delta\mathbf{V}_R^2+\epsilon^2} + \frac{\Delta\mathbf{V}_L\ \max\left[\,0,\ \min\left(\,\beta\Delta\mathbf{V}_L^2,\ \Delta\mathbf{V}_L\Delta\mathbf{V}_R\right)\right]}{2\ \Delta\mathbf{V}_L^2+\epsilon^2}, \tag{97}$$

where ϵ is a small constant that avoids division by zero, e.g. $\epsilon = 10^{-14}$, and β defines a family of *minmod* limiters. For $\beta = 1$, the classic minmod slope limiter is obtained, whereas it reduces to the MUSCL-Barth-Jespersen limiter for $\beta = 3$, and $\beta = 2$ represents a good compromise between robustness and dissipation, and this value will be assumed for all the subsequent numerical tests.

In fact the slope $\widetilde{\Delta\mathbf{V}}_i$ is not the final slope but a *preliminary* one since it was found useful to adopt a slope *rescaling* approach presented in [25]. Thus, after $\widetilde{\Delta\mathbf{V}}_i$ is computed it is then corrected to impose an upper or lower limit for certain variables; in this way, the positivity of the reconstructed density values is guaranteed and the upper and lower bounds of the volume fractions of the phases are respected. We list below the steps to achieve this rescaling

$$\Delta\mathbf{V}_i = \widetilde{\Delta\mathbf{V}}_i \min\left(1, \Phi_i^+, \Phi_i^-\right), \tag{98}$$

with

$$\begin{aligned}
\Phi_i^+ &= \frac{\left[\left(\mid\widetilde{\Delta\mathbf{V}}_i\mid +\widetilde{\Delta\mathbf{V}}_i\right)(\mathbf{V}_M-\mathbf{V}_i) + \left(\mid\widetilde{\Delta\mathbf{V}}_i\mid -\widetilde{\Delta\mathbf{V}}_i\right)(\mathbf{V}_m-\mathbf{V}_i)\right]\widetilde{\Delta\mathbf{V}}_i}{2\mid\widetilde{\Delta\mathbf{V}}_i^3\mid+\epsilon^3}, \\
\Phi_i^- &= \frac{\left[\left(\mid\widetilde{\Delta\mathbf{V}}_i\mid -\widetilde{\Delta\mathbf{V}}_i\right)(\mathbf{V}_i-\mathbf{V}_M) + \left(\mid\widetilde{\Delta\mathbf{V}}_i\mid +\widetilde{\Delta\mathbf{V}}_i\right)(\mathbf{V}_i-\mathbf{V}_m)\right]\widetilde{\Delta\mathbf{V}}_i}{2\mid\widetilde{\Delta\mathbf{V}}_i^3\mid+\epsilon^3},
\end{aligned} \tag{99}$$

where, the vectors $\mathbf{V}_m$ and $\mathbf{V}_M$ represent the lower and upper bounds for each variable of the primitive state vector, and are set, for each phase $a = 1, 2, 3$, as

$$\mathbf{V}_{m,a} = (0, -\boldsymbol{h}, -H, 0, -\boldsymbol{H})_a, \quad \text{and} \quad \mathbf{V}_{M,a} = (H, \boldsymbol{h}, H, 1, \boldsymbol{H})_a, \tag{100}$$

where the values of H, $\boldsymbol{h}$ and $\boldsymbol{H}$ should be set to certain bound values following from the physical meaning of the corresponding quantity or to arbitrary large value to represent the absence of

bounds. The analogous steps are performed in y-direction to calculate the reconstruction of the slope $\Delta \mathbf{V}_j$.

After the spatial reconstruction, at a given time instant t^n, the cell-local space-time primitive variable polynomial reconstruction, in each cell Ω_{ij}, is written in terms of a space-time Taylor series expanded about x_i, y_i and t^n as

$$\mathbf{V}^r_{i,j}(x,y,t) = \mathbf{V}^n_{i,j} + (x - x_{i,j})\frac{\Delta \mathbf{V}_i}{\Delta x} + (y - y_{i,j})\frac{\Delta \mathbf{V}_j}{\Delta y} + (t - t^n)\ \partial_t \mathbf{V}_{i,j}. \tag{101}$$

The time derivative, in (101), is computed in terms of primitive variables in two steps, through the following straight-forward application of the operator splitting approach.

Thus, to determine $\partial_t \mathbf{V}_{i,j}$, we consider

$$\partial_t \mathbf{V}_{i,j} = -\ (\mathbf{C}\cdot\hat{\boldsymbol{n}}_x)\ \partial_x \mathbf{V} -\ (\mathbf{C}\cdot\hat{\boldsymbol{n}}_y)\ \partial_y \mathbf{V} + \mathbf{S}, \tag{102}$$

where

$$\mathbf{C} = \left(\frac{\partial \mathbf{Q}}{\partial \mathbf{V}}\right)^{-1}\left(\frac{\partial \mathbf{F}(\mathbf{Q})}{\partial \mathbf{V}} + \mathbf{B}(\mathbf{Q})\frac{\partial \mathbf{Q}}{\partial \mathbf{V}}\right) \qquad \text{and} \qquad \tilde{\mathbf{B}} = \mathbf{B}(\mathbf{Q})\frac{\partial \mathbf{Q}}{\partial \mathbf{V}}. \tag{103}$$

To solve (102), we split it into the homogeneous part

$$\partial_t \mathbf{V}_{i,j} = -\ (\mathbf{C}\cdot\hat{\boldsymbol{n}}_x)\ \partial_x \mathbf{V} -\ (\mathbf{C}\cdot\hat{\boldsymbol{n}}_y)\ \partial_y \mathbf{V}, \tag{104}$$

and the source part

$$\frac{\mathrm{d}\mathbf{V}_{i,j}}{\mathrm{d}\hat{t}} = \mathbf{S}(\mathbf{V}_{i,j}), \qquad \hat{t} \in [t^n, t]. \tag{105}$$

In order to approximate the spatial derivatives of the primitive state variables in (104), we use a central finite difference with respect to the cell center by using the boundary primitive reconstructed values from within the cell $\Omega_{i,j}$, as

$$\partial_t \mathbf{V}_{i,j} \approx \left(\mathbf{C}(\mathbf{V}^n_{i,j})\cdot\hat{\boldsymbol{n}}_x\right)\frac{\Delta \mathbf{V}_i}{\Delta x} + \left(\mathbf{C}(\mathbf{V}^n_{i,j})\cdot\hat{\boldsymbol{n}}_y\right)\frac{\Delta \mathbf{V}_j}{\Delta y}. \tag{106}$$

Hence, using (106), one can compute an update for each cell, such that $\mathbf{V}^*_{i,j}$ is the solution of (104) at time t with an initial value $\mathbf{V}^n_{i,j}$, as follows

$$\mathbf{V}^*_{i,j} = \mathbf{V}^n_{i,j} + (t - t^n)\ \partial_t \mathbf{V}_{i,j}. \tag{107}$$

In the second step, we consider the contribution of the stiff source terms via solving the initial value problem

$$\frac{d\mathbf{V}_{i,j}}{d\hat{t}} = \mathbf{S}(\mathbf{V}_{i,j}), \qquad \hat{t} \in [t^n, t], \qquad \mathbf{V}_{i,j}(t^n) = \mathbf{V}^*_{i,j}, \tag{108}$$

whose solution at time t is denoted by $\mathbf{V}^{**}_{i,j}$. This initial value problem is solved with two different implicit methods discussed in detail in Sec. 6.3.

Finally, by introducing the discrete solution $\mathbf{V}^{**}_{i,j}$ of $\partial_t \mathbf{V}_{i,j}$ in (101), the cell-local primitive variable polynomial reconstruction reads

$$\mathbf{V}^r_{i,j}(t,x,y) = \mathbf{V}^{**}_{i,j}(t) + (x - x_{i,j})\frac{\Delta \mathbf{V}_i}{\Delta x} + (y - y_{i,j})\frac{\Delta \mathbf{V}_j}{\Delta y}, \tag{109}$$

which we also refer to as the *cell-local space-time predictor*.

6.2 Explicit finite volume discretization of the homogeneous system

After obtaining the local space-time predictor (109), the final solution $\mathbf{Q}_{i,j}^{n+1}$ at t^{n+1} of the MUSCL-Hancock scheme is also computed using the splitting approach, in which we first compute the solution of the homogeneous PDE system

$$\partial_t \mathbf{Q} + \nabla \cdot \mathbf{F}(\mathbf{Q}) + \mathbf{B}(\mathbf{Q}) \cdot \nabla \mathbf{Q} = \mathbf{0}, \tag{110}$$

with the initial data obtained by extrapolating the reconstructed polynomials towards the cell boundaries and by applying the standard explicit FV update formula to (110). The latter is obtained by integrating (110) over the space-time element and applying Gauss's theorem for integrating the divergence of fluxes in space:

$$\int_{t^n}^{t^{n+1}} \int_{\Omega_{ij}} \partial_t \mathbf{Q} \mathrm{d}\boldsymbol{x}\mathrm{d}t + \int_{t^n}^{t^{n+1}} \int_{\partial\Omega_{ij}} \mathbf{F}(\mathbf{Q}) \cdot \hat{\mathbf{n}} \mathrm{d}S\mathrm{d}t + \int_{t^n}^{t^{n+1}} \int_{\Omega_{ij}} \mathbf{B}(\mathbf{Q}) \cdot \nabla \mathbf{Q} \, \mathrm{d}\boldsymbol{x}\mathrm{d}t = 0, \tag{111}$$

where $\hat{\mathbf{n}}$ defines the outward unit normal vector on the element boundary, and $\mathrm{d}\boldsymbol{x} = \mathrm{d}x\mathrm{d}y$.

Then, by using the reconstructed polynomials $\mathbf{V}_{i,j}^r(t,x,y)$ and treating the non-conservative terms using the path-conservative approach by Castro and Parés [88, 22], we get the usual *path-conservative* FV discretization

$$\begin{aligned} \int_{t^n}^{t^{n+1}} \int_{\Omega_{ij}} \partial_t \mathbf{Q} d\boldsymbol{x}\mathrm{d}t + \int_{t^n}^{t^{n+1}} \int_{\partial\Omega_{ij}} \left(\mathbf{F}(\mathbf{V}_{i,j}^{r,-}, \mathbf{V}_{i,j}^{r,+}) + \mathbf{D}(\mathbf{V}_{i,j}^{r,-}, \mathbf{V}_{i,j}^{r,+}) \right) \cdot \hat{\mathbf{n}} \mathrm{d}S\mathrm{d}t + \\ + \int_{t^n}^{t^{n+1}} \int_{\Omega_{ij} n \partial\Omega_{ij}} \tilde{\mathbf{B}}(\mathbf{V}_{i,j}^r) \cdot \nabla \mathbf{V}_{i,j}^r \, d\boldsymbol{x}\mathrm{d}t = 0, \end{aligned} \tag{112}$$

where, within the framework of path-conservative schemes, the new term $\mathbf{D}$ was introduced to take into account the jumps of the primitive variables $\mathbf{V}$ across the space-time element boundaries $\partial\Omega_{ij}$, while the last term is the integral over the smooth part of the non-conservative terms.

Using notations (95), the fully discrete one-step update formula for the solution $\mathbf{Q}_{i,j}^{(1)}$ of the homogeneous part of the system at time t^{n+1} reads

$$\begin{aligned} \mathbf{Q}_{i,j}^{(1)} = \mathbf{Q}_{i,j}^n - \frac{\Delta t}{\Delta x} \left(\mathbf{F}_{i+1/2,j}^{\mathrm{RS}} - \mathbf{F}_{i-1/2,j}^{\mathrm{RS}} + \mathbf{D}_{i+1/2,j} + \mathbf{D}_{i-1/2,j} \right) + \\ - \frac{\Delta t}{\Delta y} \left(\mathbf{F}_{i,j+1/2}^{\mathrm{RS}} - \mathbf{F}_{i,j-1/2}^{\mathrm{RS}} + \mathbf{D}_{i,j+1/2} + \mathbf{D}_{i,j-1/2} \right) + \\ + \frac{\Delta t}{\Delta x} \tilde{\mathbf{B}}_1 \left[\mathbf{V}_{i,j}^r \left(t^{\,n+1/2}, x_i, y_j \right) \right] \Delta \mathbf{V}_i + \\ + \frac{\Delta t}{\Delta y} \tilde{\mathbf{B}}_2 \left[\mathbf{V}_{i,j}^r \left(t^{\,n+1/2}, x_i, y_j \right) \right] \Delta \mathbf{V}_j, \end{aligned} \tag{113}$$

where $\mathbf{F}^{\mathrm{RS}}$ is the generic conservative numerical flux, which can be compute with different approximate Riemann solvers.

In order to describe easily each term in (113), we introduce a compact notation for the boundary-extrapolated primitive states $\mathbf{V}_R$ and $\mathbf{V}_L$, which can be evaluated from the solution of the cell-local space-time predictor (109). In particular, the space-time midpoint values for each face, of generic index $i+\frac{1}{2}, j$ in the x-direction or $i, j+\frac{1}{2}$ in the y-direction, read

$$\begin{aligned} (\mathbf{V}_L)_{i+\frac{1}{2},j} &= \mathbf{V}_{i,j}^r(t^{n+\frac{1}{2}}, x_{i+\frac{1}{2}}, y_j), \quad (\mathbf{V}_R)_{i+\frac{1}{2},j} = \mathbf{V}_{i+1,j}^r(t^{n+\frac{1}{2}}, x_{i+\frac{1}{2}}, y_j), \\ (\mathbf{V}_L)_{i,j+\frac{1}{2}} &= \mathbf{V}_{i,j}^r(t^{n+\frac{1}{2}}, x_i, y_{j+\frac{1}{2}}), \quad (\mathbf{V}_R)_{i,j+\frac{1}{2}} = \mathbf{V}_{i,j+1}^r(t^{n+\frac{1}{2}}, x_i, y_{j+\frac{1}{2}}). \end{aligned} \tag{114}$$

Thus, using this simpler notation, we illustrate how conservative numerical $\mathbf{F}^{\mathrm{RS}}$ flows are defined. In this paper, we employ the simple Rusanov flux:

$$\begin{aligned}\mathbf{F}^{\mathrm{RS}}_{i+1/2,j}(\mathbf{V}_L,\mathbf{V}_R) &= \frac{1}{2}\Big(\mathbf{F}_1(\mathbf{V}_L)+\mathbf{F}_1(\mathbf{V}_R)\Big) - \frac{1}{2}s_1^{\max}\Big(\mathcal{C}[\mathbf{V}_R]-\mathcal{C}[\mathbf{V}_L]\Big),\\ \mathbf{F}^{\mathrm{RS}}_{i,j+1/2}(\mathbf{V}_L,\mathbf{V}_R) &= \frac{1}{2}\Big(\mathbf{F}_2(\mathbf{V}_L)+\mathbf{F}_2(\mathbf{V}_R)\Big) - \frac{1}{2}s_2^{\max}\Big(\mathcal{C}[\mathbf{V}_R]-\mathcal{C}[\mathbf{V}_L]\Big),\end{aligned} \tag{115}$$

where $\mathbf{F}_1$ and $\mathbf{F}_2$ are the conservative fluxes in the first and in the second space direction.

The Rusanov numerical flux requires the knowledge of an estimate for the maximum wave velocity $s^{\max}$ for each direction. In this paper, keeping in mind that we are interested in problems with not high Mach numbers, the absolute value of the maximum eigenvalue of the PDE system linearized at the states $\mathbf{V}_L$ and $\mathbf{V}_R$ can be a good estimate for $s^{\max}$. Therefore, the maximum wave speed estimates read

$$\begin{aligned}s_1^{\max}(\mathbf{V}_L,\mathbf{V}_R) &= \max\big(\ \lambda_1^{\max}(\mathbf{V}_L),\ \lambda_1^{\max}(\mathbf{V}_R)\ \big),\\ s_2^{\max}(\mathbf{V}_L,\mathbf{V}_R) &= \max\big(\ \lambda_2^{\max}(\mathbf{V}_L),\ \lambda_2^{\max}(\mathbf{V}_R)\ \big).\end{aligned} \tag{116}$$

The maximum eigenvalues of (77) can be estimated as described in A.

The nonconservative products appearing in the BN model are treated within the framework of path-conservative schemes [22, 88, 23, 24, 38]. Thus, at each cell interface the following path integrals must be prescribed

$$\mathbf{D}_\Psi(\mathbf{V}_L,\mathbf{V}_R)\cdot\hat{\mathbf{n}} = \frac{1}{2}\int_0^1 \tilde{\mathbf{B}}\left[\Psi(\mathbf{V}_L,\mathbf{V}_R,s)\right]\cdot\hat{\mathbf{n}}\frac{\partial\Psi}{\partial s}\mathrm{d}s = \frac{1}{2}\left(\int_0^1 \tilde{\mathbf{B}}\left[\Psi(\mathbf{V}_L,\mathbf{V}_R,s)\right]\cdot\hat{\mathbf{n}}\mathrm{d}s\right)(\mathbf{V}_R-\mathbf{V}_L), \tag{117}$$

in which $\Psi(\mathbf{V}_L,\mathbf{V}_R,s) = \mathbf{V}_L + s(\mathbf{V}_R-\mathbf{V}_L)$ is a simple segment path function connecting the left and right states in the primitive state space. These path integrals, which are denoted by $\mathbf{D}_{i+1/2,j}$ and $\mathbf{D}_{i,j+1/2}$ in (113), are computed with a three-point Gauss-Legendre quadrature rule with points $s_k \in [0,1]$ and weights w_k as follows (see [38])

$$\begin{aligned}\mathbf{D}_{i+1/2,j} &= \frac{1}{2}\sum_{k=1}^{3} w_k\ \tilde{\mathbf{B}}_1\Big[\Psi(\mathbf{V}_L,\mathbf{V}_R,s_k)\Big]\ (\mathbf{V}_R-\mathbf{V}_L),\\ \mathbf{D}_{i,j+1/2} &= \frac{1}{2}\sum_{k=1}^{3} w_k\ \tilde{\mathbf{B}}_2\Big[\Psi(\mathbf{V}_L,\mathbf{V}_R,s_k)\Big]\ (\mathbf{V}_R-\mathbf{V}_L)\ .\end{aligned} \tag{118}$$

Therefore, by these means we compute the preliminary state vector $\mathbf{Q}^{(1)}_{i,j}$, which is the updated solution of the left hand side of (78). To get the final solution $\mathbf{Q}^{n+1}_{i,j}$, it remains to compute the solution of the relaxation source terms, which is done in the next section.

Before describing in detail the implicit solver for the relaxation source terms, we note that in order to guarantee stability of the explicit FV time-stepping described above, the time-step size is restricted by

$$\Delta t \le k_{\mathrm{CFL}}\frac{1}{\Delta x/\lambda_1^M + \Delta y/\lambda_2^M}, \tag{119}$$

where λ_k^M is the maximum absolute value of all eigenvalues found in the domain, in the x_k-direction, which, for system (77), can be estimated as detailed in A. Also, $k_{\mathrm{CFL}} \le 1$ is a Courant-type number [29], which is typically chosen as $k_{\mathrm{CFL}} = 0.9$ for all the simulations presented in this work.

6.3 Integration of relaxation sources

As previously mentioned, to account for the algebraic relaxation source terms in the numerical solution, we adopt a splitting approach. It is a simple but robust strategy since it allows to separate the contribution of relaxation terms from the reversible part of the time evolution equations. Here, we discuss the details of the implicit method that is used to solve the ordinary differential equations (ODE)

$$\frac{\mathrm{d}\mathbf{Q}_{i,j}}{\mathrm{d}t} = \mathbf{S}(\mathbf{Q}_{i,j}), \qquad t \in [t^n, t^{n+1}], \qquad \mathbf{Q}_{i,j}(t^n) = \mathbf{Q}_{i,j}^{(1)}. \tag{120}$$

In Section 5.3, the source terms were separated into $\mathbf{S}^{\mathrm{w}}(\mathbf{Q}_a)$, which contains the velocity relaxation terms and are stiff, but linear with respect to the relative velocity, and $\mathbf{S}^{\mathrm{s}}(\mathbf{Q}_a)$, which contains the strain relaxation terms of the distortion matrix $\mathbf{A}_a$, and which is non-linear and can be very stiff. The integration of these two different source terms is carried out with two different implicit approaches.

6.3.1 Relative velocity relaxation

In the following, we describe the system of ODEs arising from the source vector $\mathbf{S}^{\mathrm{w}}(\mathbf{Q})$ in (88), related to the relative velocity relaxation. Since there are zeros in $\mathbf{S}^{\mathrm{w}}(\mathbf{Q}_a)$ corresponding to the conservation equations of mass, volume fraction, and distortion matrix, they are remained constant over time in (120). Therefore, these quantities can be considered as constant parameters and can be omitted from the state vector $\mathbf{Q}_{i,j}$ of the initial value problem (120).

The integration of the remaining quantities, the phase momenta $\boldsymbol{u}_a$ and entropies s_a, is carried out in terms of the primitive state variables. More precisely, instead of (120) we consider the following reduced ODE system for the vector$\widetilde{\mathbf{V}} = (\boldsymbol{v}_1, \boldsymbol{v}_2, \boldsymbol{v}_3, s_1, s_2, s_3)$:

$$\frac{\mathrm{d}\widetilde{\mathbf{V}}_{ij}}{\mathrm{d}t} = \mathbf{S}(\widetilde{\mathbf{V}}_{ij}), \qquad t \in [t^n, t^{n+1}], \qquad \widetilde{\mathbf{V}}_{ij}(t^n) = \widetilde{\mathbf{V}}_{ij}^{(1)}, \tag{121}$$

where $\widetilde{\mathbf{V}}^{(1)}$ is the primitive variable reduced state vector obtained in (113) as the solution to the the homogeneous PDE system. The later ODE system can be easily integrated by means of the backward Euler method to obtain an updated solution $\widetilde{\mathbf{V}}^{(2)}$ at time t^{n+1}.

For instance, it can be seen that for each spatial direction x_k, $k = 1, 2$, one can decouple the phase velocity equations from the phase entropy ones, and this velocity subsystem reads

$$\begin{aligned}
\frac{\mathrm{d}v_{1,k}}{\mathrm{d}t} &= \lambda\Big(c_1(v_{1,k}-V_k) + c_2(v_{2,k}-V_k) + c_3(v_{3,k}-V_k) - (v_{1,k}-V_k)\Big),\\
\frac{\mathrm{d}v_{2,k}}{\mathrm{d}t} &= \lambda\Big(c_1(v_{1,k}-V_k) + c_2(v_{2,k}-V_k) + c_3(v_{3,k}-V_k) - (v_{2,k}-V_k)\Big),\\
\frac{\mathrm{d}v_{3,k}}{\mathrm{d}t} &= \lambda\Big(c_1(v_{1,k}-V_k) + c_2(v_{2,k}-V_k) + c_3(v_{3,k}-V_k) - (v_{3,k}-V_k)\Big),
\end{aligned} \tag{122}$$

where the phase kinetic coefficients $\lambda_{ab,k}$, that define the time scale for friction relaxation dissipative process in (51), are assumed to be equal throughout all phases and directions in this paper, i.e. $\lambda_{ab,k} = \lambda$. It is also usually assumed that this parameter is larger than $1/\Delta t$, where Δt is the time-step given by the stability condition in (119), and hence, we can say that we have a stiff ODE system, and an implicit discretization is needed. For such a system, in which all the sources are linear, the following discretization can be written for each cell Ω_{ij}

$$\begin{pmatrix} v_{1,k} \\ v_{2,k} \\ v_{3,k} \end{pmatrix}_{i,j}^{(2)} = (\mathrm{I} - \Delta t\mathcal{M})^{-1} \begin{pmatrix} v_{1,k} \\ v_{2,k} \\ v_{3,k} \end{pmatrix}_{i,j}^{(1)} \tag{123}$$

where the matrix inverse can be evaluated analytically, and after defining $\lambda^* = \Delta t \lambda$, it reads

$$(\mathrm{I} - \Delta t \mathcal{M})^{-1} = \frac{1}{1+\lambda^*} \begin{pmatrix} 1+\lambda^* c_1 & \lambda^* c_2 & \lambda^* c_3 \\ \lambda^* c_1 & 1+\lambda^* c_2 & \lambda^* c_3 \\ \lambda^* c_1 & \lambda^* c_2 & 1+\lambda^* c_3 \end{pmatrix}. \tag{124}$$

After that, it remains to solve the independent ODE subsystem for the phase entropies that reads

$$\begin{aligned} \frac{\mathrm{d}s_1}{\mathrm{d}t} &= \frac{\lambda c_1}{T_1} \Big(\big(v_{1,1} - V_1\big)^2 + \big(v_{1,2} - V_1\big)^2 + \big(v_{1,3} - V_1\big)^2 \Big), \\ \frac{\mathrm{d}s_2}{\mathrm{d}t} &= \frac{\lambda c_2}{T_2} \Big(\big(v_{2,1} - V_1\big)^2 + \big(v_{2,2} - V_1\big)^2 + \big(v_{2,3} - V_1\big)^2 \Big), \\ \frac{\mathrm{d}s_3}{\mathrm{d}t} &= \frac{\lambda c_3}{T_3} \Big(\big(v_{3,1} - V_1\big)^2 + \big(v_{3,2} - V_1\big)^2 + \big(v_{3,3} - V_1\big)^2 \Big), \end{aligned} \tag{125}$$

where we can use the updated velocities evaluated in (123). Finally, to discretize the three ODEs in (125), a generic implicit backward Euler time integrator based on Newton's method can be used in order to deal with the nonlinearity inherent to the definitions of the phase temperatures $T_a(\rho_a, s_a)$.

6.3.2 Strain relaxation

In contrast to the relative velocity relaxation subsystem (121), an accurate integration of the non-linear stiff source $\mathbf{S}^{\mathrm{s}}(\mathbf{Q})$ governing the strain relaxation of the distortion matrix $\boldsymbol{A}_a$ is a more challenging task, especially in the context of multiphase flows. Let us begin with some remarks on the evolution equations of the phase distortion fields $\boldsymbol{A}_a$, which we recall to be defined for each phase $a = 1, 2, 3$.

In the multiphase context, the evolution of the three distortion fields $\boldsymbol{A}_a$, $a =, 1, 2, 3$ given by

$$\partial_t \boldsymbol{A}_a + \nabla\big(\boldsymbol{A}_a \cdot \boldsymbol{v}_a\big) + \big(\nabla \boldsymbol{A}_a - \nabla \boldsymbol{A}_a^T\big) \cdot \boldsymbol{v}_a = -\frac{3}{\tau_a^{\mathrm{e}}} \left(\det \boldsymbol{A}_a\right)^{5/3} \boldsymbol{A}_a \mathrm{dev}\big(\boldsymbol{A}_a^T \boldsymbol{A}_a\big). \tag{126}$$

may occur over a very wide range of time scales in a single computational cell Ω_{ij}. Namely, there might be infinitely slow strain relaxation time scale ($\tau_a^{\mathrm{e}} = 10^{14}$) in an elastic solid phase and extremely fast relaxation of shear stresses in the inviscid ($\tau_a^{\mathrm{e}} = 10^{-14}$) and viscous fluid phase ($\tau_a^{\mathrm{e}} \sim 10^{-6} - 10^{-3}$). These different time scales are quantified by means of the relaxation time τ_a^{e} in the evolution equation of the phase distortion field

The interpretation of the strain relaxation timescale τ_A^{e} and its definition in the multiphase context were described in Section 5.2. From that description, it is clear that one of the major difficulties in solving the unified multiphase model of continuum mechanics is conditioned by the presence of these stiff and very non-linear strain relaxation source terms. Therefore, it is necessary to solve the associated ODE systems with care using an appropriate implicit time integrator.

Following the ideas in [55], an efficient and robust method for a semi-analytical implicit integration of the strain relaxation ODE systems was introduced by Chiocchetti and co-authors in [120] in the context of strain relaxation in the damaged solids, and further developed in [26, 25] for finite-rate pressure and strain relaxation in multiphase flows. The *key idea* of this time integrator is a reduction of the problem by using the *polar decomposition* for each phase distortion matrix $\boldsymbol{A}_a$:

$$\boldsymbol{A}_a = \boldsymbol{R}_a \, \boldsymbol{G}_a^{1/2} \qquad \text{with} \qquad \boldsymbol{G}_a^{1/2} = \boldsymbol{E}_a \, \hat{\boldsymbol{G}}_a^{1/2} \, \boldsymbol{E}_a^{-1}, \tag{127}$$

where $\boldsymbol{R}_a$ is an orthogonal matrix with a positive unit determinant, while the matrix square root $\boldsymbol{G}_a^{1/2}$ can be defined by means of eigen-decomposition of the symmetric positive definite matrix $\boldsymbol{G}_a$, where $\boldsymbol{E}_a$ is the matrix whose columns are eigenvectors and $\hat{\boldsymbol{G}}_a^{1/2}$ is the diagonal matrix whose diagonal elements are the roots of the eigenvalues.

Indeed, the distortion field $\boldsymbol{A}_a$ represents three local basis vectors representing the volume, shape, and the orientation of the phase control volume. Its 9 independent components (degrees of freedom), therefore, encodes two different types of information. Six degrees of freedom are strictly related to the definition of the stress tensor $\boldsymbol{\sigma}_a^{\mathrm{e}} = \varrho_a \mathrm{Cs}_a^2(\boldsymbol{G}_a \mathrm{dev} \boldsymbol{G}_a)$ via the six independent components of the metric tensor $\boldsymbol{G}_a$, and the three remaining degrees of freedom that define the angular orientation of the control volume.

Numerically, the matrix $\boldsymbol{G}_a^{1/2}$ can be simply evaluated using the Denman-Beavers algorithm. Thus, for any given state $\boldsymbol{A}_a$, one can easily compute $\boldsymbol{G}_a$, its square root $\boldsymbol{G}_a^{1/2}$, and eventually the inverse $\boldsymbol{G}_a^{-1/2}$. After that, the rotation matrix can be computed as

$$\boldsymbol{R}_a = \boldsymbol{A}_a \, \boldsymbol{G}_a^{-1/2}. \tag{128}$$

Moreover, the invariance of the rotational component of the distortion matrix under strain relaxation can be proven following the arguments in [55, 25], which means that during the strain relaxation step, one can use the evolution PDE for the metric tensor

$$\partial_t \boldsymbol{G}_a + \left(\nabla \boldsymbol{G}_a\right) \boldsymbol{v}_a + \boldsymbol{G}_a \nabla \boldsymbol{v}_a - (\nabla \boldsymbol{v}_a)^T \boldsymbol{G}_a = -\frac{6}{\tau_a^{\mathrm{e}}} \left(\det \boldsymbol{G}_a\right)^{5/6} \boldsymbol{G}_a \mathrm{dev} \boldsymbol{G}_a \ , \tag{129}$$

instead of the PDE for the full distortion matrix.

We now have all the ingredients to describe the following steps in order to obtain the final solution for the distortion matrix. First, we calculate the update $\boldsymbol{A}_a^{(1)}$ of the distortion matrix $\boldsymbol{A}_a$ obtained from the left hand side of the evolution equation (126), as presented in (113). From this solution, a rotation matrix can be calculated independently of the non-linear source terms as

$$\boldsymbol{R}_a^{(1)} = \boldsymbol{A}_a^{(1)} \, \boldsymbol{G}_a^{(1)\ -1/2} \quad \text{with} \quad \boldsymbol{G}_a^{(1)} = \left(\boldsymbol{A}_a^{(1)}\right)^T \boldsymbol{A}_a^{(1)}, \tag{130}$$

with $\boldsymbol{G}_a^{(1)\ -1/2}$ computed by means of the Denman-Beavers algorithm. Then, the following non-linear ODE system should be solved

$$\frac{\mathrm{d}\boldsymbol{G}_a}{\mathrm{d}t} = \boldsymbol{L}_a^{(1)} - \frac{6}{\tau_a^{\mathrm{e}}} \left(\ \det \boldsymbol{G}_a\right)^{5/6} \ \boldsymbol{G}_a \ \mathrm{dev} \ \boldsymbol{G}_a \ , \tag{131}$$

where $\boldsymbol{L}_a^{(1)}$ is a constant convective/productive forcing term evaluated simply as

$$\boldsymbol{L}_a^{(1)} = \frac{\boldsymbol{G}_a^{(1)} - \boldsymbol{G}_a^n}{\Delta t}, \quad \text{with} \quad \boldsymbol{G}_a^{(1)} = \left(\boldsymbol{A}_a^{(1)}\right)^T \boldsymbol{A}_a^{(1)}, \quad \boldsymbol{G}_a^n = \boldsymbol{G}_a\left(t^n\right). \tag{132}$$

This term, which takes into account the left-hand side of (129), is introduced to converge to the asymptotically correct state in the stiff limit of the equations. This alternative ODE problem (131) is then solved by computing the analytical solution of a sequence of linearized problems that approximate the original non-linear ODE, according to the procedure outlined in [25]. Once the source term applied to the metric tensor is integrated, and thus obtaining $\boldsymbol{G}_a^{(2)}$ at time t^{n+1}, the information can be mapped back to get the updated distortion field as

$$\boldsymbol{A}_a^{(2)} = \boldsymbol{R}_a^{(1)} \ \left(\boldsymbol{G}_a^{(2)}\right)^{1/2}. \tag{133}$$

6.4 Further remarks on the distortion field

Before assembling the final solution of the entire PDE system, we must make some important remarks concerning the challenges related to the numerical computation of the distortion field $\boldsymbol{A}_a$.

6.4.1 Algebraic determinant constraint

In the numerical solution of the evolution equation (127) for the phase distortion field $\boldsymbol{A}_a$, particularly when describing liquid phases, one must be careful with preserve the nonlinear algebraic constraint

$$\rho_a = \rho \mathrm{o}_a \det \boldsymbol{A}_a. \tag{134}$$

This constraint stems from the fact that the phase mass balance equation (77a) is the consequence of the time evolution (127) for the distortion matrix $\boldsymbol{A}_a$, see e.g. [52, 94]. Yet, in an Eulerian scheme, it is important to explicitly discretize the mass balance equation to ensure that it is fulfilled at the discrete level (important for the Rankine–Hugoniot conditions). Thus, the phase density can be computed by two means: from the mass balance equations and from (134). Therefore, to ensure that the solution is consistent with (134), this constraint must be actively enforced in the numerical scheme.

A simple but effective approach is to manually impose the constraint at each time iteration. Specifically, the distortion field obtained after solving the homogeneous problem is enforced to satisfy the ratio

$$\det \boldsymbol{A}_a^{(1)} = \frac{\rho_a^{(1)}}{\rho \mathrm{o}_a} \tag{135}$$

as detailed in [25].

6.4.2 Linear combination of pure rotational fields

Numerical discretization, in all its parts from data representation to explicit discretization with the FV update formula, is applied to the vector and tensorial quantities in a component-wise manner. This is not a problem for the velocity field, but the distortion field requires more attention due to its rotational component. From our experience, an improper treatment of the rotational matrix $\boldsymbol{R}_a$ can lead to artificial stresses and other numerical artifacts.

It is clear that even in the case of a simple component-by-component linear combination of two rotational matrices, such as that presented by an average operator for example, the resulting matrix is a rotational matrix only in the case of infinitesimal rotations. However, the additivity rule does not in general hold for finite rotations. For example, we have observed in our numerical experiments, in which the solution of the distortion field is not particularly smooth, that simple averaging of the rotational matrices results in artificial stresses. This happened in tests such as the lid-driven cavity test, Sec. 7.5 if no special treatment is applied. In this test, the boundary conditions produce a velocity gradient singularity at the corners of the cavity, which results in a locally discontinuous distortion field. On the other hand, no issue arises in the double shear layer problem, Sec. 7.4. For this reason, a different approach would be required to describe the rotational component of the information encoded by $\boldsymbol{A}_a$, by means of a auxiliary mathematical representation of these quantities that allows a component-by-component treatment even for rotations of finite amplitude.

Thus, in this paper, we propose a simple but effective approach to address this issue. It employs the efficiency of the Chiocchetti semi-analytical solver [25] in the infinitely stiff relaxation regime, $\tau_a^{\mathrm{e}} \to 0$. In particular, in this limit, the strains encoded in the metric tensor $\boldsymbol{G}_a$ dissipate almost

instantaneously, resulting in a distortion field that is represented by a pure rotation matrix, i.e. $\boldsymbol{A}_a = \boldsymbol{R}_a$ and $\boldsymbol{G}_a = \boldsymbol{I}$.

Therefore, the idea of decoupling of the evolution of the two types of information encoded in $\boldsymbol{A}_a$ (at least numerically) is straightforward. This can be done by adding an auxiliary evolution equation (126) for a new auxiliary distortion field $\widetilde{\boldsymbol{A}}_a$ subject to a relaxation timescale $\tilde{\tau}_a^{\mathrm{e}} \to 0$. This auxiliary distortion field $\widetilde{\boldsymbol{A}}_a$ carries only the information about the rotational component of the original distortion $\boldsymbol{A}_a$, i.e. $\widetilde{\boldsymbol{A}}_a = \widetilde{\boldsymbol{R}}_a$. Moreover, thanks to this almost instantaneous relaxation (numerically we use $\tilde{\tau}_a^{\mathrm{e}} = 10^{-14}$), the artificial stresses that may arise from the combination of finite amplitude rotations are dissipated instantaneously, both at the level of the predictor, Sec. 6.1, and at the level of the final solution at each time-step, Sec. 6.2 and Sec. 6.3.

On the other hand, due to this decoupling, the original distortion field $\boldsymbol{A}_a$ at each time step carries only the information about the strains, i.e. $\boldsymbol{A}_a = \boldsymbol{G}_a^{1/2}$ and $\boldsymbol{R}_a = \boldsymbol{I}$, both at the level of the predictor and the solution updated at time t^{n+1}. Therefore, expression (133), in the source term integration process for the original distortion field $\boldsymbol{A}_a$, should be rewritten as

$$\boldsymbol{A}_a^{(2)} = \boldsymbol{I} \left(\boldsymbol{G}_a^{(2)} \right)^{1/2} . \tag{136}$$

6.5 Final solution for the complete problem

The final solution $\mathbf{Q}_{i,j}^{n+1}$ of the complete problem (78) can now be retrieved by considering the solution of the homogeneous problem, the contribution of the source terms, and the remarks on rotational matrices discussed above. Thus, including formally the auxiliary phase distortion field $\widetilde{\boldsymbol{A}}_a$ to the set of state parameters, the final solution of each phase $a = 1, 2, 3$ reads

$$\mathbf{Q}_{a,i,j}^{n+1} = \left(\varrho_a^{(1)}, \boldsymbol{u}_a^{(2)}, s_a^{(2)}, \alpha_a^{(1)}, \boldsymbol{A}_a^{(3)}, \widetilde{\boldsymbol{A}}_a^{(2)} \right)_{i,j} , \tag{137}$$

where the complete phase distortion field $\boldsymbol{A}_a^{(3)}$ is computed as

$$\boldsymbol{A}_a^{(3)} = \widetilde{\boldsymbol{R}}_a^{(1)} \ \left(\boldsymbol{G}_a^{(2)} \right)^{1/2} . \tag{138}$$

7 Numerical results

This section provides the results obtained with the numerical scheme presented in Section 6 addressing the three-phase reduced BN-type SHTC model presented in 5.3. The numerical scheme developed in this work considers the entropy inequalities of each phase (77e), instead of the phase energy balance laws as in the most existing finite-volume discretizations. This choice was made in order to make the mathematical model less complex. Indeed, the phase entropy balance laws have a much simpler structure than the energy balance laws. This, however, comes with the price that such a numerical scheme can not be applied to problems with high Mach number. In particular, the following numerical test problems also aim to demonstrate that considering the phase entropy balance laws rather than phase energy ones leads to negligible errors for problems with relatively *weak shocks*. Also, it should be emphasized that our future intention is to develop a numerical scheme more suited to the original SHTC formulation (47), i.e. the thermodynamically compatible (HTC) type schemes where the fully-discrete energy conservation is obtained as a mere consequence of the discretized PDEs, see e.g. [1, 125, 21].

Furthermore, the presented results consist of a wide range of benchmarks and problems that may occur in real life problems involving several phases. Some results demonstrate the solution of the multiphase model in a single-phase limit, and in the relaxation limits of the GPR model, e.g.

the inviscid and viscous fluid, as well as in the limit of nonlinear elasticity and plasticity. In all the cases, the numerical results are comparable with results obtained from established standard models, i.e. the Euler or Navier-Stokes equations for fluids, or the classical hypo-elastic model with plasticity, but, notably, in our case the solution is obtained within the unified multiphase model of continuum mechanics.

In all the tests, the time step Δt is computed according to the CFL condition expressed in (119), in order to guarantee the stability of the explicit FV time-stepping. Furthermore, the initial conditions for volume fractions are defined with respect to a minimum value $\alpha_{\min} = \epsilon = 10^{-6}$; i.e. when a-th phase is not present in a given computational cell, the volume fraction of that phase is set to $\alpha_a = \alpha_{\min}$.

7.1 Numerical convergence study

A numerical convergence study is presented by solving the isentropic vortex problem proposed in [5, 63], considering the one-phase limit of the model: $\alpha_1 = 1 - 2\epsilon$, $\alpha_2 = \epsilon$, $\alpha_3 = \epsilon$. For this problem, there is an exact analytical solution for the compressible Euler equations, i.e. in the stiff inviscid limit $\tau_1^{\mathrm{e}} \to 0$ of the SHTC BN-model considered in this work. The initial condition consists of a linear superposition of a homogeneous background field and some δ perturbations, which in terms of primitive variables for the first phase read

$$\mathbf{V}_1 = (1 + \delta\rho_1, 1 + \delta v_{1,1}, 1 + \delta v_{1,2}, 1 + \delta p_1, 1 - 2\epsilon, \boldsymbol{I}), \tag{139}$$

where the phase distortion field is initially set equal to the identity, while the quantities for the absent phases are set in the same way except for the volume fractions. The computational domain is $\Omega = [0; 10] \times [0; 10]$ and periodic boundary conditions are applied everywhere. In this domain, the perturbations of velocities $\delta v_{1,k}$ and temperature δT_1 are given by

$$\begin{pmatrix} \delta v_{1,1} \\ \delta v_{1,2} \end{pmatrix} = \frac{5}{2\pi} e^{0.5(1-r^2)} \begin{pmatrix} 5 - y \\ x - 5 \end{pmatrix}, \qquad \delta T_1 = -\frac{(\gamma_1 - 1)5^2}{8\gamma_1 \pi^2} e^{1-r^2}, \tag{140}$$

where r is the distance frm the center of the vortex. Aditionally, because we are considering an isentropic vortex, it is assumed that the perturbation of the entropy δs_1 is zero, hence the perturbations for density and pressure result in

$$\delta\rho_1 = (1 + \delta T_1)^{\frac{1}{\gamma_1 - 1}} - 1, \qquad \delta p_1 = (1 + \delta T_1)^{\frac{\gamma_1}{\gamma_1 - 1}} - 1. \tag{141}$$

The exact analytical solution of the problem represented by these initial conditions for the compressible Euler equations is represented simply by the time-shifted initial conditions (140), (141), convected following the mean velocity $\bar{\boldsymbol{v}} = (1, 1)$. The equation of state parameters that remain to be defined are assumed to be $\gamma_1 = 1.4$, $\mathrm{Cv}_1 = 1$, $\mathrm{Cs}_1 = 0.5$, $\tau_1^{\mathrm{e}} = 10^{-14}$.

This test is performed up to a final time of $t = 1.0$ using a sequence of successively refined equidistant meshes composed of $\mathrm{N}_x \times \mathrm{N}_y$ control volumes. The L^1 and L^2 error norms at the final time for the density ρ_1, the velocity component $v_{1,1}$ and the phase entropy s_1 are shown in Tab. 1 and Tab. 2 together with the corresponding convergence rates. From the results shown in the tables, it can be seen that second-order accuracy is achieved for this inviscid problem, i.e. in the stiff limit of the governing PDE system.

7.2 Shear motion in solids and fluids

In the context of this work, this test has a twofold purpose of showing that the unified model for fluid and solid mechanics and the developed numerical scheme can indeed model the behavior

$N_x \times N_y$	$L^1_{\rho_1}$	$L^1_{v_{1,1}}$	$L^1_{s_1}$	$\mathcal{O}_{\rho_1}$	$\mathcal{O}_{v_{1,1}}$	$\mathcal{O}_{s_1}$
32	2.5094E-1	5.1290E-1	1.3009E-2			
64	5.2676E-2	1.1826E-1	5.4240E-3	2.25	2.11	1.26
128	1.0012E-2	2.7041E-2	9.9400E-4	2.39	2.12	2.44
256	1.8412E-3	6.3160E-3	1.5781E-4	2.44	2.09	2.65

Tab. 1: Mesh elements, L^1-error norms and their respective numerical convergence rates for the density ρ_1, the velocity component $v_{1,1}$ and the phase entropy s_1, applied to the isentropic vortex problem.

$N_x \times N_y$	$L^1_{\rho_1}$	$L^1_{v_{1,1}}$	$L^1_{s_1}$	$\mathcal{O}_{\rho_1}$	$\mathcal{O}_{v_{1,1}}$	$\mathcal{O}_{s_1}$
32	6.6187E-2	1.3959E-1	4.4700E-3			
64	1.4075E-2	3.4710E-2	2.3585E-3	2.23	2.01	0.93
128	2.6702E-3	8.5657E-3	4.9292E-4	2.40	2.02	2.26
256	4.8569E-4	2.0754E-3	7.6455E-5	2.46	2.05	2.69

Tab. 2: Mesh elements, L^2-error norms and their respective numerical convergence rates for the density ρ_1, the velocity component $v_{1,1}$ and the phase entropy s_1, applied to the isentropic vortex problem.

of viscous fluids and elastic solids at once. We consider a simple shear motion in solids and fluids in the single-phase limit of the entire multiphase model: $\alpha_1 = 1 - 2\epsilon$, $\alpha_2 = \epsilon$, $\alpha_3 = \epsilon$. Similar to the previous section 7.1, the time evolution of an incompressible shear layer is one of the few test problems for which the exact analytical solution of the non-stationary Navier-Stokes equations is known, and for the velocity component $v_{1,1}$ is given by the following error function

$$v_{1,1}(x,y,t) = v_{1,1}(x,y,0)\,\mathrm{erf}\left(\frac{1}{2}\frac{x}{\sqrt{\nu_1 t}}\right). \tag{142}$$

However, because we are discretizing compressible equations with an explicit scheme, the best we can do is to simulate the problem at sufficiently low Mach number, e.g. $\mathrm{M}_1 = 0.1$ was sufficient to obtain an almost incompressible behavior.

The computational domain is $\Omega = [-0.5; 0.5] \times [-0.0625; 0.0625]$, with the opposite velocities imposed on the left and right halfs of the domain in the x-direction, while we use periodic boundary conditions in the y-direction. The initial conditions of the problem for the first phase, are given by

$$\begin{aligned} &\alpha_1 = 1 - 2\epsilon, \quad \rho_1 = 1, \quad p_1 = \frac{1}{\gamma_1}, \quad \boldsymbol{A}_1 = \boldsymbol{I} \\ &v_{1,1} = 0, \quad v_{1,2}(x,y) = \begin{cases} +0.1 & \text{if} \quad x > 0, \\ -0.1 & \text{if} \quad x \leq 0. \end{cases} \end{aligned} \tag{143}$$

with the physical parameters set to $\gamma_1 = 1.4$, $\mathrm{Cv}_1 = 1$, $\mathrm{Cs}_1 = 1$. The strain relaxation time $\tau_1^{\mathrm{e}} = 6\nu_1/\mathrm{Cs}_1^2$ is chosen according to (50) for various values of the fluid kinematic viscosity ν_1, while for the elastic solid limit is set to $\tau_1^{\mathrm{e}} = 10^{14}$.

For the elastic solid limit, this initial condition leads to two shear waves travelling to the left and right with the shear sound speed. In this case, a reference solution for the solid limit was obtained for the single-material GPR model using a classical second-order MUSCL-Hancock scheme [126] on a fine mesh of 32000 cells, as done in [21].

Simulations are carried out on a grid composed of 256×32 control volumes up to a final time of $t = 0.4$. The comparison between the numerical results and the previously mentioned reference

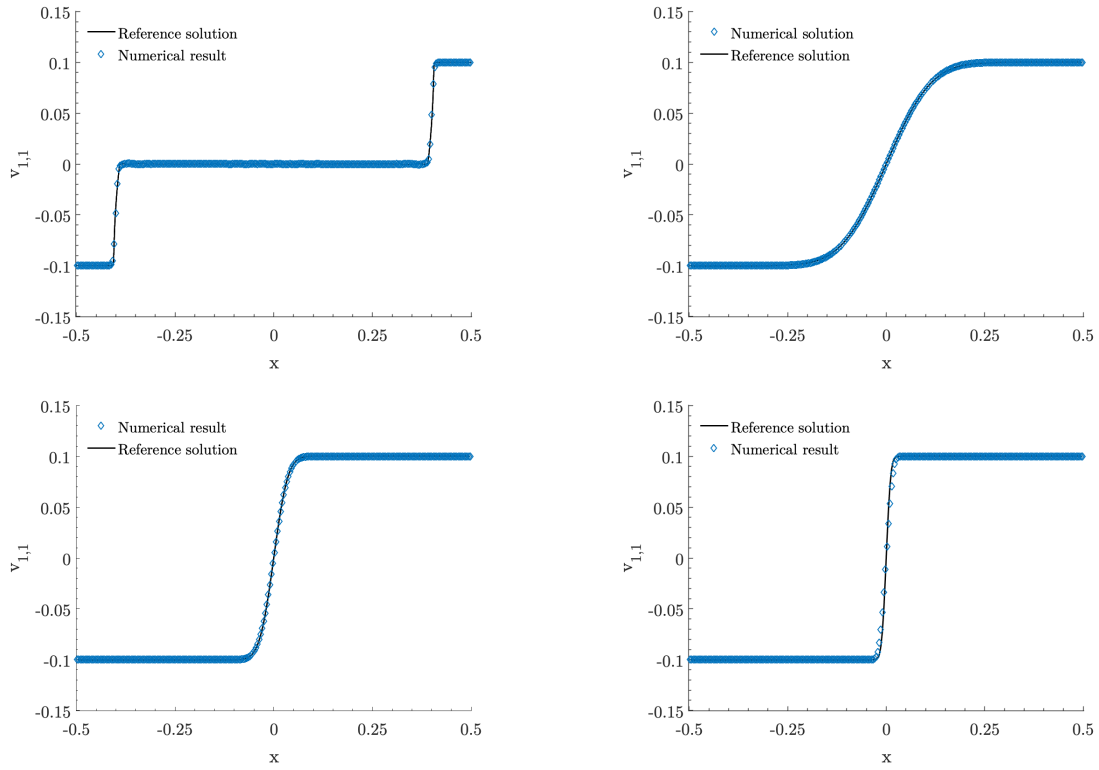

Fig. 1: Numerical solution at time $t = 0.4$ obtained with the explicit FV scheme for compressible multiphase fluid and solid mechanics applied to a simple shear flow in fluids and in an elastic solid. Results for the solid limit (top left) and for fluids with different viscosities $\nu_1 = 10^{-2}$ (top right), $\nu_1 = 10^{-2}$ (bottom left) and $\nu_1 = 10^{-2}$ (bottom right). For fluids, the analytical solution of the first problem of Stokes is used as the reference solution.

solutions is presented in Fig. 1, where an excellent agreement between the two solutions can be observed for both solid and fluid behaviour.

7.3 Riemann problems

We continue the validation of our numerical scheme with a set of Riemann problems to quantify the error encountered by considering the balance equations of phase entropies rather than of the phase energies, and to see that the correct wave structure can still be reproduced for problems with relatively weak shocks. In this section, we solve a series of Riemann problems with initial data according to Tab. 3, for the Euler equations of compressible gas dynamics, which can be retrieved in the stiff relaxation limit $\tau_1^{\mathrm{e}} \to 0$.

RP	ρ_1^L	$v_{1,1}^L$	$v_{1,2}^L$	P_1^L	ρ_1^R	$v_{1,1}^R$	$v_{1,2}^R$	P_1^R
RP1	1.0	0.0	0.0	1.0	0.125	0.0	0.0	0.1
RP2	1.0	0.75	0.0	1.0	0.125	0.0	0.0	0.1
RP3	1.0	0.0	-0.2	1.0	0.5	0.0	0.2	0.5

Tab. 3: Left initial state (L) and right initial state (R) for the quantities related to the first phase. In particular the density ρ_1, velocity $\boldsymbol{v} = (v_{1,1}, v_{1,2}, 0)$ and pressure P are defined for three different Riemann problems. These Riemann problems (RP1), (RP2) and (RP3) can be referred to the solution of the Euler equations, i.e. $\tau_1^{\mathrm{e}} = 10^{-14}$.

The computational $\Omega = [-0.5; 0.5] \times [-0.0625; 0.0625]$ is partitioned into two regions with constant states, left (L) and right (R), separated by a discontinuity normal to the x-direction, located at x_d. The distortion field is initially set equal to the identity $\boldsymbol{A}_1 = \boldsymbol{I}$, while the equation of state parameters are taken as $\gamma_1 = 1.4$, $\mathrm{Cv}_1 = 1.0$, $\mathrm{Cs}_1 = 1.0$ and Riemann problems. Simulations are carried out on a grid composed of 512×64 control volumes up to a final time of $t = 0.2$.

In Figure 2, the one-dimensional profiles of the density ρ_1, the x-component of the velocity field $v_{1,1}$ and pressure p_1 for the Riemann problems RP1 ($x_d = 0$) and RP2 ($x_d = -0.2$) are shown. The results are compared with the exact solution of the compressible Euler equations. From the results it can be observed that the correct wave structure is overall reproduced properly for the Riemann problem RP1, while as the shock wave becomes stronger, as for RP2, the error introduced due to the use of phase entropy balance laws increases. This is why we limit ourselves to low Mach number flows, and RP2 clearly demonstrates the well-known fact that satisfying the conservation of energy is essential to correctly solve problems involving shock waves. RP2 was proposed by Toro in [126] and includes a sonic rarefaction, however this test cases is well resolved and does not present any sonic glitches.

The numerical results obtained for the Riemann problem RP3 ($x_d = 0$) is shown in Fig. 3. In this case, the shock present is even weaker, the solution is very close to an isoentropic one, and therefore the numerical solution is in very good agreement with the exact one.

7.4 Double shear layer problem

The numerical scheme is now applied to solve the double shear layer test problem, see e.g. [8, 39, 122, 21, 25]. It is another classical benchmark problem which is useful for the validation of the model and numerical algorithm on viscous flows. Here, the model is still considered in the single-phase limit with the volume fractions taken as $\alpha_1 = 1 - 2\epsilon$, $\alpha_2 = \epsilon$, $\alpha_3 = \epsilon$. For this test, the 2D computational domain is $\Omega = [0; 1]^2$, with periodic boundary conditions imposed everywhere.

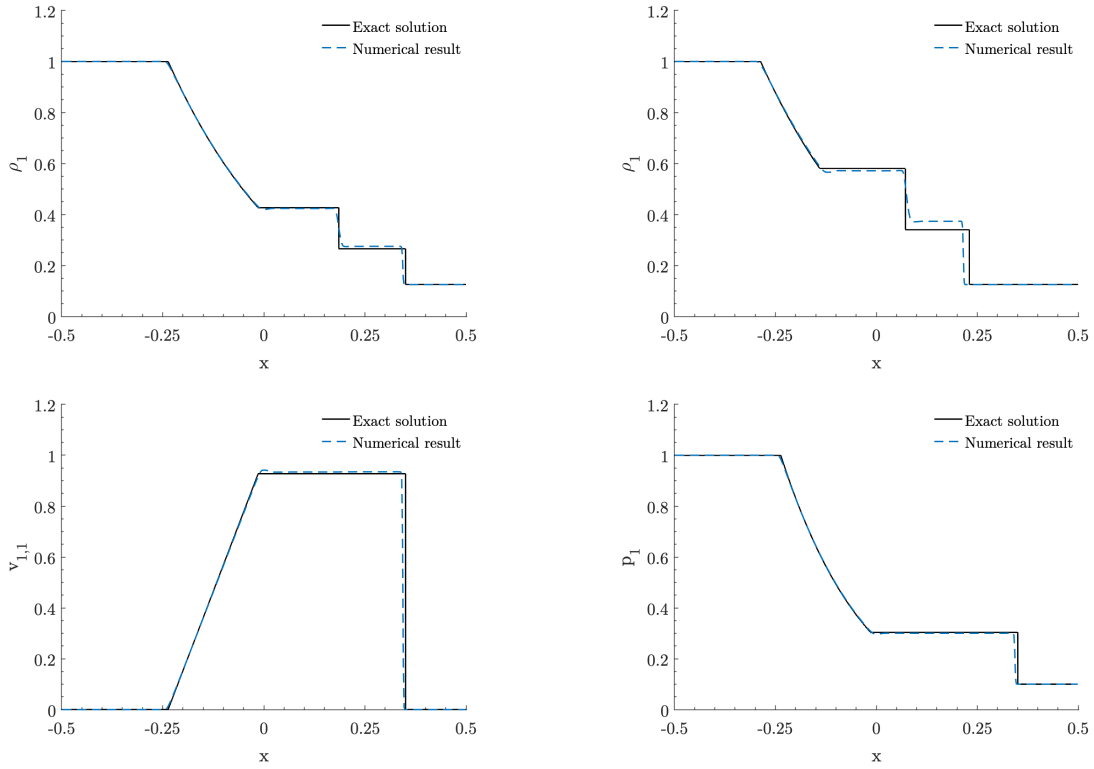

Fig. 2: Numerical results (dashed line) for density ρ_1, velocity component $v_{1,1}$ and pressure p_1 in the inviscid limit $\tau_1 = 10^{-14}$, for the Riemann problem RP1 ($x_d = 0$) (top left, bottom left and right), for the Riemann problem RP2 ($x_d = -0.2$) (top right). The exact solution of the compressible Euler equations (black solid line).

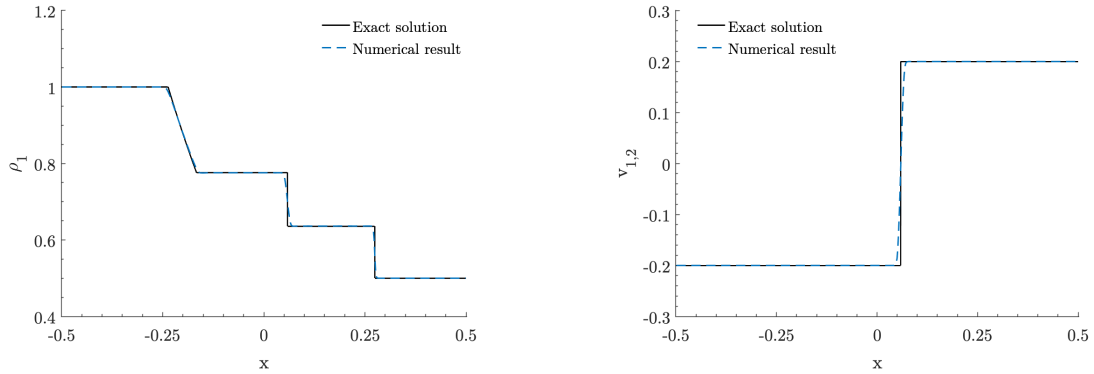

Fig. 3: Numerical results for density ρ_1 and velocity component $v_{1,2}$ in the inviscid limit $\tau_1 = 10^{-14}$, at time $t = 0.2$, for the Riemann problem RP3 ($x_d = 0$) (dashed line). The exact solution of the compressible Euler equations (black solid line).

The initial conditions contain a steep velocity gradient and are defined as follows

$$\begin{aligned} &\alpha_1 = 1 - 2\epsilon, \quad \rho_1 = 1, \quad p_1 = \frac{100}{\gamma_1}, \quad \boldsymbol{A}_1 = \boldsymbol{I}, \\ &v_{1,1}(x,y) = \begin{cases} \tanh\big((y-0.25)\bar{\rho}\big), & \text{if} \quad x \leq 0.5, \\ \tanh\big((0.75-y)\bar{\rho}\big), & \text{if} \quad x > 0.5, \end{cases} \\ &v_{1,2}(x,y) = \delta \sin(2\pi x), \end{aligned} \tag{144}$$

where the parameters that determine the shape of the velocity field are set to $\delta = 0.05$ and $\bar{\rho} = 30$. The other physical parameters are assumed to be $\gamma_1 = 1.4$, $\mathrm{Cv}_1 = 1$, $\mathrm{Cs}_1 = 8.0$ while two different viscosity coefficients were set in two separate runs of the test problem, $\nu_1 = 2 \times 10^{-3}$ ($\mathbb{R}\mathrm{e} \simeq 1000$) and $\nu_1 = 2 \times 10^{-4}$ ($\mathbb{R}\mathrm{e} \simeq 10000$) respectively, which result in $\tau_1^{\mathrm{e}} = 1.875 \cdot 10^{-4}$ and $\tau_1^{\mathrm{e}} = 1.875 \cdot 10^{-5}$, respectively.

Simulations are carried out up to a final time of $t = 1.8$ on a grid consisting of 1280×1280 control volumes. Figure 4 shows the time evolution of the $A_{1,12}$ component of the distortion field at times $t = 1.2$ (top), $t = 1.6$ (center) and $t = 1.8$ (bottom), for the two different viscosity coefficients considered (left) and (right), respectively. The dynamics of the flow, as already described in [8, 39, 122, 21, 25], is represented by the evolution of the initially perturbed shear layers into different vortices, which exhibit particularly complex flow structures.

The results in Fig. 4, highlight the incredible capability of the distortion field to describe the details of the flow structures, which in particular are encoded in the rotational component $\boldsymbol{R}_1$ of the distortion field $\boldsymbol{A}_1$. The results obtained are in excellent agreement with those obtained in [21], where a thermodynamically compatible scheme is used and with those in [25] obtained through a semi-implicit structure-preserving scheme, despite the fact that in these works a four times finer grid was used.

7.5 Lid-driven cavity

As a last numerical test considering a single-phase limit of the full model, we present the lid-driven cavity problem, see [49]. It is a classical benchmark problem for numerical methods applied to incompressible Navier-Stokes equations, see [121], however it can be used to validate compressible flow solvers in the low Mach number regime [37, 123, 9]. Moreover, it has already been successfully solved with the GPR model in [39, 12] with a discontinuous Galerkin and a semi-implicit scehem, and with a thermodynamically compatible scheme in [21]. However, in these works, high-order schemes or schemes that make use of a particular time or structure-preserving discretizations have been used, e.g. on staggered grid or thermodynamically compatible discretization. These could be the reasons why it would appear that the problem associated with the discretization, i.e. the combination, of purely rotational fields presented in Sec. 6.4 does not arise in these works, whereas it does for the classical MUSCL-Hancock discretization, specifically in this test where the boundary conditions produce a velocity gradient singularity in the corners.

The computational domain is given by $\Omega = [-0.5; 0.5] \times [-0.5; 0.5]$ and the initial condition are simply

$$\alpha_1 = 1 - 2\epsilon, \quad \rho_1 = 1, \quad \boldsymbol{v}_1 = \boldsymbol{0}, \quad p_1 = \frac{100}{\gamma_1}, \quad \boldsymbol{A}_1 = \boldsymbol{I}. \tag{145}$$

The fluid flow inside the cavity is driven by the lid on the upper boundary, whose velocity is set to $v_{1,1} = 1$, resulting in the Mach number $\mathrm{M}_1 = 0.1$. On all the other boundaries, a no-slip wall boundary condition with $\boldsymbol{v}_1 = 0$ has been be imposed. Furthermore, the parameters of the model

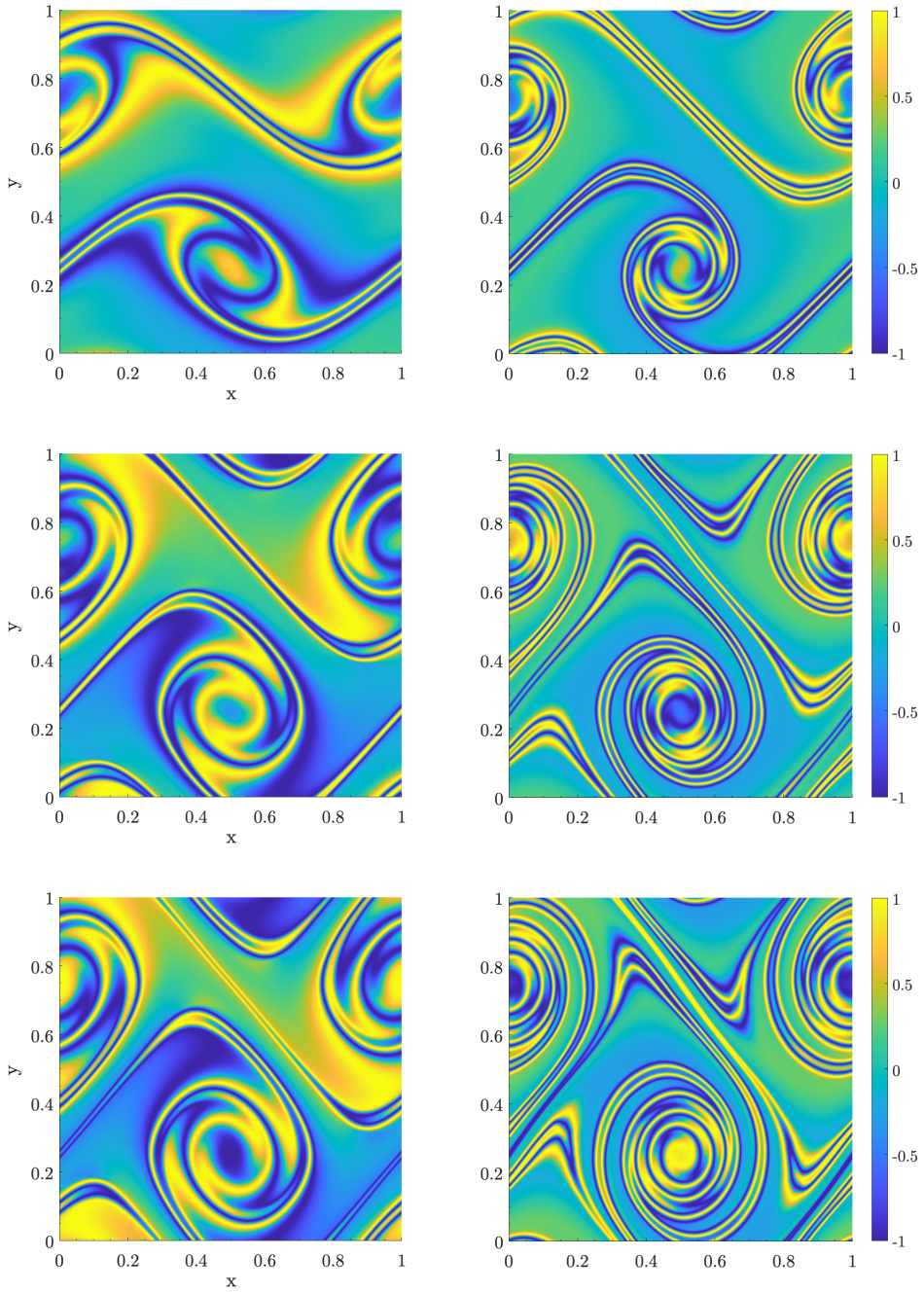

Fig. 4: Filled contours of one component of the distortion field $\boldsymbol{A}_1$, namely of the $A_{1,12}$ component, for the double shear layer problem at times $t = 1.2$ (top), $t = 1.6$ (center) and $t = 1.8$ (bottom); for two values of kinematic viscosity $\nu_1 = 2 \times 10^{-3}$ ($\mathbb{R}\mathrm{e} \simeq 1000$) (left) and $\nu_1 = 2 \times 10^{-4}$ ($\mathbb{R}\mathrm{e} \simeq 10000$) (right).

are set to $\gamma_1 = 1.4$, $\mathrm{Cv}_1 = 1$, $\mathrm{Cs}_1 = 8.0$ and the kinematic viscosity is chosen as $\nu_1 = 10^{-2}$ so that the Reynolds number of the test problem is $\mathbb{R}\mathrm{e} = 100$.

Simulations are carried out up to a final time of $t = 10$ on a grid consisting of 512×512 control volumes. To correctly set the no-slip wall boundary conditions, it is necessary to compute and prescribe a specific distortion field $\boldsymbol{A}_{BC}$ using the values taken in the edge-adjacent cell. First, the information encoded by the distortion field is expressed through $\boldsymbol{R}_{BC\,(1)}$ and $\boldsymbol{G}_{BC\,(1)}$, by means of a polar decomposition. Subsequently, the inverse of the rotational component can be easily evaluated as $\boldsymbol{R}^{-1}_{BC\,(1)} = \boldsymbol{R}^{T}_{BC\,(1)}$. At this point the information can be mapped back to obtain the boundary condition for the distortion field as

$$\boldsymbol{A}_{BC} = \boldsymbol{R}^{T}_{BC\,(1)}\, \boldsymbol{G}^{1/2}_{BC\,(1)}. \tag{146}$$

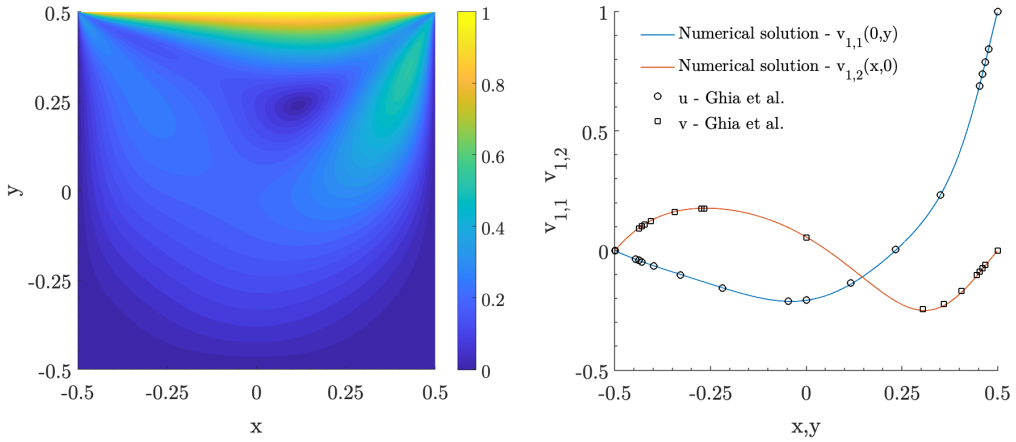

Fig. 5: Lid driven cavity at Reynolds number $\mathbb{R}\mathrm{e} = 100$. Numerical results obtained at time $t = 10.0$. Colour contours of the velocity module (left), and a comparison with the reference solution of Ghia et al. [49] of the velocity components $v_{1,1}$ and $v_{1,2}$ for 1D cuts along the x and y axis.

Figure 5 shows the computational results obtained using the approach described in section 6.4. This approach separates the evolution of the two types of information encoded in $\boldsymbol{A}_a$ and leverages the capabilities of a semi-analytical solver to efficiently solve the equations in the stiff relaxation regime. Excellent agreement between the numerical solution and the Navier-Stokes reference solution of Ghia et al. [49] was obtained. Also for this test, Fig. 6 shows the time evolution of the $A_{1,12}$ component of the distortion field. It can again be seen that the distortion field components are excellent candidates for flow visualisation, revealing in detail the evolution of the flow and keeping track of the rotations that the fluid element undergoes over time.

7.6 Elastic vibrations of a beryllium plate

From this section, we begin to test the multiphase property of the governing equations and the ability of the model to describe the solid and fluid branches of continuum mechanics in a single PDE system. In the following test problem, we simulate the vibrations of an edely elastic beryllium plate subjected to an initial velocity perturbation. The setup follows [112, 75, 17, 13, 92], but with the notable modification. Namely, instead of considering a solid body in a vacuum, we consider

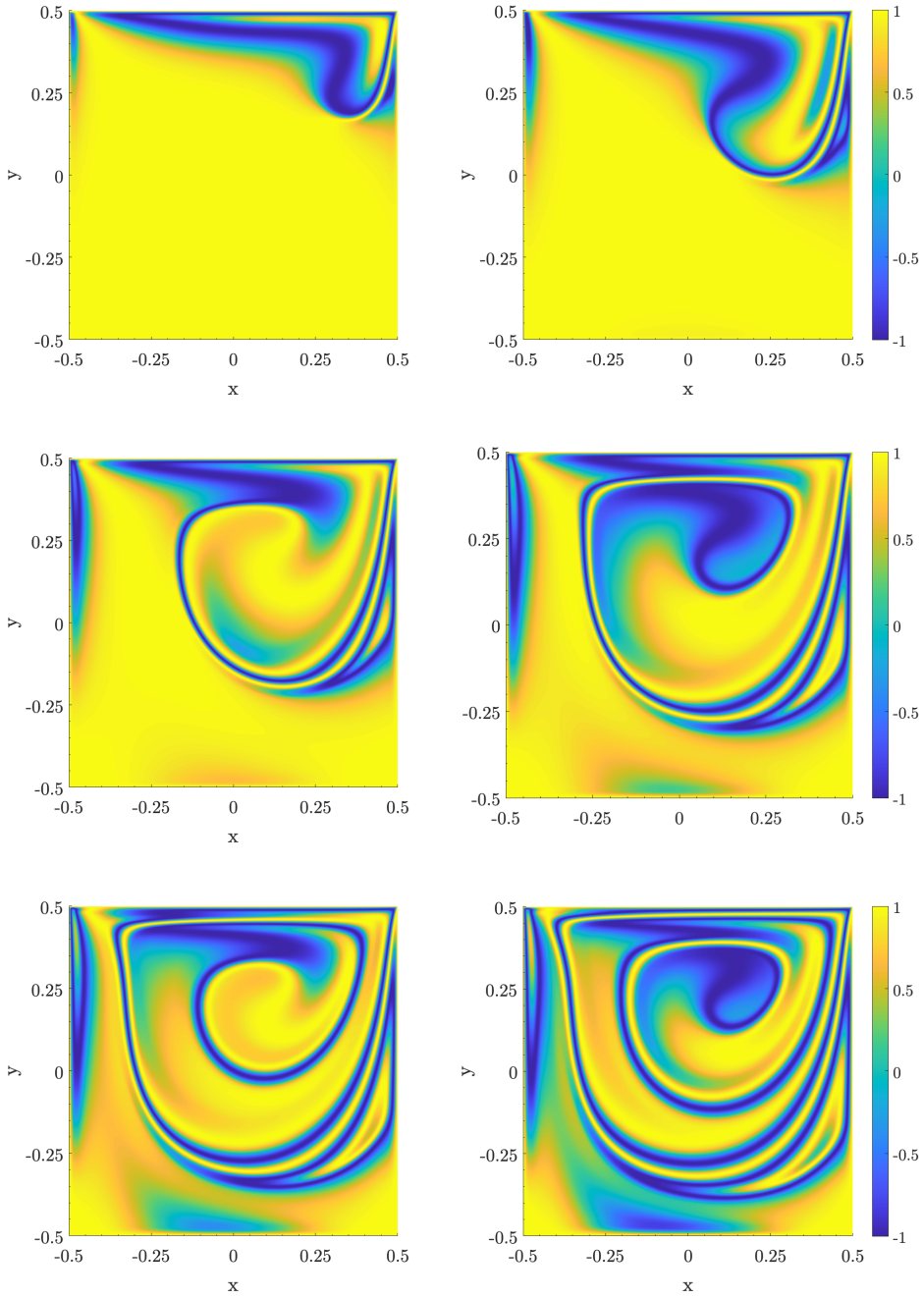

Fig. 6: Filled contours of one component of the distortion field $\boldsymbol{A}_1$, namely of the $A_{1,12}$ component, for the lid-driven cavity problem at $\mathbb{R}\mathrm{e} = 100$, at times $t = 1.0, t = 2.0$, (top), $t = 4.0, t = 6.0$, (center) and $t = 8.0, t = 10.0$ (bottom).

a solid body in a gas, and thus we need to define two separate density fields via their respective volume fractions.

Compared to the Lagrangian setup, used in the previously mentioned works, the computational domain considered here is larger, as in [18], and is assumed to be $\Omega = [-4.0; 4.0] \times [-2.0; 2.0]$ and the initial conditions for the first phase (the solid) are

$$\alpha_1(x,y) = \begin{cases} 1-2\epsilon & \text{if } \boldsymbol{x} \in \Omega_1, \\ \epsilon & \text{if } \boldsymbol{x} \notin \Omega_1, \end{cases} \quad \boldsymbol{v}_1(x,y) = \begin{cases} (0, \boldsymbol{v}_{1,2}) & \text{if } \boldsymbol{x} \in \Omega_1, \\ (0,0) & \text{if } \boldsymbol{x} \notin \Omega_1, \end{cases} \tag{147}$$
$$\rho_1 = 1.845, \quad p_1 = 10^{-4}, \quad \boldsymbol{A}_1 = \boldsymbol{I},$$

while the second phase (the gas) is initialised as follows

$$\alpha_2(x,y) = \begin{cases} \epsilon & \text{if } \boldsymbol{x} \in \Omega_1, \\ 1-2\epsilon & \text{if } \boldsymbol{x} \notin \Omega_1, \end{cases} \tag{148}$$
$$\rho_2 = 10^{-3}, \quad \boldsymbol{v}_2 = \boldsymbol{0} \quad p_2 = 10^{-4}, \quad \boldsymbol{A}_2 = \boldsymbol{I},$$

where $\Omega_1 = [-3.0; 3.0] \times [-0.5; 0.5]$ is the subdomain that defines the initial geometry of the beryllium bar, and the initial vertical velocity component $\boldsymbol{v}_{1,2}$, according to Boscheri et al. [13], is given as

$$\boldsymbol{v}_{1,2}(x) = C_1\omega\big(C_2(\sinh(C_3(x+3)) + \sin(C_3(x+3))) - C_4(\cosh(C_3(x+3)) + \cos(C_3(x+3)))\big) \tag{149}$$

with $C_3 = 0.7883401241$, $C_2 = 0.2359739922$, $C_1 = 0.004336850425$, $C_4 = 57.64552048$ and $C_2 = 56.53585154$. The third phase has $\alpha_3 = \epsilon$. The other parameters and physical quantities that define the properties of the beryllium material and that are required to use the stiffened-gas EOS (29) are chosen as $\gamma_1 = 1.4$, $\mathrm{Cv}_1 = 1000$, $\mathrm{Cs}_1 = 0.905$, $\rho\mathrm{o}_a = 1.845$, $\mathrm{Co}_1 = 1.287$ and $p\mathrm{o}_1 = p_1$. Additinally, to have an ideal elastic material we set $\tau_1^{\mathrm{e}} = 10^{14}$. For the gas phase surrounding the solid phase, the EOS of ideal gases is used and the physical parameters are $\gamma_2 = 1.2$, $\mathrm{Cv}_2 = 1000$, $\mathrm{Cs}_2 = 1.0$ and $\nu_2 = 10^{-4}$.

The simulation is carried out up to the final time $t_f = 53.2$ which corresponds approximately to two complete periods of vibration and the computational domain is discretized with an uniform Cartesian mesh composed of 1024×512 control volumes. In contrast to Lagrangian schemes, it is not necessary to impose boundary conditions on the surface of the solid, as the solid-gas boundary condition is directly taken into account within the governing PDE system. Hence, in our simulation, periodic boundaries are set everywhere.

In Fig. 7, we represent the contour map of the volume fraction α_1, which represents the geometry of the bar at time $t = 8$ and in the same figure, we also depict the time evolution of the vertical velocity component $v_{1,2}(0,0,t)$ at $\bar{\boldsymbol{x}} = (0,0)$, i.e. in the barycenter of the bar. For comparison, we also show the results obtained with a third-order ALE ADER-WENO scheme (black line), with which our numerical solution (blue line) is in good agreement. In Fig. 8, the first component of the stress tensor $\sigma_{1,11}$ and the vertical component of the velocity $v_{1,2}$ are shown on the left and right panels respectively for the intermediate times $t = 8$, $t = 15$, $t = 23$ and $t = 30$, covering approximately one bending period. Despite the fact that in our case we use a diffuse interface approach on a fixed Cartesian grid, our computational results compare visually well with the reference solutions available in the literature, e.g. [112, 75, 17, 13, 92], which all have been simulated with a pure Lagrangian or arbitrary Lagrangian-Eulerian scheme on moving meshes.

7.7 Taylor bar impact

In the previous test, we considered an ideal elastic material, which is the limit case for $\tau_1 \to \infty$. In the following test, we show how a material can also exhibit non-linear elastic-plastic behaviour.

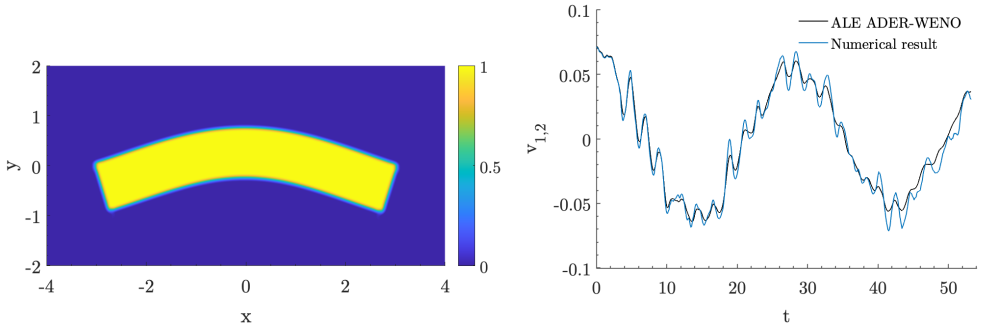

Fig. 7: Filled contour map of the volume fraction function α_1 for the first phase, which represents the geometry of the beryllium bar at time $t = 8$ (left). The time evolution of the vertical velocity component $v_{1,2}(0,0,t)$ at $\bar{\mathbf{x}} = (0,0)$, i.e. in the barycenter of the bar (right).

Here we consider the Taylor bar impact problem, which is a classical benchmark for an elasto-plastic target that impacts on a rigid solid wall, e.g. see [112, 75, 34, 13] for pure Lagrangian or ALE schemes on moving meshes and [18] for an Eulerian diffuse interface approach.

As in the previous test, we define two separate density fields representing a gas and a solid phase through their respective volume fractions. The computational domain considered here is larger than in the Lagrangian setup in order to include the space occupied by the gas phase around the solid. The computational domain under consideration, as in [18], is $\Omega = [-150, +150] \times [0, 600]$ and the initial conditions for the solid phase are

$$\alpha_1(x,y) = \begin{cases} 1-2\epsilon & \text{if } \boldsymbol{x} \in \Omega_1, \\ \epsilon & \text{if } \boldsymbol{x} \notin \Omega_1, \end{cases} \quad \boldsymbol{v}_1(x,y) = \begin{cases} (0, \boldsymbol{v}_{1,2}) & \text{if } \boldsymbol{x} \in \Omega_1, \\ (0,0) & \text{if } \boldsymbol{x} \notin \Omega_1, \end{cases} \tag{150}$$
$$\rho_1 = 2.785, \quad p_1 = 10^{-4}, \quad \boldsymbol{A}_1 = \boldsymbol{I},$$

where $\Omega_1 = [-50, +50] \times [0, 500]$ is the subdomain that defines the initial geometry of the solid bar, and the initial vertical velocity component is $\boldsymbol{v}_{1,2} = -0.015$; while the gas phase is initialised as follows

$$\alpha_2(x,y) = \begin{cases} \epsilon & \text{if } \boldsymbol{x} \in \Omega_1, \\ 1-2\epsilon & \text{if } \boldsymbol{x} \notin \Omega_1, \end{cases} \tag{151}$$
$$\rho_2 = 10^{-3}, \quad \boldsymbol{v}_2 = \boldsymbol{0} \quad P_2 = 10^{-4}, \quad \boldsymbol{A}_2 = \boldsymbol{I}.$$

According to [112, 75, 34, 13], the solid projectile is assumed to be an aluminium bar, with following material parameters $\gamma_1 = 1.4$, $\mathrm{Cv}_1 = 1000$, $\mathrm{Cs}_1 = 0.305$, $\rho \mathrm{o}_a = 2.785$, $\mathrm{Co}_1 = 0.533$ and $p\mathrm{o}_1 = p_1$. To obtain a non-linear elasto-plastic material behaviour the relaxation time τ_1^{e} has to be choosen as a non-linear function of an invariant of the shear stress tensor as follows [6, 92]

$$\tau_1^{\mathrm{e}} = \tau_{\mathrm{o}} \left(\frac{\sigma_{\mathrm{o}}}{\bar{\sigma}_1} \right)^m, \tag{152}$$

where $\tau_{\mathrm{o}} = 1$ is the scaling constant, $\sigma_{\mathrm{o}} = 0.003$ is the yield stress of the material under quasi static conditions, the exponent parameter is chosen equal to $m = 20$ (the higher m is the less rate-dependent the effective yield strength is [6, 92]) and the von Mises stress $\bar{\sigma}_1$ is given by

$$\bar{\sigma}_1 = \left(\frac{1}{2} \big((\sigma_{1,11} - \sigma_{1,22})^2 + (\sigma_{1,22} - \sigma_{1,33})^2 + (\sigma_{1,33} - \sigma_{1,11})^2 + 6(\sigma_{1,21}^2 + \sigma_{1,31}^2 + \sigma_{1,32}^2) \big) \right)^{1/2}. \tag{153}$$

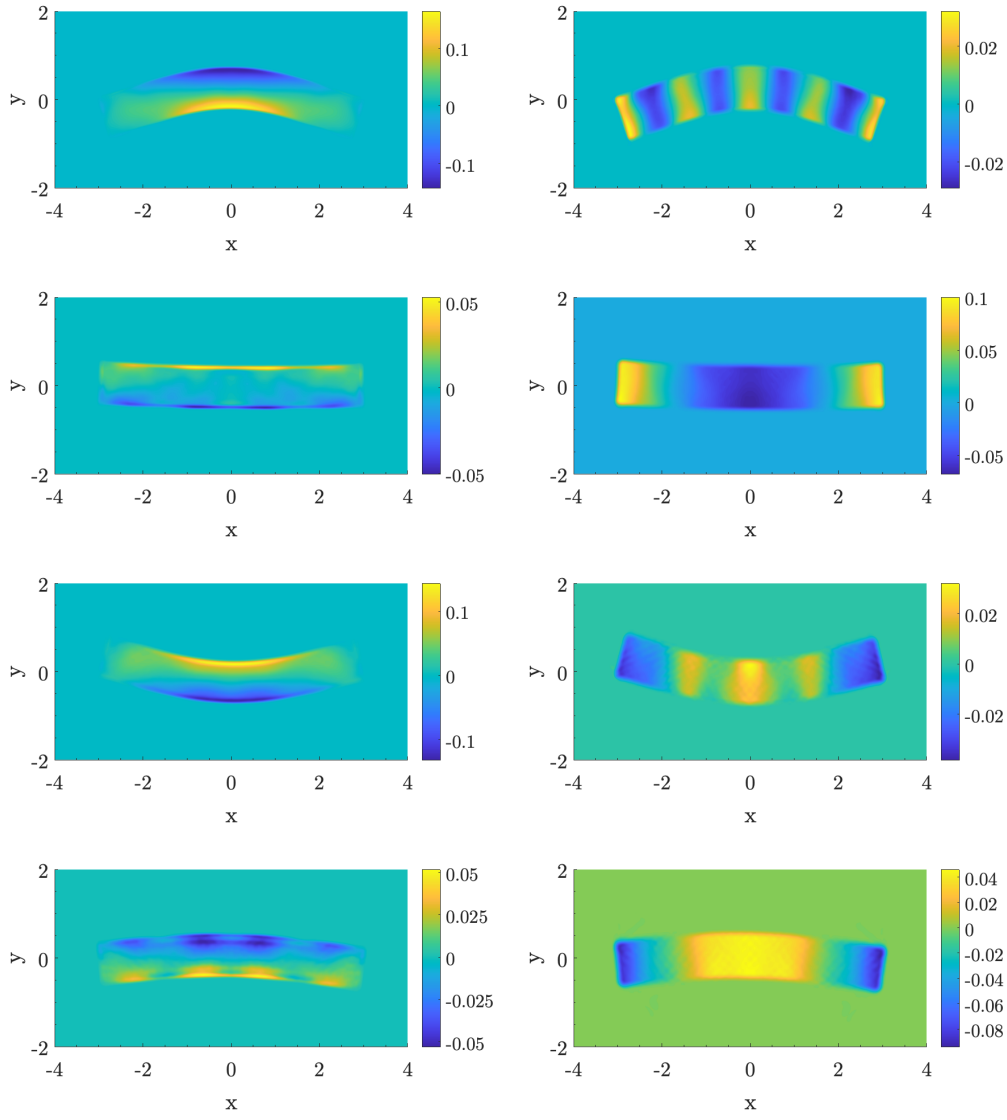

Fig. 8: Results for the elastic vibrations of a beryllium plate, at times $t = 8$, $t = 15$, $t = 23$ and $t = 30$ (from top to bottom), for the first component of the stress tensor $\sigma_{1,11}$ and the vertical component of the velocity $v_{1,2}$.

For the surrounding gas phase, the ideal gas EOS with the parameters $\gamma_2 = 1.2$, $\mathrm{Cv}_2 = 1000$, $\mathrm{Cs}_2 = 1.0$ and $\nu_2 = 10^{-4}$ is used.

The simulation is carried out up to the final time $t_f = 5000$, and the computational domain is discretized with a uniform Cartesian mesh composed of 2048×1024 control volumes. In contrast to the Lagrangian schemes, it is not necessary to impose boundary conditions on the surface of the solid; in our simulation, periodic boundaries are set in the x-direction while reflective slip wall boundary conditions are set in the y-direction.

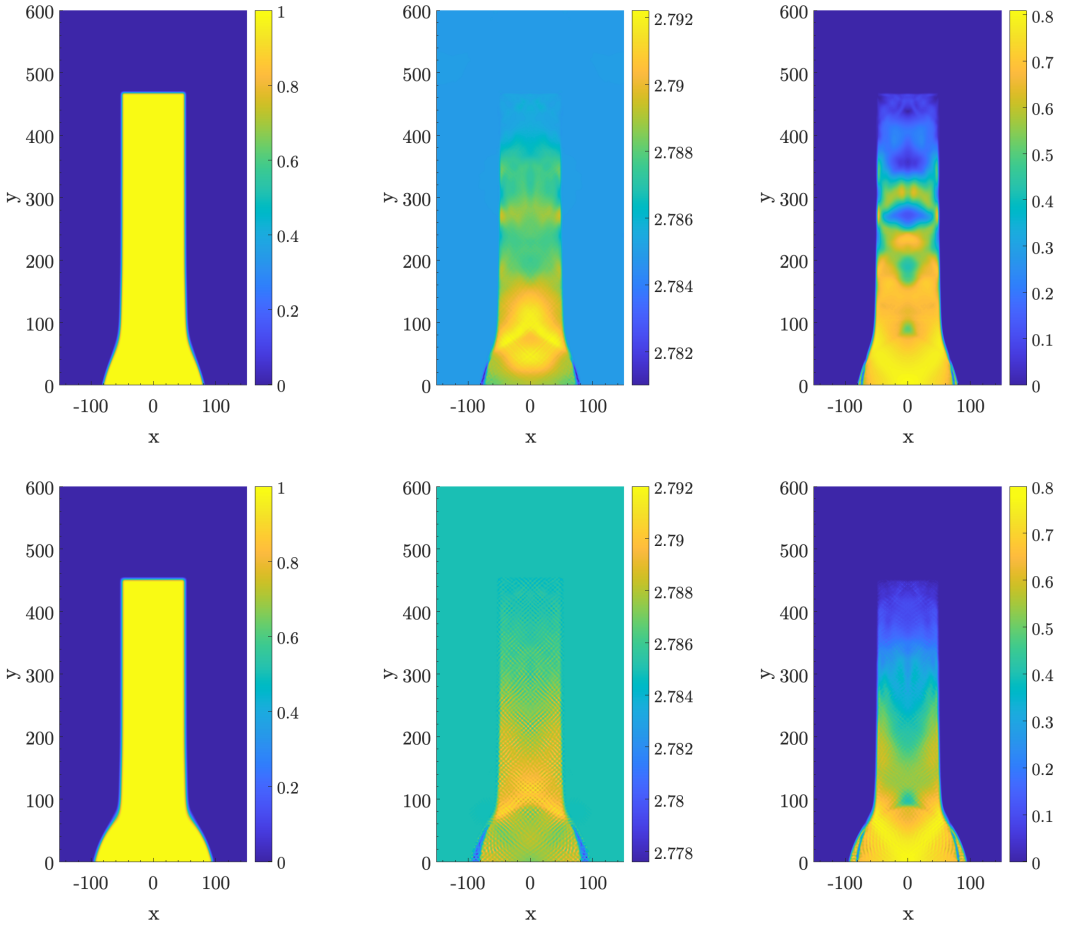

Fig. 9: Results for the non-linear elasto-plastic Taylor bar impact, at times $t = 2500$ and $t = 5000$ (from top to bottom): the volume fraction (left), the density distribution (center) and the plastic rate $\eta_1 = \bar{\sigma}_1/\sigma_o$ (right).

In Fig. 9, we present the results computed at output times $t = 2500$ and $t = 5000$. The volume fraction (left), the density distribution (center) and the plastic rate $\eta_1 = \bar{\sigma}_1/\sigma_o$ (right) are depicted. It can be observed that the numerical solution is in good agreement with that presented in [75, 13], although the models used are significantly different. Moreover at time $t = 5000$, the final length of the aluminium bar is $L_f = 455$, which fits the results achieved in [75, 13] within the 2% error.

7.8 Multiphase Rayleigh-Taylor instability

The two previous tests focused mainly on the validation of the unified model for the elastic and elasto-plastic type behavior, and not much emphasis was placed on the dynamics of the fluid phase. In this test, however, we will finally put to the test one of the main features of the model and the numerical scheme, namely the ability to describe several interacting phases. To this end, we will simulate a true *two-phase* low-Mach, $M_1 \simeq M_2 \simeq 0.1$, viscous Rayleigh–Taylor instability. The approach follows [25], but with the notable modification that instead of initialising a single fluid with a jump in the density, we define two fluids through the volume fraction and each fluid has a constant phase density. This makes the problem more challenging because the quasi-vacuum states of either phase are introduced almost throughout the entire computational domain, however it introduces much more freedom in defining the material characteristics of each phase. The computational domain under consideration, as in [25], is $\Omega = [0, 1/3] \times [0, 1]$ and the initial conditions for the hevier phase (on top) are

$$\begin{aligned} &\alpha_1(x, y) = \bar{s}(1 - 2\epsilon) + (1 - \bar{s})\epsilon, \qquad \rho_1 = 2.0, \qquad \boldsymbol{v}_1 = \boldsymbol{0}, \\ &p_1 = \bar{s}p_t + (1 - \bar{s})p_b, \qquad \boldsymbol{A}_1 = \boldsymbol{I}, \end{aligned} \tag{154}$$

and for the lighter fluid (at the bottom) are

$$\begin{aligned} &\alpha_2(x, y) = 1 - \alpha_1 - \epsilon, \qquad \rho_2 = 1.0, \qquad \boldsymbol{v}_2 = \boldsymbol{0}, \\ &p_2 = \bar{s}p_t + (1 - \bar{s})p_b, \qquad \boldsymbol{A}_2 = \boldsymbol{I}, \end{aligned} \tag{155}$$

where $\bar{s}$ is a switch function introduced to impose a smooth transition between the two states and to avoid inaccurate representation of the initial condition on the discrete Cartesian grid. This function $\bar{s}$ is defined as

$$\bar{s} = \frac{1}{2} + \frac{1}{2}\mathrm{erf}\left(\frac{y - y_{\mathrm{I}}}{\delta}\right), \tag{156}$$

where $y_{\mathrm{I}} = 0.5 + 0.01\cos(6\pi x)$ is the initially perturbed interface between phases and $\delta = \max(0.004, 6\Delta x)$ can be seen as the thickness of this interface. The initial top and bottom phase pressures, in (154), (155), are defined as

$$\begin{aligned} p_t &= 1 + \rho_1(1 - y)\boldsymbol{g}, \\ p_b &= 1 + 0.5\rho_1\boldsymbol{g} + \rho_2(0.5 - y)\boldsymbol{g}, \end{aligned} \tag{157}$$

where the gravity vector is $\boldsymbol{g} = (0, -0.1, 0)^T$. The other parameters and physical quantities are equal for the two gas phases and using the ideal-gas EOS are set as $\gamma = 1.4$, Cv $= 1000$, Cs $= 0.3$ and the dynamic viscosity $\mu = 6 \times 10^{-5}$, which translates to $\tau_1^{\mathrm{e}} = 2 \times 10^{-3}$ and $\tau_2^{\mathrm{e}} = 4 \times 10^{-3}$ so that the Reynolds number of the test problem is $\mathbb{R}\mathrm{e} \simeq 2000$ for the both phases.

Two simulations are carried out up to the final time $t_f = 10$ on two different uniform Cartesian meshes in order to verify mesh convergence of the solution algorithm. In these simulations, periodic boundaries are set in x-direction while reflective slip wall boundary conditions are set in y-direction. Fig. 10 shows on the left the result for the mixture density $\rho = \alpha_1\rho_1 + \alpha_2\rho_2 + \alpha_3\rho_3$ obtained with a mesh consisting of 512×1536, while on the right the result obtained by doubling the mesh resolution, both at time $t = 7$. It is possible to see that mesh convergence has already been achieved with the coarsest mesh, since the macroscopic structure of the flow does not depend on mesh size.

Fig. 11 shows the time evolution of both the volume fraction function α_1 and the $A_{1,12}$ component of the distortion field, for the first phase. It is interesting to note that it for such a low Mach

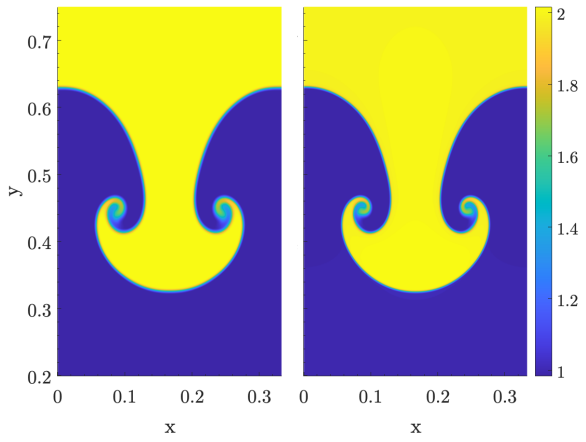

Fig. 10: Mixture density ρ. Mesh convergence test for the Rayleigh-Taylor instability problem, at times $t = 7$; on the left the result obtained with a mesh consisting of 512×1536 is shown, and on the right the result obtained by doubling the mesh resolution.

number as in this test, the mixture density, depicted in Fig. 10 is macroscopically proportional to the volume fraction structure in Fig. 11. Moreover, due to the velocity relaxation, both distortion fields encode the same flow structure, except that they satisfy two different algebraic constraints, so that each phase mass conservation equation is the consequence of the time evolution of each phase distortion field, see 6.4.1.

Our computational results, in particular the temporal evolution in Fig. 11 compare visually well with the reference solutions available in the literature, see [71], obtained in this case with ALE schemes on moving meshes.

7.9 Three-phase triple point problem

Finally, in this section, we will test all the capabilities of the model and the numerical scheme developed, i.e. the ability to describe several, up to three in this paper, interacting phases. The problem that will be addressed is a typical test in the ALE community, namely the so-called triple point problem. This test is a three state, two material, 2D Riemann problem in a rectangular domain that generates vorticity, which is why it is very popular in the ALE community for testing the ability of a code to handle complex fluid motion on moving mesh. It was introduced in [72] and was used to compare ALE approaches in the case of a two-material Riemann problem in [71, 16, 69] or the simplified one-material case in [14, 10, 46]. In the Eluerian context, this problem has been addressed with an interface-capturing approach considering three immiscible compressible fluids in [132]. In the context of this work, the main aim of this problem is to verify the ability of the code and model to correctly propagate shock waves over multiphase and multi-material regions.

Specifically, we follow the setting presented in [72], but with the significant modification that instead of initialising a two-material Riemann problem, we set up an initial problem involving three phases, where two of them have the same material parameters. The computational domain of the triple point problem $\Omega = [0; 7] \times [0; 3]$ is divided into three subdomains filled with three phases describing different perfect gases, thus yielding a three-phase, two-material problem. The initial condition, in our diffuse interface framework, can be easily set by means of jumps in volume

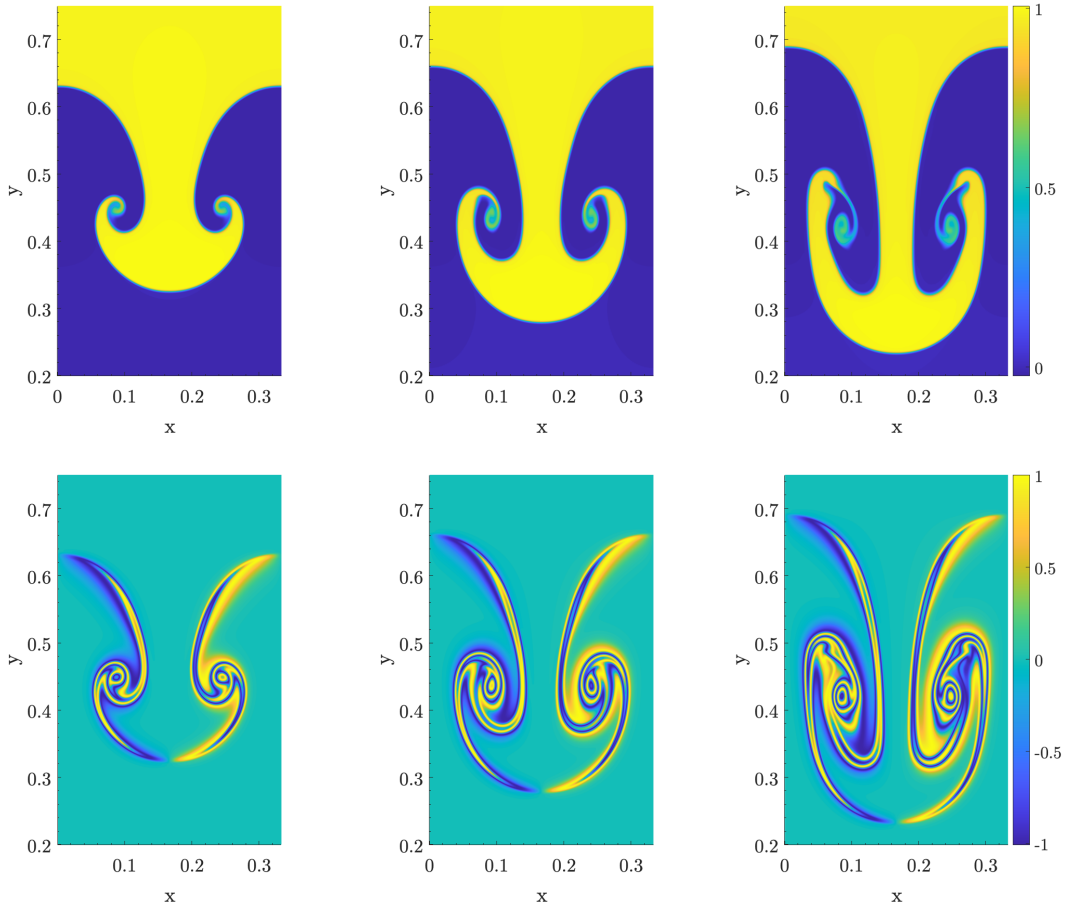

Fig. 11: Results for the multiphase Rayleigh-Taylor instability problem, at times $t = 6$, $t = 7$ and $t = 8$ (from left to right); the volume fraction α_1 (top) and the $A_{1,12}$ component of the distortion field for the first phase (bottom) are represented.

fraction as follows. The first phase, with a state of high pressure and high density, is initialized as

$$\begin{aligned} \alpha_1(x,y) &= \begin{cases} 1-2\epsilon & \text{if } \boldsymbol{x} \in \Omega_1, \\ \epsilon & \text{if } \boldsymbol{x} \notin \Omega_1, \end{cases} \qquad \text{with} \qquad \Omega_1 = [0;1] \times [0;3] \\ \rho_1 &= 1.0, \quad \boldsymbol{v}_1 = \boldsymbol{0}, \quad p_1 = 1.0, \quad \boldsymbol{A}_1 = \boldsymbol{I}, \end{aligned} \tag{158}$$

the second phase, with a state of low pressure high density, as

$$\begin{aligned} \alpha_2(x,y) &= \begin{cases} 1-2\epsilon & \text{if } \boldsymbol{x} \in \Omega_2, \\ \epsilon & \text{if } \boldsymbol{x} \notin \Omega_2, \end{cases} \qquad \text{with} \qquad \Omega_2 = [1;7] \times [0;1.5] \\ \rho_2 &= 1.0, \quad \boldsymbol{v}_2 = \boldsymbol{0}, \quad p_2 = 0.1, \quad \boldsymbol{A}_2 = \boldsymbol{I}, \end{aligned} \tag{159}$$

and the third, with an initial low pressure and low density state, is initialized as

$$\begin{aligned} \alpha_3(x,y) &= \begin{cases} 1-2\epsilon & \text{if } \boldsymbol{x} \in \Omega_3, \\ \epsilon & \text{if } \boldsymbol{x} \notin \Omega_3, \end{cases} \qquad \text{with} \qquad \Omega_3 = [1;7] \times [1.5;3.0] \\ \rho_3 &= 0.125, \quad \boldsymbol{v}_3 = \boldsymbol{0}, \quad p_3 = 0.1, \quad \boldsymbol{A}_3 = \boldsymbol{I}. \end{aligned} \tag{160}$$

All the phases represent ideal inviscid gases, thus we are in the stiff limit of the model and the relaxation times are $\tau_1^e = \tau_2^e = \tau_3^e = 14^{-14}$. Furthermore, according to [72], since the first phase and the third phase represent the same material with the material parameters $\gamma_1 = \gamma_3 = 1.5$, $\text{Cv}_1 = \text{Cv}_3 = 1$, $\text{Cs}_1 = \text{Cs}_3 = 1.0$, while the second phase has the paramers $\gamma_2 = 1.4$, $\text{Cv}_2 = 1$, $\text{Cs}_2 = 1.0$.

The simulation is carried out up to the final time $t_f = 5$ discretizing the computational domain with a uniform Cartesian mesh composed of 3584×1536 control volumes; reflective slip wall boundary conditions are set in all the directions.

In Fig. 12 and 13, we present the results obtained for the multiphase and multi-material triple point problem at time $t = 3$ and $t = 5$, respectively. In particular, we illustrate the evolution of the different volume fractions (top), where the first phase is shown in blue, the second in yellow and the third in blue-green. These contour levels clearly show that the vortex shape is well resolved and a zoom is shown on the right to better visualise the vorticity formation resulting from the initial contact discontinuity. From these results, it is clear how suitable a modelling and numerical description via an Eulerian diffuse interface approach is for describing these mixing areas characterised by high vorticity.

From the representation of the density field in Fig. 12 and 13, the entire dynamics of the problem can be well understood. The fluid flow after the initial discontinuity has broken is characterised by a rarefaction wave pointing to the left and two shock waves pointing to the right, separated by a horizontal contact discontinuity. Moreover, these two shock waves has different velocities, as the densities of the materials are different, and this leads to the formation of a strong vortex. Our computational results compare visually well with reference solutions available in the literature [72, 71, 46], proving the ability of the code and model to correctly propagate shock waves over multiphase and multi-material regions, despite the results being obtained on a simple fixed Cartesian grid.

Additionally, in Fig. 12 and 13, we present the evolution of the $A_{1,12}$ component of the first phase distortion field. However, as emphasised in the previous test case, the distortion fields of all phases encode the same flow structure, except that they satisfy three different algebraic constraints (134), thus the representation in Fig. 12 and 13 is indicative of the flow structure of all phases. We note once again an extremely useful ability of the distortion field (encoded in its rotational component $\boldsymbol{R}_1$) to demonstrate the details of the flow structures hidne otherwise. Thus, thanks

to this ability of the distortion field, it is possible to identify a strong shear zone along a contact discontinuity inside the second phase (the yellow one) that otherwise would not have been visible using the other state variables.

7.10 Water entry of a symmetric wedge

In all the previous test cases all three phases were formally considered, but some of them had identical material parameters. In this sense, the test addressed in this section is more general, and all three phases will be considered having very different material parameters. Namely, we consider one solid, one liquid and one gaseous phase. The aim of this numerical test is to reproduce, as fully as possible, the experiment conducted by Zhao et al. [133], which consists of the impact of a symmetrical wedge with a free surface. This test has already been considered in the validation

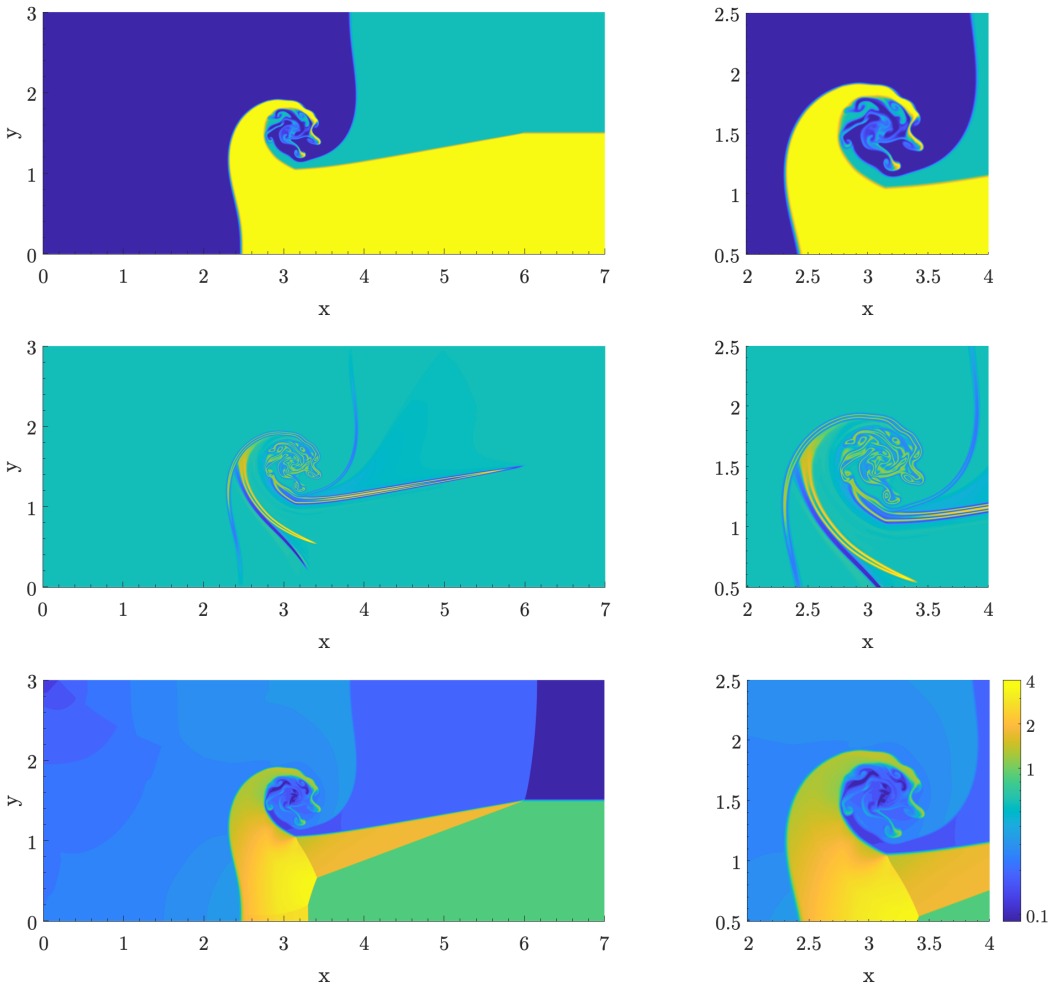

Fig. 12: Results for the multiphase and multi-material triple point problem at time $t = 3$: the contour plots of the volume fractions (first phase in blue, second phase in yellow and the third one in blue-green) (top), the $A_{1,12}$ component of the distortion field for the first phase (center) and the mixture density (bottom). A zoom in the region $[2.0, 4.0] \times [0.5, 2.5]$, which illustrates the formation of vorticity resulting from the initial contact discontinuity, is shown (right).

of the semi-implicit numerical scheme presented by the authors in [44]. Unlike the previous work, using the explicit FV scheme developed in this paper for the compressible multiphase fluid and solid mechanics, we have a possibility to reproduce the experimental setup [133] in its completeness. Namely, by imposing only the initial velocity of the solid wedge, we can now evaluate the complete dynamics of the three phases resulting from their interaction. Therefore, the vertical velocity of the wedge recorded experimentally by Zhao et al. [133] and reported in Fig. 14, which was *prescribed* in the previous work [44] and in the numerical test by Oger et al. [86], now becomes an excellent indicator to judge about the validity of the multiphase simulation presented here.

In this numerical experiment, we follow the geometric setup used in our previous work [44] but with the significant modification of defining an initial problem involving three phases. The computational domain $\Omega = [-0.5; 0.5] \times [-0.5; 0.5]$ is divided into three subdomains occupied with

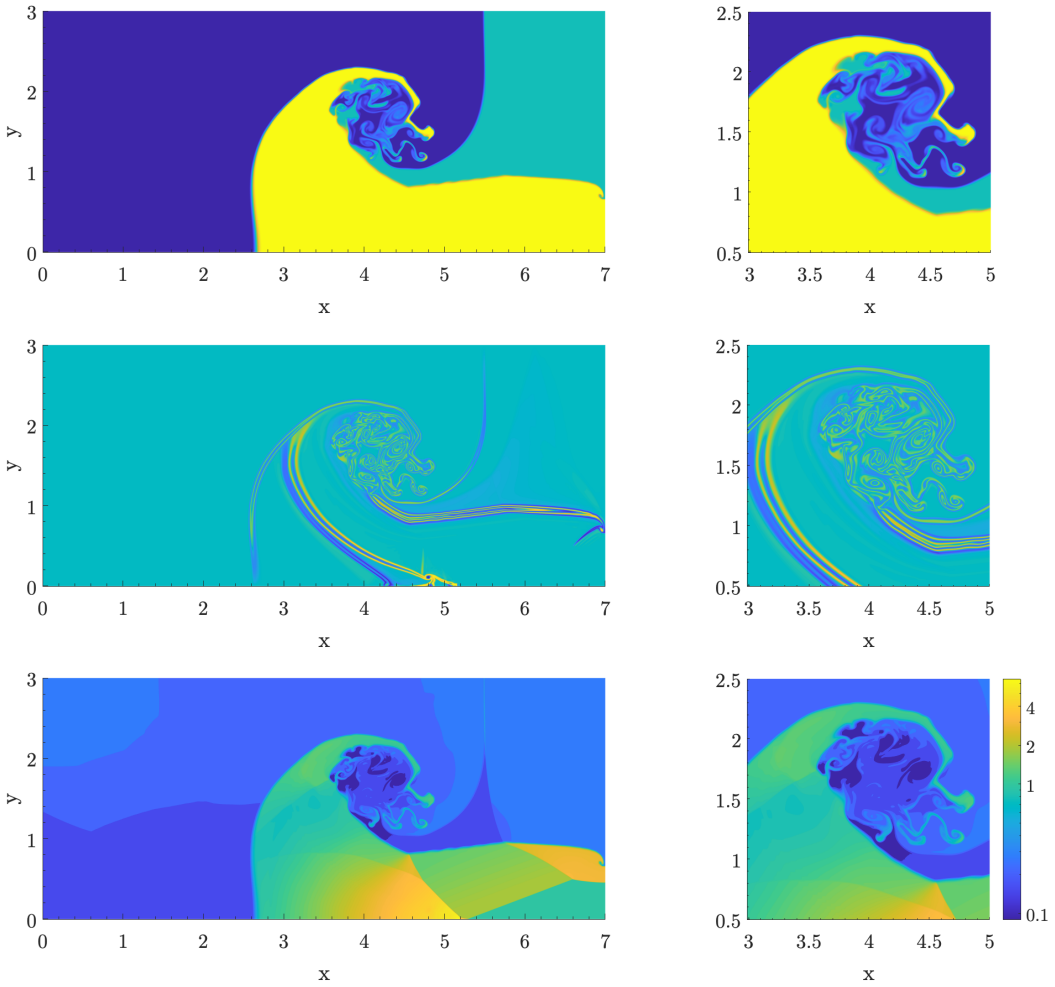

Fig. 13: Results for the multiphase and multi-material triple point problem at time $t = 5$: the contour levels of the volume fractions (first phase in blue, second phase in yellow and the third one in blue-green) (top), the $A_{1,12}$ component of the distortion field for the first phase (center) and the mixture density (bottom). A zoom in the region $[3.0, 5.0] \times [0.5, 2.5]$, which illustrates the formation of vorticity resulting from the initial contact discontinuity, is shown (right).

three phases describing an ideal elastic solid, a viscous liquid phase and a viscous gaseous phase. The initial condition for each phases are set by means of jumps in volume fraction. The first phase, the solid one, is defined according to the the geometry of the experimental section, which consider the wedge with a dead-rise angle of 30° illustrated in Fig. 14 (left); specifically the initial conditions for this phase read

$$\begin{aligned}
&\alpha_1(x,y) = \begin{cases} 1-2\epsilon & \text{if } \ |x| \leq 0.25 \ \wedge \ y \geq |x\tan(\frac{\pi}{6})| \ \wedge \ y \leq 0.25\tan(\frac{\pi}{6}), \\ \epsilon & \text{if otherwise}, \end{cases} \\
&\rho_1 = 7{\times}10^3, \quad \boldsymbol{v}_1 = (0,-6.15), \quad p_1 = 10^3, \quad \boldsymbol{A}_1 = \boldsymbol{I},
\end{aligned} \tag{161}$$

where the density is evaluated to obtain the total weight of the measuring section used in the experiment by Zhao et al. [133], which corresponds to 255.5 kg; thus the density is calculated as the weight of the instrumental tools divided by the effective area described by the wedge in this numerical setup. The initial condition for the second phase, defining the viscous liquid phase, are

$$\begin{aligned}
&\alpha_2(x,y) = \begin{cases} 1-2\epsilon & \text{if } \ \boldsymbol{x} \in \Omega_2, \\ \epsilon & \text{if } \ \boldsymbol{x} \notin \Omega_2, \end{cases} \quad \text{with} \quad \Omega_2 = [-0.5;0.5]{\times}[-0.5;0.0] \\
&\rho_2 = 10^3, \quad \boldsymbol{v}_2 = \boldsymbol{0}, \quad p_2 = 10^3, \quad \boldsymbol{A}_2 = \boldsymbol{I},
\end{aligned} \tag{162}$$

while the third one, defining the gaseous phase, is initialized as

$$\alpha_3 = 1-\alpha_1-\alpha_2, \quad \rho_3 = 1, \quad \boldsymbol{v}_3 = \boldsymbol{0}, \quad p_3 = 10^3, \quad \boldsymbol{A}_3 = \boldsymbol{I}. \tag{163}$$

For the solid and liquid phase, the stiffened gas EOS is used; the other material parameters are $\gamma_1 = \gamma_2 = 1.4$, $\mathrm{Cv}_1 = \mathrm{Cv}_2 = 1$, $\mathrm{Cs}_1 = 120$, $\mathrm{Cs}_2 = 100$, $\mathrm{Co}_1 = \mathrm{Co}_2 = 120$ and $p\mathrm{o}_1 = p\mathrm{o}_2 = p_1$. For the viscous gas, the ideal gas EOS is used with the following parameters $\gamma_3 = 1.4$, $\mathrm{Cv}_3 = 1$, $\mathrm{Cs}_3 = 60.0$ and $\nu_3 = 10^{-1}$. To consider an ideal elastic material, the relaxation time for the first phase is chosen to be $\tau_1^{\mathrm{e}} = 10^{14}$, while a kinematic viscosity $\nu_1 = 10^{-6}$ is adopted for the viscous liquid phase.

Two simulations are carried out up to the final time $t_f = 0.025$ on two different uniform Cartesian meshes composed of 1024×1024 and 2048×2048 control volumes, in order to verify qualitatively the mesh convergence of the solution. In these simulations, reflective slip wall boundary conditions are set in all the directions.

Fig. 14 (left) shows the distribution of the different volume fractions in accordance with the initial conditions describing the geometric and experimental setup of the test water entry of a symmetric wedge. The solid phase is shown in yellow, the liquid phase in blue-green and the gas phase in blue. Moreover, in Fig. 14 (right) we present a comparison that verifies the validity of the results obtained. In this comparison, the vertical velocity of the wedge experimentally recorded by Zhao et al. [133] is compared with the purely elastic solid body velocity computed in this test by evaluating an averaged vertical velocity using the volume fraction, in accordance with the following definition

$$|\boldsymbol{v}_{1,2}| = \frac{|\sum_{ij}^{N_1 N_2} \alpha_{1,ij} v_{1,2}|}{\sum_{ij}^{N_1 N_2} \alpha_{ij}}, \tag{164}$$

where N_1 and N_2 are the discrete elements in the first and in the second directions, respectively. It is possible to observe how qualitatively the dynamics of the impact is well represented, in particular the deceleration over time follows the correct trend, i.e. deceleration increases in modulus until about half the simulation time and then tends to decrease. Furthermore, both the results obtained with a 1024×1024 mesh and that obtained by doubling the mesh resolution are represented, and

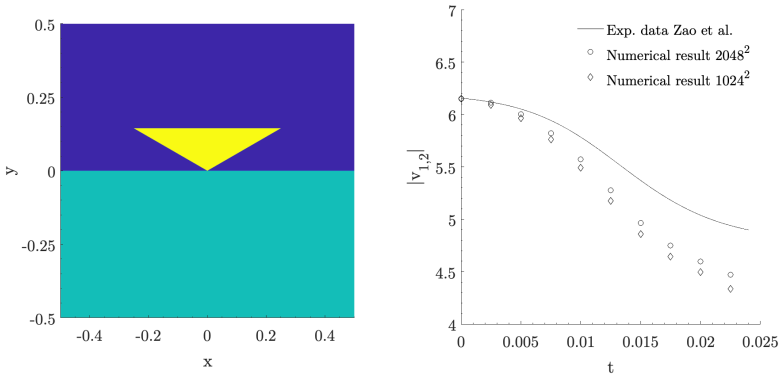

Fig. 14: Filled contour map of the different volume fractions of the constituents to represent the initial test condition (left). Comparison with the reference vertical wedge fall velocity experimentally recorded by Zhao et al. [133] of the average components of the vertical velocity of the solid wedge $v_{1,2}$ evaluated with the explicit FV scheme for the complete compressible multiphase fluid and solid mechanics on two different uniform Cartesian meshes (right).

it can be seen that the numerical solution is getting closer to that recorded experimentally by Zhao et al. [133] as mesh is getting more finer. The main reason for the discrepancy from the experimental result has to be found in the strongly low Mach nature of the test. Indeed, this impact, in which the solid must maintain a particularly rigid behaviour, represents a complex test for an explicit numerical scheme. Moover, it should be noted that this is the first time this test has been solved by considering the interaction of three phases through a monolithic mathematical model for compressible multiphase fluid and solid mechanics.

Fig. 15 shows the temporal evolution of volume fractions obtained with the explicit FV scheme for compressible multiphase fluid and solid mechanics (right column). For the sake of comparison, the results previously obtained in [44] with a semi-implicit numerical method are shown along side with the new results, see the left column. From the top to the bottom, the results for three different instants are shown: $t = 0.005$, $t = 0.015$ and $t = 0.020$. It can be observed that the phenomenological evolution of the free surface during the entry of the wedge, obtained with the new numerical method that solves the entire three-phase dynamics, is in agreement with what was previously obtained in [44] with a semi-implicit solver. The first time instant shows quite well the formation of two jets escaping along the edges of the wedge. At time $t = 0.015$, these two jets reach the point of separation, which corresponds to the end of the edge. It can be seen that the jets leave the edge almost tangentially at this initial phase of flow separation. Then, at $t = 0.020$, the jets tend to move more vertically as well as breaking. This shape is qualitatively similar to the experimental illustration in the article by Zhao et al. [133].

Furthermore, Fig. 15 shows the velocity fields obtained with both numerical methods. One can see that the gas phase was not considered in [44] presented in the left column, while the dynamics of all three phases is taken into account in this paper. The interraction of the liquid jets and the gas phase might in particular be responsible for the slight differences in jets shape between the two simulations.

7.11 Multiphase and multi-material solid impact

This is the last test presented in this work, the aim of which is to show from a qualitative point of view the wide applicability of the model and numerical scheme presented. As in the previous test, all the capabilities of the developed model and numerical scheme are tested. Namely, an impact

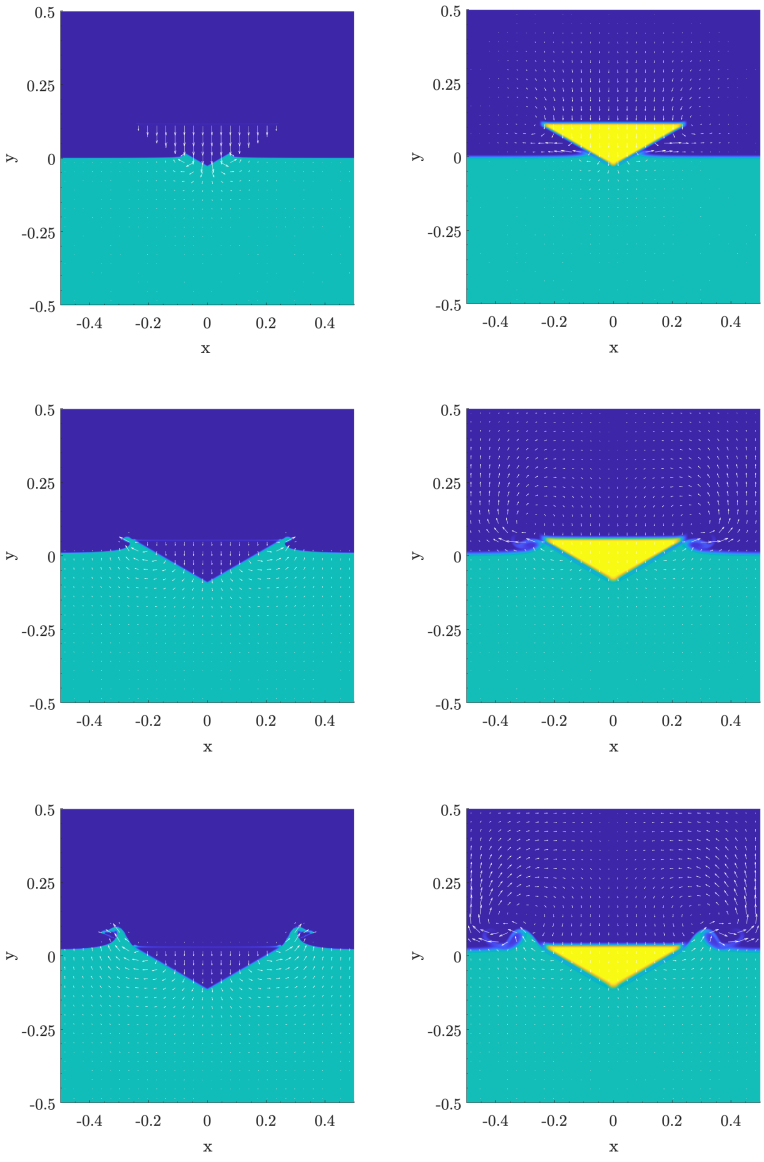

Fig. 15: Filled contour map of the different volume fractions of the constituents and velocity field of the mixture, the solid phase is shown in yellow, the liquid phase in blue-green and the gas phase in blue. Results obtained with the explicit FV scheme for compressible three-phase fluid and solid mechanics (right), and the two-phase results obtained with a semi-implicit numerical method from [44] (left). From the top to the bottom, three different time instants are shown: $t = 0.005$, $t = 0.015$ and $t = 0.020$.

of true multi-material *three-phases* will be simulated, which exhibits elastic and also elasto-plastic behaviour in a inviscid fluid environment.

In this test, we roughly follow the approach presented in [31, 15], which has been modified by not paying particular attention to physical material characteristics, as the interest is to qualitatively verify the approach ability to solve such a complex test. Thus, while maintaining the geometry similar to the tests in the literature, the parameters and physical quantities that define the properties of the aluminium bar in 7.7 are used. Therefore, this test case presents an impact of an aluminium ball into an aluminium plate embedded in the surrounding inviscid fluid modeld with the perfect gas EOS. The computational domain $\Omega = [-0.5; 0.5] \times [-0.5; 0.5]$ is divided into three subdomains filled with three phases describing two solids with the same properties and a perfect gas. As for the previous test, the initial conditions are set by means of jumps in volume fraction; the first phase, that defines the aluminium ball, is initialized as

$$\begin{aligned} &\alpha_1(x,y) = \begin{cases} 1-2\epsilon & \text{if } ((-0.125-x)^2 + (0.5-y)^2)^{0.5} \leq 0.075, \\ \epsilon & \text{if otherwise,} \end{cases} \\ &\rho_1 = 2.785, \quad \boldsymbol{v}_1 = (0.002, 0), \quad p_1 = 10^{-6}, \quad \boldsymbol{A}_1 = \boldsymbol{I}, \end{aligned} \tag{165}$$

the second phase, defining the aluminium plate, as

$$\begin{aligned} &\alpha_2(x,y) = \begin{cases} 1-2\epsilon & \text{if } \boldsymbol{x} \in \Omega_2, \\ \epsilon & \text{if } \boldsymbol{x} \notin \Omega_2, \end{cases} \quad \text{with} \quad \Omega_2 = [0.05; 0.225] \times [-0.35; 0.35] \\ &\rho_2 = 2.785, \quad \boldsymbol{v}_2 = \boldsymbol{0}, \quad p_2 = 10^{-6}, \quad \boldsymbol{A}_2 = \boldsymbol{I}, \end{aligned} \tag{166}$$

and the third, defining the surrounding perfect gas, is initialised as

$$\alpha_3 = 1 - \alpha_1 - \alpha_2, \quad \rho_3 = 10^{-3}, \quad \boldsymbol{v}_3 = \boldsymbol{0}, \quad p_3 = 10^{-6}, \quad \boldsymbol{A}_3 = \boldsymbol{I}. \tag{167}$$

Since the first and second phases represent the same material, i.e. aluminium, the other parameters and physical quantities that define the properties of such a material using the stiffened gas EOS are $\gamma_1 = \gamma_2 = 1.4$, $\mathrm{Cv}_1 = \mathrm{Cv}_2 = 1000$, $\mathrm{Cs}_1 = \mathrm{Cs}_2 = 0.305$, $\mathrm{Co}_1 = \mathrm{Co}_2 = 0.533$ and $p\mathrm{o}_1 = p\mathrm{o}_2 = p_1$. For the inviscid gas phase surrounding the solid phases, the ideal gas EOS is used and the physical parameters are $\gamma_3 = 1.2$, $\mathrm{Cv}_3 = 1000$, $\mathrm{Cs}_3 = 0.0$ and $\tau_3^{\mathrm{e}} = 10^{-14}$. In a first simulation, the solid materials are assumed to have purely elastic behaviour, so the relaxation time is assumed to be $\tau_1^{\mathrm{e}} = \tau_2^{\mathrm{e}} = 10^{14}$ for both phases. Subsequently, to obtain a non-linear elasto-plastic behaviour of the material, the relaxation time $\tau_1^{\mathrm{e}}, \tau_2^{\mathrm{e}}$ is chosen as a non-linear function of an invariant of the shear stress tensor as done in the previous test, see (152). In this case, however, the yield stress of the material is set to a lower number, i.e. $\sigma_{\mathrm{o}} = 2.5 \times 10^{-4}$, for the sake of making the plastic deformations more visible.

Two simulations are carried out up to the final time $t_f = 200$ discretizing the computational domain with a uniform Cartesian mesh composed of 2048×2048 control volumes; periodic boundary conditions are set in all the directions.

Fig. 16 shows the volume fraction of the first and second phase at times $t = 60$, $t = 100$ and $t = 140$ from left to right, respectively. The first time instant represents the moment of impact with the plate. As one can see from the subsequent instants the behavior of an elastic collision is qualitatively well represented by the numerical solution. It should be emphasized that, in a diffuse interface approach, and if both the solid objects are represented by the same volume fraction function, it is not obvious that the two solids would bounce instead of sticking to each other. The results for multibody problems in which the solids are carrying their own volume fractions is, therefore, of considerable interest. Additionally, Fig. 18 shows the A_{12} component of the mixture

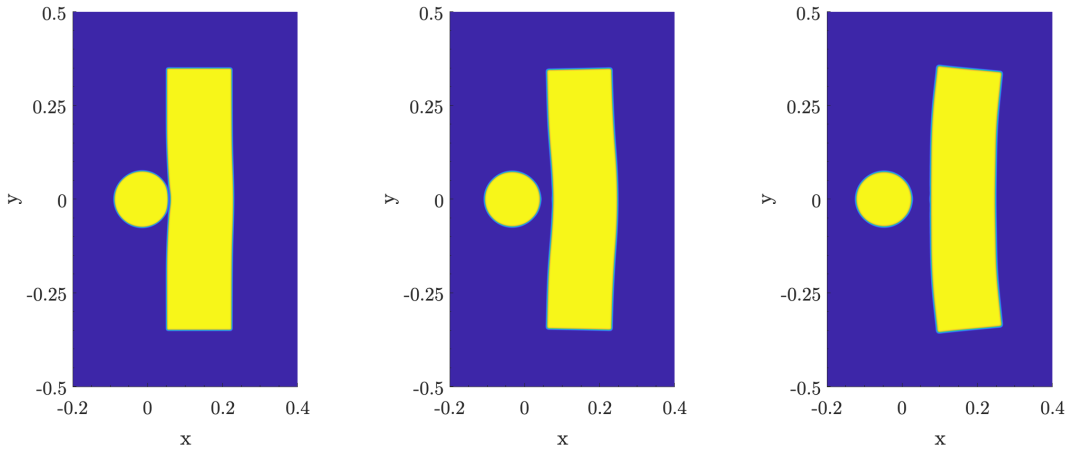

Fig. 16: Results for the multiphase and multi-material elastic solid impact. The contour levels of the volume fractions of the first and the second phases at times $t = 60$, $t = 100$, and $t = 140$ (from left to right).

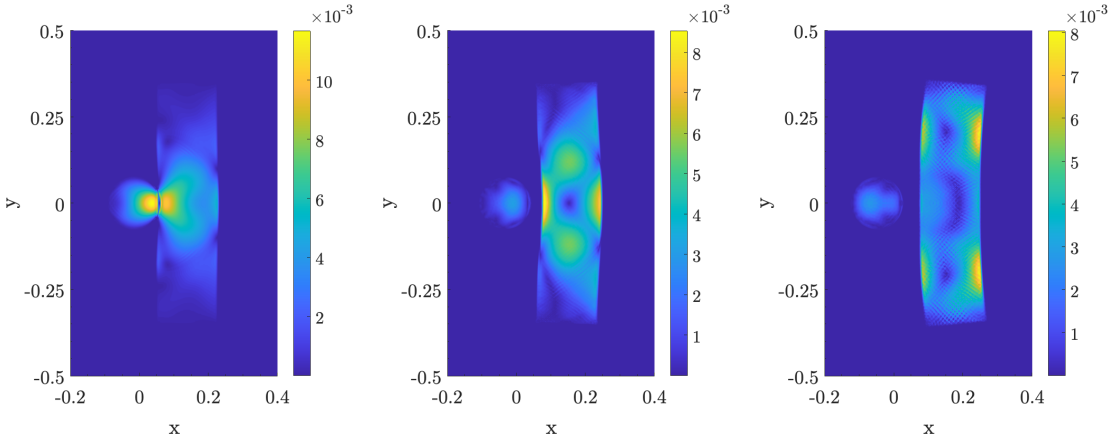

Fig. 17: Results for the multiphase and multi-material elastic solid impact. The contour levels of the von Mises stress of the first $\bar{\sigma}_1$ and the second $\bar{\sigma}_2$ at times $t = 60$, $t = 100$ and $t = 140$ (from left to right).

distortion field, obtained through the following relation

$$A_{12} = \alpha_1 A_{1,12} + \alpha_2 A_{2,12} + \alpha_3 A_{3,12}. \tag{168}$$

This allows the dynamics of the gas phase to be clearly shown as well, making it evident that the dynamics of all three phases have been resolved through a distortion field for each phase. It is possible to see the two fluid jets with non-trivial vorticity being generated at the moment of impact.

Similarly, Fig. 19 shows a collision of the same solid objects but withe plasticity effect taken into account. The obtained results visually compare well with the one in [15]. To better understand how the different definitions of material properties in these two tests affect the behavior of solids, it is useful to observe the von Mises stress of the first phase $\bar{\sigma}_1$ and the second phase $\bar{\sigma}_2$, evaluated as in (153), and presented in Fig. 17 and 20. It can be seen that the stress in an ideal elastic material

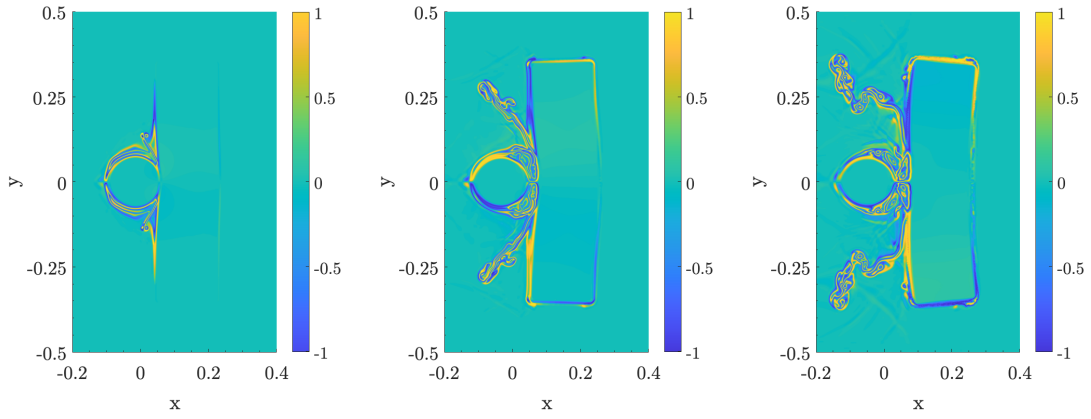

Fig. 18: Results for the multiphase and multi-material elastic solid impact. The contour levels of the A_{12} component of the mixture distortion field $\boldsymbol{A}$ are presented at times $t = 60$, $t = 100$, and $t = 140$ (from left to right).

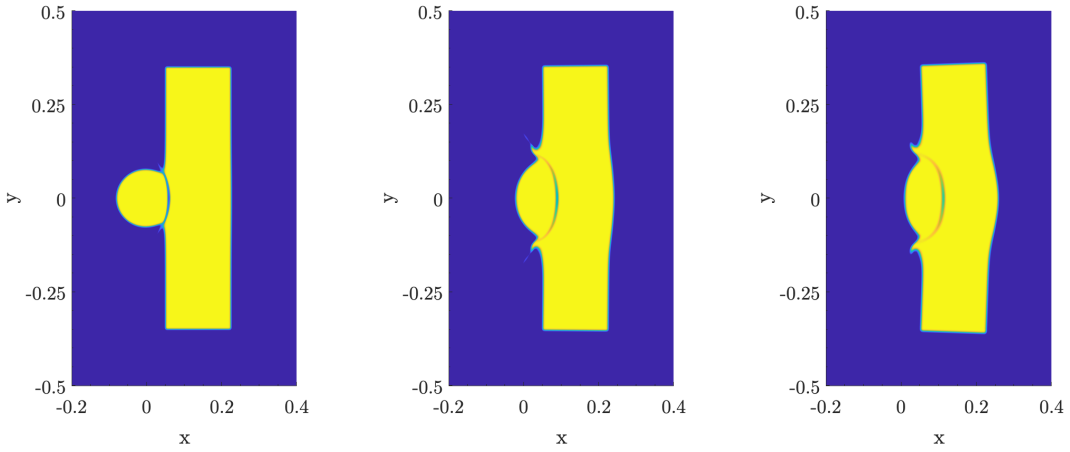

Fig. 19: Results for the multiphase and multi-material elasto-plastic solid impact. The contour levels of the volume fractions of the first and the second phases at times $t = 60$, $t = 100$, and $t = 140$ (from left to right).

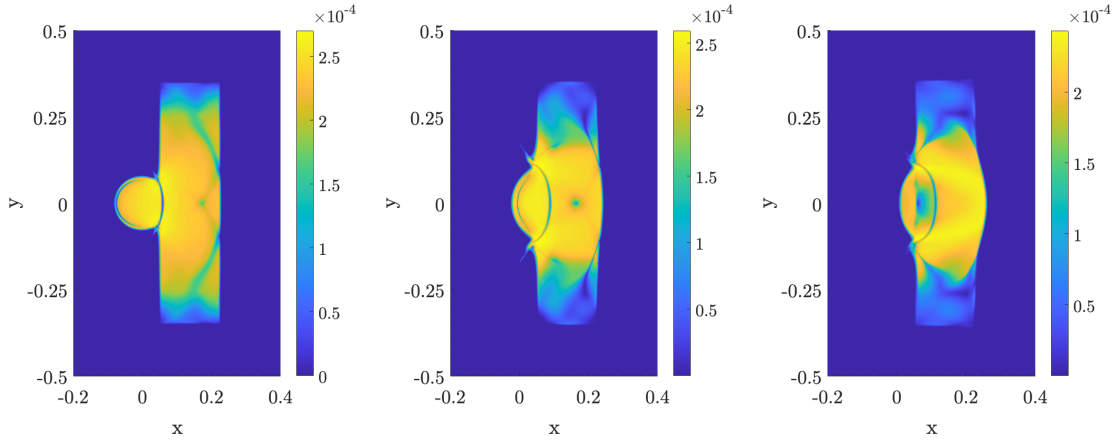

Fig. 20: Results for the multiphase and multi-material elasto-plastic solid impact. The contour levels of the von Mises stress of the first $\bar{\sigma}_1$ and the second $\bar{\sigma}_2$ at times $t = 60$, $t = 100$, and $t = 140$ (from left to right).

propagates through the body by means of waves, which are reflected over time from the body boundaries. On the contrary, in the case of an elasto-plastic material, it can be observed that the stress reaches a lower magnitude than in the ideal elastic case, due to the stress relaxation process in the inelastic deformations. Furthermore, it is evident that over time, the highest stress values are localised in the area undergoing plastic deformations, while the regions far from the impact, in this case, are less stressed.

Finally, to emphasize the multimaterial character of the test, Fig. 21 shows the gas pressure p_3 and the contours of the solid objects. One can see quite complicated flow structures consisting of multiple shock waves interracting with the boundaries of the solid bodies and with each other.

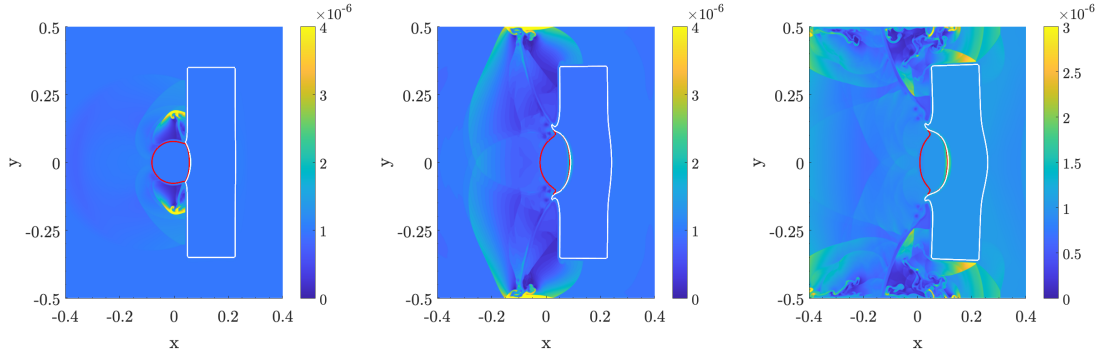

Fig. 21: Results for the multiphase and multi-material elastic-plastic solid impact. The contour levels of the the gas pressure p_3 and the contours of the solids presented at times $t = 60$, $t = 100$, and $t = 140$ (from left to right).

8 Conclusion

The goal of the presented research was to investigate the applicability of the continuous mixture theory to the numerical simulation of multiphase and multi-material flows, and in particular to the fluid structure interaction problems. Within various formulations for the mixture theory, we opted for the SHTC formulation of continuum mechanics and multiphase flows. The finite volume MUSCL-Hancock method was selected due to its robustness and easy adaptability to complex PDE systems like the one presented in this paper.

The multiphase SHTC model [108, 103, 107] was presented in a general non-equilibrium formulation with different phase pressure, velocities, temperatures, etc., and for arbitrary number of phases. The phase can be of different nature, viscous gas or liquid, or elastoplastic solid, and the material interfaces are treated as diffuse interfaces represented by a rapid but smooth change of the corresponding volume fraction function across the interface. This presented level of unification of various materials has been achieved by introducing the unified model of continuum fluid and solid mechanics [96, 39] which also belongs to the SHTC class of equations.

The SHTC formulation was put into a form resembling the Baer-Nunziato (BN) model, which is a popular model within the compressible multiphase community. The motivation for such a reformulation of the SHTC equations was twofold. First, we wanted to demonstrate how the BN model can be extended beyond its two-fluid formulation. The second reason is due to our experience with the numerical discretiztion of the BN model [68] in the past. However, we find out that in a true multiphysics (e.g. including heat conduction, elasticity, phase transition, etc.) and multiphase (more than 2 phase) setting, a BN formulation might be not an optimal choice for building a computational code due to the complexity of the system of equations. Nevertheless, it was a simplified version of the BN form of the SHTC equations that was solved numerically in this work.

Despite being a standard finite volume method, the MUSCL-Hancock scheme required some adaptation to the complicated PDE system presented in this paper. To deal with the presence of non-conservative product terms a path-conservative variant of the scheme is employed. Moreover, in order to cope with the stiff character of the relaxation source terms, the MUSCL-Hancock scheme is implemented in an operator splitting manner with the aid of a specially designed implicit discretization of the sources. Particular attention is also given to the reconstruction phase through a specific reconstruction procedure in the primitive variable space that also performs positivity preserving limiting of certain quantities.

This research will be continued in the future in the following directions. We plan to solve the original SHTC multiphase equations with the help of the new class of Hyperbolic Thermodynamically Compatible (HTC) schemes [20, 1, 125], which will allow to respect most of the structure of the continuous SHTC equations at the discrete level, and to deal with non-isentropic flows due to the natural ability of the HTC schemes to deal with hyperbolic models with multiple entropy inequalities, e.g see [125, 20].

The multiphase SHTC model presented in Sec. 4 can be further extended to include phenomena such as phase transition and surface tension [97, 27], likewise to include the SHTC coupling with electrodynamics [40], e.g. for multifluid plasma models. Also, a proper SHTC multi-distortion formulation for multiphase flows is missing. In this paper, the multi-distortion formulation was achieved in a *ad hoc* manner, and further research is required.

9 Acknowledgments

This work was financially supported by the Italian Ministry of Education, University and Research (MIUR) in the framework of the PRIN 2022 project *High order structure-preserving*

semi-implicit schemes for hyperbolic equations, the PRIN 2022 project No. 2022N9BM3N *Efficient numerical schemes and optimal control methods for time-dependent partial differential equations* and via the Departments of Excellence Initiative 2018–2027 attributed to DICAM of the University of Trento (grant L. 232/2016). M.D. was also co-funded by the European Union NextGenerationEU (PNRR, Spoke 7 CN HPC). Views and opinions expressed are however those of the author(s) only and do not necessarily reflect those of the European Union or the European Research Council. Neither the European Union nor the granting authority can be held responsible for them. E.R. was supported by the state contract of the Sobolev Institute of Mathematics (project no. FWNF-2022-0008) M.D. and I.P. are members of the INdAM GNCS group in Italy.

A Eigenvalue estimates

From the very nature of the hyperbolic equations, it is important to understand the *characteristic* structure of the PDE system (77) under consideration. However, even if simplified with respect to the full SHTC model in (47), this system remains too complex for analytical calculation of all eigenvalues due to coupling of convective, acoustic, and shear parts, as well as due to coupling between the phases. Therefore, since our FV method requires the knowledge of the maximum sound speeds, we shall use some estimates for the eigenvalues discussed below.

As has been suggested in [25] in teh context of -two-fluid model coupled with the GPR model, a practical and effective choice for estimating the spectral radius of the Jacobian matrix for moderate Mach numbers is λ_k^M in each direction x_k as

$$\lambda_k^M = \max_a \left(|\boldsymbol{v}_a \cdot \hat{\boldsymbol{n}}_k + \lambda|, |\boldsymbol{v}_a \cdot \hat{\boldsymbol{n}}_k - \lambda| \right), \qquad \text{with} \qquad \lambda = \sqrt{\lambda_p^2 + \lambda_s^2} \tag{169}$$

where

$$\lambda_p = C_a = p_a \gamma_a / \rho_a \tag{170}$$

accounts for the pressure waves of the multiphase model, while

$$\lambda_s = \sqrt{4\ \mathrm{Cs}_a^2 / 3} \tag{171}$$

is a linearised estimate for contribution by the shear modes. Through our numerical experiments, we found out that (171) is quite safe, leading to only occasional slight overestimates.

B Variational formulation

Here, we provide a variational formulation of the SHTC multifluid heat conducting equations in the Lagrangian coordinates, which extends the variational scheme from [95] for two-fluid systems to the multifluid case. With the variational principle we can only obtain the Eulerian homogeneous multifluid system (19) that represents the reversible part of the overall time evolution. The irreversible part is represented by the relaxation source terms, which are added afterwards in accordance with the second law of thermodynamics and Onsager's principle [95]. Additionally, the following formulation is limited to the case of single distortion field because it remains unclear to us how to extend it to multiple distortion fields.

We consider a vector potential $x_i(t, X_K)$, $i = 1, 2, 3$, N − 1-scalar potentials $\chi_a(t, X_K)$, and another set of N scalar potentials $\varphi_a(t, X_K)$. Here, t is the time, and $x_i(t, X_K)$ is the map (also called motion) between the Lagrangian X_K, $K = 1, 2, 3$ and Eulerian position x_i of the mixture element. The physical meaning of the other potentials might be not clear (similar to the vector

potential in the electrodynamics). Yet, their time derivatives are assumed to have the following meaning

$$\begin{aligned} V_i &= \frac{\mathrm{d}x_i}{\mathrm{d}t}, \qquad & F_{iK} &= \frac{\partial x_i}{\partial X_K}, \\ -\mu_a &= \frac{\mathrm{d}\chi_a}{\mathrm{d}t}, \qquad & w_{a,K} &= \frac{\partial \chi_a}{\partial X_K}, \\ -\vartheta_a &= \frac{\partial \varphi_a}{\partial t}, \qquad & J_{a,K} &= \frac{\partial \varphi_a}{\partial X_K}, \end{aligned} \tag{172}$$

where μ_a, $a = 1, \ldots, \mathrm{N}-1$ stands for the phase chemical potential, while ϑ_a, $a = 1, \ldots, \mathrm{N}$ is the phase temperature. Also, $\mathrm{d}/\mathrm{d}t$ should be understood as the material time derivative.

The action integral can be defined in a general form

$$\mathcal{L} = \int \Lambda(x_i, \chi_a, \varphi_a; \mathrm{d}_t x_i, \partial_K x_i, \mathrm{d}_t \chi_a, \partial_K \chi_a, \mathrm{d}_t \varphi_a, \partial_K \varphi_a) \mathrm{d}t \mathrm{d}\boldsymbol{X}, \tag{173}$$

with the Lagrangian density Λ being a function (unspecified at the moment) of the potentials x_i, χ_a, φ_a, and their time and space gradients denoted with the symbols $\mathrm{d}_t = \mathrm{d}/\mathrm{d}t$ and $\partial_K = \partial/\partial X_K$. However, for our purposes, the explicit dependence of Λ on x_i, χ_a, and φ_a is not required.

One can immediately write down the Euler-Lagrange equations corresponding to this action integral:

$$\frac{\mathrm{d}\Lambda_{V_i}}{\mathrm{d}t} + \frac{\partial \Lambda_{F_{iK}}}{\partial X_K} = 0, \tag{174a}$$

$$-\frac{\mathrm{d}\Lambda_{\mu_a}}{\mathrm{d}t} + \frac{\partial \Lambda_{w_{a,K}}}{\partial X_K} = 0, \tag{174b}$$

$$-\frac{\mathrm{d}\Lambda_{\vartheta_a}}{\mathrm{d}t} + \frac{\partial \Lambda_{J_{a,K}}}{\partial X_K} = 0, \tag{174c}$$

and the following space-time integrability conditions

$$\frac{\mathrm{d}F_{iJ}}{\mathrm{d}t} - \frac{\partial V_i}{\partial X_K} = 0, \tag{175a}$$

$$\frac{\mathrm{d}w_{a,K}}{\mathrm{d}t} + \frac{\partial \mu_a}{\partial X_K} = 0, \tag{175b}$$

$$\frac{\mathrm{d}J_{a,K}}{\mathrm{d}t} + \frac{\partial \vartheta_a}{\partial X_K} = 0. \tag{175c}$$

and pure spatial integrability conditions

$$\frac{\partial F_{iI}}{\partial X_K} - \frac{\partial F_{iK}}{\partial X_I} = 0, \qquad \frac{\partial w_{a,I}}{\partial X_K} - \frac{\partial w_{a,K}}{\partial X_I} = 0, \qquad \frac{\partial J_{a,I}}{\partial X_K} - \frac{\partial J_{a,K}}{\partial X_I} = 0. \tag{176}$$

which are trivial consequences of definitions (172).

After introducing new unknowns (mixture momentum U_i)

$$U_i = \Lambda_{V_i}, \quad \varrho_a = -\Lambda_{\mu_a}, \quad \eta_a = -\Lambda_{\vartheta_a}, \tag{177}$$

a new potential

$$\mathcal{U}(U_i, F_{iJ}, \varrho_a, w_{a,K}, \eta_a, J_{a,K}) = V_i \Lambda_{V_i} - \mu_a \Lambda_{\mu_a} - \vartheta_a \Lambda_{\vartheta_a} - \Lambda, \tag{178}$$

and noting that the derivatives of the old potential and new potential are related by

$$\mathcal{U}_{F_{iI}} = -\Lambda_{F_{iI}}, \quad \mathcal{U}_{w_{a,I}} = \Lambda_{w_{a,I}}, \quad \mathcal{U}_{J_{a,I}} = \Lambda_{J_{a,I}}, \tag{179}$$

$$U_i = \mathcal{U}_{V_i}, \quad \mu_a = \mathcal{U}_{\varrho_a}, \quad \vartheta_a = \mathcal{U}_{\eta_a}, \tag{180}$$

we can rewrite the Euler-Lagrange equations (174) and the integrability conditions (175) in the following form

$$\frac{\mathrm{d}U_i}{\mathrm{d}t} - \frac{\partial \mathcal{U}_{F_{iK}}}{\partial X_K} = 0, \tag{181a}$$

$$\frac{\mathrm{d}F_{iK}}{\mathrm{d}t} - \frac{\partial \mathcal{U}_{U_i}}{\partial X_K} = 0, \tag{181b}$$

$$\frac{\mathrm{d}\varrho_a}{\mathrm{d}t} + \frac{\partial \mathcal{U}_{w_{a,K}}}{\partial X_K} = 0, \tag{181c}$$

$$\frac{\mathrm{d}w_{a,K}}{\mathrm{d}t} + \frac{\partial \mathcal{U}_{\varrho_a}}{\partial X_K} = 0, \tag{181d}$$

$$\frac{\mathrm{d}\eta_a}{\mathrm{d}t} + \frac{\partial \mathcal{U}_{J_{a,K}}}{\partial X_K} = 0, \tag{181e}$$

$$\frac{\mathrm{d}J_{a,K}}{\mathrm{d}t} + \frac{\partial \mathcal{U}_{\eta_a}}{\partial X_K} = 0, \tag{181f}$$

The conversion from the SHTC Lagrangian master system (181), which admits the original Godunov structure [50], to the Eulerian system (19) can be carried out by means of the Lagrange-to-Euler coordinate transformation which also concerns the change of the state variables, potential $\mathcal{U}$, and is described in detail in [95, 53].

References

[1] R. Abgrall, S. Busto, and M. Dumbser. "A simple and general framework for the construction of thermodynamically compatible schemes for computational fluid and solid mechanics". *Applied Mathematics and Computation* 440 (2023), p. 127629. DOI: https://doi.org/10.1016/j.amc.2022.127629 (Cited on pp. 2, 5, 34, 61).

[2] R. Abgrall and R. Saurel. "Discrete equations for physical and numerical compressible multiphase mixtures". *Journal of Computational Physics* 186 (2003), pp. 361–396 (Cited on p. 18).

[3] N. Andrianov and G. Warnecke. "The Riemann problem for the Baer-Nunziato two-phase flow model". *Journal of Computational Physics* 212 (2004), pp. 434–464 (Cited on p. 18).

[4] M. Baer and J. Nunziato. "A two-phase mixture theory for the deflagration-to-detonation transition (DDT) in reactive granular materials". *International Journal of Multiphase Flow* 12.6 (1986), pp. 861–889 (Cited on pp. 3, 4, 18).

[5] D. Balsara and C.-W. Shu. "Monotonicity Preserving Weighted Essentially Non-oscillatory Schemes with Increasingly High Order of Accuracy". *Journal of Computational Physics* 160.2 (2000), pp. 405–452. DOI: https://doi.org/10.1006/jcph.2000.6443 (Cited on p. 35).

[6] P. T. Barton, D. Drikakis, and E. I. Romenski. "An Eulerian finite-volume scheme for large elastoplastic deformations in solids". *International Journal for Numerical Methods in Engineering* 81.4 (2010), pp. 453–484. DOI: https://doi.org/10.1002/nme.2695 (Cited on pp. 45, 47).

[7] J. Bdzil, R. Menikoff, S. Son, A. Kapila, and D. Stewart. "Two-phase modeling of deflagration-to-detonation transition in granular materials: A critical examination of modeling issues". *Physics of Fluids* 11.2 (1999), pp. 378–402 (Cited on p. 3).

[8] J. Bell, P. Coletta, and H. Glaz. "A Second-Order Projection Method for the Incompressible Navier-Stokes Equations". *Journal of Computational Physics* 85 (1989), pp. 257–283 (Cited on pp. 38, 40).

[9] A. Bermúdez, S. Busto, M. Dumbser, J. Ferrín, L. Saavedra, and M. Vázquez-Cendón. "A staggered semi-implicit hybrid FV/FE projection method for weakly compressible flows". *Journal of Computational Physics* 421 (2020), p. 109743. DOI: https://doi.org/10.1016/j.jcp.2020.109743 (Cited on p. 40).

[10] W. Bo and M. Shashkov. "Adaptive reconnection-based arbitrary Lagrangian Eulerian method". *Journal of Computational Physics* 299 (2015), pp. 902–939 (Cited on pp. 4, 49).

[11] W. Boscheri, S. Chiocchetti, and I. Peshkov. "A cell-centered implicit-explicit Lagrangian scheme for a unified model of nonlinear continuum mechanics on unstructured meshes". *Journal of Computational Physics* 451 (2022), p. 110852. DOI: https://doi.org/10.1016/j.jcp.2021.110852 (Cited on pp. 4, 5).

[12] W. Boscheri, M. Dumbser, M. Ioriatti, I. Peshkov, and E. Romenski. "A structure-preserving staggered semi-implicit finite volume scheme for continuum mechanics". *Journal of Computational Physics* 424 (2021), p. 109866 (Cited on pp. 5, 9, 40).

[13] W. Boscheri, M. Dumbser, and R. Loubère. "Cell centered direct Arbitrary-Lagrangian-Eulerian ADER-WENO finite volume schemes for nonlinear hyperelasticity". *Computers and Fluids* 134–135 (2016), pp. 111–129 (Cited on pp. 42, 44, 45, 48).

[14] W. Boscheri, R. Loubère, and M. Dumbser. "Direct Arbitrary-Lagrangian–Eulerian ADER-MOOD finite volume schemes for multidimensional hyperbolic conservation laws". *Journal of Computational Physics* 292 (2015), pp. 56–87 (Cited on pp. 4, 49).

[15] A. de Brauer, A. Iollo, and T. Milcent. "A Cartesian Scheme for Compressible Multimaterial Hyperelastic Models with Plasticity". *Communications in Computational Physics* 22.05 (2017), pp. 1362–1384. DOI: 10.4208/cicp.OA-2017-0018 (Cited on pp. 57, 58).

[16] J. Breil, T. Harribey, P. Maire, and M. Shashkov. "A multi-material ReALE method with MOF interface reconstruction". *Computers & Fluids* 83 (2013), pp. 115–125 (Cited on pp. 4, 49).

[17] D. Burton, N. Morgan, T. Carney, and M. Kenamond. "Reduction of dissipation in Lagrange cell-centered hydrodynamics (CCH) through corner gradient reconstruction (CGR)". *Journal of Computational Physics* 299 (2015), pp. 229–280 (Cited on pp. 42, 44).

[18] S. Busto, S. Chiocchetti, M. Dumbser, E. Gaburro, and I. Peshkov. "High Order ADER Schemes for Continuum Mechanics". *Frontiers in Physics* 8 (2020) (Cited on pp. 2, 44, 45).

[19] S. Busto and M. Dumbser. "A New Family of Thermodynamically Compatible Discontinuous Galerkin Methods for Continuum Mechanics and Turbulent Shallow Water Flows". *Journal of Scientific Computing* 93.2 (2022), p. 56. DOI: 10.1007/s10915-022-02017-0 (Cited on p. 5).

[20] S. Busto, M. Dumbser, S. Gavrilyuk, and K. Ivanova. "On Thermodynamically Compatible Finite Volume Methods and Path-Conservative ADER Discontinuous Galerkin Schemes for Turbulent Shallow Water Flows". *Journal of Scientific Computing* 88.1 (2021), p. 28. DOI: 10.1007/s10915-021-01521-z (Cited on pp. 5, 61).

[21] S. Busto, M. Dumbser, I. Peshkov, and E. Romenski. "On Thermodynamically Compatible Finite Volume Schemes for Continuum Mechanics". *SIAM Journal on Scientific Computing* 44.3 (2022), A1723–A1751. DOI: 10.1137/21M1417508 (Cited on pp. 2, 5, 34, 36, 38, 40).

[22] M. Castro, J. Gallardo, and C. Parés. "High Order Finite Volume Schemes Based on Reconstruction of States for Solving Hyperbolic Systems with Nonconservative Products. Applications to Shallow-Water Systems". *Mathematics of Computation* 75.255 (2006), pp. 1103–1134 (Cited on pp. 28, 29).

[23] M. Castro, J. Gallardo, J. López, and C. Parés. "Well-balanced high order extensions of Godunov's method for semilinear balance laws". *SIAM Journal of Numerical Analysis* 46 (2008), pp. 1012–1039 (Cited on p. 29).

[24] M. Castro, A. Pardo, C. Parés, and E. Toro. "On some fast well-balanced first order solvers for nonconservative systems". *Mathematics of Computation* 79 (2010), pp. 1427–1472 (Cited on p. 29).

[25] S. Chiocchetti and M. Dumbser. "An Exactly Curl-Free Staggered Semi-Implicit Finite Volume Scheme for a First Order Hyperbolic Model of Viscous Two-Phase Flows with Surface Tension". *Journal of Scientific Computing* 94 (2023), p. 24 (Cited on pp. 4, 5, 26, 31, 32, 33, 38, 40, 48, 62).

[26] S. Chiocchetti and C. Müller. "A Solver for Stiff Finite-Rate Relaxation in Baer–Nunziato Two-Phase Flow Models". In: *Droplet Interactions and Spray Processes*. Ed. by G. Lamanna, S. Tonini, G. Cossali, and B. Weigand. Cham: Springer International Publishing, 2020, pp. 31–44 (Cited on pp. 4, 31).

[27] S. Chiocchetti, I. Peshkov, S. Gavrilyuk, and M. Dumbser. "High order ADER schemes and GLM curl cleaning for a first order hyperbolic formulation of compressible flow with surface tension". *Journal of Computational Physics* 426 (2021), p. 109898. DOI: https://doi.org/10.1016/j.jcp.2020.109898 (Cited on pp. 24, 61).

[28] B. Coleman and W. Noll. "The thermodynamics of elastic materials with heat conduction and viscosity". *Archive for Rational Mechanics and Analysis* 13.1 (1963), pp. 167–178. DOI: 10.1007/BF01262690 (Cited on p. 3).

[29] R. Courant, K. Friedrichs, and H. Lewy. "Über die partiellen Differenzgleichungen der mathematische Physik". *Mathematische Annalen* 100 (1928), pp. 32–74 (Cited on p. 29).

[30] C. Crowe, M. Sommerfeld, and Y. Tsuji. *Multiphase Flows with Droplets and Particles*. Boca Raton: CRC Press, 1998 (Cited on p. 3).

[31] A. de Brauer, A. Iollo, and T. Milcent. "A Cartesian scheme for compressible multimaterial models in 3D". *Journal of Computational Physics* 313 (2016), pp. 121–143. DOI: https://doi.org/10.1016/j.jcp.2016.02.032 (Cited on p. 57).

[32] V. Deledicque and M. Papalexandris. "An exact Riemann solver for compressible two-phase flow models containing non-conservative products". *Journal of Computational Physics* 222 (2007), pp. 217–245 (Cited on p. 18).

[33] F. Dhaouadi and S. Gavrilyuk. "An Eulerian hyperbolic model for heat transfer derived via Hamilton's principle: analytical and numerical study". *Proceedings of the Royal Society A: Mathematical, Physical and Engineering Sciences* 480.2283 (2024). DOI: 10.1098/rspa.2023.0440 (Cited on p. 12).

[34] V. Dobrev, T. Kolev, and R. Rieben. "High order curvilinear finite elements for elastic-plastic Lagrangian dynamics". *Journal of Computational Physics* 257 (2014), pp. 1062–1080. DOI: 10.1016/j.jcp.2013.01.015 (Cited on p. 45).

[35] D. Drew and L. Segel. "Averaged Equations for Two-Phase Flows". *Studies in Applied Mathematics* 50 (1971), pp. 205–231 (Cited on p. 3).

[36] M. Dumbser. "A simple two-phase method for the simulation of complex free surface flows". *Computer Methods in Applied Mechanics and Engineering* 200 (2011), pp. 1204–1219 (Cited on p. 4).

[37] M. Dumbser and V. Casulli. "A conservative, weakly nonlinear semi-implicit finite volume method for the compressible Navier-Stokes equations with general equation of state". *Applied Mathematics and Computation* 272 (2016), pp. 479–497 (Cited on p. 40).

[38] M. Dumbser, A. Hidalgo, M. Castro, C. Parès, and E. Toro. "FORCE Schemes on Unstructured Meshes II: Non–Conservative Hyperbolic Systems". *Computer Methods in Applied Mechanics and Engineering* 199 (2010), pp. 625–647 (Cited on pp. 18, 29).

[39] M. Dumbser, I. Peshkov, E. Romenski, and O. Zanotti. "High order ADER schemes for a unified first order hyperbolic formulation of continuum mechanics: Viscous heat-conducting fluids and elastic solids". *Journal of Computational Physics* 314 (2016), pp. 824–862. DOI: https://doi.org/10.1016/j.jcp.2016.02.015 (Cited on pp. 2, 5, 9, 11, 14, 15, 38, 40, 61).

[40] M. Dumbser, I. Peshkov, E. Romenski, and O. Zanotti. "High order ADER schemes for a unified first order hyperbolic formulation of Newtonian continuum mechanics coupled with electro-dynamics". *Journal of Computational Physics* 348 (2017), pp. 298–342. DOI: https://doi.org/10.1016/j.jcp.2017.07.020 (Cited on pp. 5, 61).

[41] P. Embid and M. Baer. "Mathematical analysis of a two-phase continuum mixture theory". *Continuum Mechanics and Thermodynamics* 4.4 (1992), pp. 279–312. DOI: 10.1007/BF01129333 (Cited on p. 3).

[42] N. Favrie and S. Gavrilyuk. "Diffuse interface model for compressible fluid-compressible elastic-plastic solid interaction". *Journal of Computational Physics* 232 (2012), pp. 2695–2723 (Cited on p. 4).

[43] N. Favrie, S. Gavrilyuk, and R. Saurel. "Solid–fluid diffuse interface model in cases of extreme deformations". *Journal of Computational Physics* 228 (2009), pp. 6037–6077 (Cited on pp. 2, 4).

[44] D. Ferrari and M. Dumbser. "A Semi-implicit Finite Volume Scheme for Incompressible Two-Phase Flows". *Communications on Applied Mathematics and Computation* (2023). DOI: https://doi.org/10.1007/s42967-024-00367-0 (Cited on pp. 53, 55, 56).

[45] K. Friedrichs. "Symmetric positive linear differential equations". *Communications on Pure and Applied Mathematics* 11.3 (1958), pp. 333–418. DOI: 10.1002/cpa.3160110306 (Cited on p. 5).

[46] E. Gaburro, W. Boscheri, S. Chiocchetti, C. Klingenberg, V. Springel, and M. Dumbser. "High order direct Arbitrary–Lagrangian–Eulerian schemes on moving Voronoi meshes with topology changes". *Journal of Computational Physics* 407 (2020), p. 109167. DOI: https://doi.org/10.1016/j.jcp.2019.109167 (Cited on pp. 4, 49, 51).

[47] E. Gaburro, M. Castro, and M. Dumbser. "A well balanced diffuse interface method for complex nonhydrostatic free surface flows". *Computers & Fluids* 175 (2018), pp. 180–198 (Cited on p. 4).

[48] S. Gavrilyuk and H. Gouin. “A new form of governing equations of fluids arising from Hamilton’s principle”. *International Journal of Engineering Science* 37.12 (1999), pp. 1495–1520. DOI: 10.1016/S0020-7225(98)00131-1 (Cited on p. 3).

[49] U. Ghia, K. Ghia, and C. Shin. “High-Re solutions for incompressible flow using Navier-Stokes equations and multigrid method”. *Journal of Computational Physics* 48 (1982), pp. 387–411 (Cited on pp. 40, 42).

[50] S. Godunov. “An interesting class of quasilinear systems”. *Dokl. Akad. Nauk SSSR* 139(3) (1961), pp. 521–523 (Cited on pp. 2, 5, 64).

[51] S. Godunov. “Symmetric form of the magnetohydrodynamic equation”. *Numerical Methods for Mechanics of Continuum Medium* 3.1 (1972), pp. 26–34 (Cited on pp. 2, 5).

[52] S. Godunov. *Elements of mechanics of continuous media*. Nauka, 1978 (Cited on p. 33).

[53] S. Godunov, T. Mikhaîlova, and E. Romenskiî. “Systems of thermodynamically coordinated laws of conservation invariant under rotations”. *Siberian Mathematical Journal* 37.4 (1996), pp. 690–705. DOI: 10.1007/BF02104662 (Cited on pp. 2, 5, 8, 17, 64).

[54] S. Godunov and E. Romenski. “Thermodynamics, conservation laws and symmetric forms of differential equations in mechanics of continuous media”. *Computational fluid dynamics review* 95 (1995), pp. 19–31 (Cited on pp. 5, 8, 17).

[55] S. Godunov and E. Romenskii. *Elements of continuum mechanics and conservation laws*. Kluwer Academic/Plenum Publishers, 2003 (Cited on pp. 2, 7, 9, 15, 31, 32).

[56] S. Godunov and E. Romenskiî. *Elements of mechanics of continuous media*. Nauchnaya Kniga, 1998 (Cited on p. 2).

[57] H. Gouin and T. Ruggeri. “Hamiltonian principle in the binary mixtures of Euler fluids with applications to the second sound phenomena”. *Atti della Accademia Nazionale dei Lincei. Classe di Scienze Fisiche, Matematiche e Naturali. Rendiconti Lincei. Matematica e Applicazioni* 14 (2003), pp. 69–83 (Cited on p. 3).

[58] M. Grmela and H. Öttinger. “Dynamics and thermodynamics of complex fluids. I. Development of a general formalism”. *Physical Review E* 56.6 (1997), pp. 6620–6632. DOI: 10.1103/PhysRevE.56.6620 (Cited on p. 3).

[59] M. Gurtin and A. Vargas. “On the classical theory of reacting fluid mixtures”. *Archive for Rational Mechanics and Analysis* 43.3 (1971), pp. 179–197. DOI: 10.1007/BF00251451 (Cited on pp. 3, 18).

[60] J. Hérard. “A three-phase flow model”. *Mathematical and Computer Modelling* 45 (2007), pp. 732–755 (Cited on pp. 4, 18, 22).

[61] J. Hérard and H. Mathis. “A three-phase flow model with two miscible phases”. *ESAIM: Mathematical Modelling and Numerical Analysis* 53 (2019), pp. 1373–1389 (Cited on pp. 4, 18, 22).

[62] C. Hirt and B. Nichols. “Volume of Fluid (VOF) Method for Dynamics of Free Boundaries”. *Journal of Computational Physics* 39 (1981), pp. 201–225 (Cited on p. 4).

[63] C. Hu and C.-W. Shu. “Weighted Essentially Non-oscillatory Schemes on Triangular Meshes”. *Journal of Computational Physics* 150.1 (1999), pp. 97–127. DOI: https://doi.org/10.1006/jcph.1998.6165 (Cited on p. 35).

[64] Z. Huang and E. Johnson. “A consistent and conservative phase-field method for compressible N-phase flows: Consistent limiter and multiphase reduction-consistent formulation”. *Journal of Computational Physics* 501 (2024), p. 112801 (Cited on p. 18).

[65] M. Ishii. “Thermo-fluid Dynamic Theory of Two-phase Flow”. *Eyrolles* (1975) (Cited on p. 3).

[66] H. Jackson. “A fast numerical scheme for the Godunov-Peshkov-Romenski model of continuum mechanics”. *Journal of Computational Physics* 348 (2017), pp. 514–533. DOI: 10.1016/J.JCP.2017.07.055 (Cited on p. 5).

[67] H. Jackson and N. Nikiforakis. “A numerical scheme for non-Newtonian fluids and plastic solids under the GPR model”. *Journal of Computational Physics* 387 (2019), pp. 410–429 (Cited on pp. 5, 7, 15).

[68] F. Kemm, E. Gaburro, F. Thein, and M. Dumbser. “A simple diffuse interface approach for compressible flows around moving solids of arbitrary shape based on a reduced Baer–Nunziato model”. *Computers & Fluids* 204 (2020), p. 104536 (Cited on pp. 4, 61).

[69] M. Kucharik and M. Shashkov. “Conservative multi-material remap for staggered multi-material Arbitrary Lagrangian-Eulerian methods”. *Journal of Computational Physics* 258 (2014), pp. 268–304 (Cited on pp. 4, 49).

[70] I. Liu and I. Müller. “Thermodynamics of Mixtures of Fluids”. In: *Rational Thermodynamics*. New York, NY: Springer New York, 1984, pp. 264–285. DOI: 10.1007/978-1-4612-5206-1_14 (Cited on p. 3).

[71] R. Loubère, P. Maire, and M. Shashkov. "ReALE: A Reconnection Arbitrary–Lagrangian-Eulerian method in cylindrical geometry". *Computers and Fluids* 46 (2011), pp. 59–69 (Cited on pp. 4, 49, 51).

[72] R. Loubère, P. Maire, M. Shashkov, J. Breil, and S. Galera. "ReALE: A reconnection-based arbitrary-Lagrangian–Eulerian method". *Journal of Computational Physics* 229 (2010), pp. 4724–4761 (Cited on pp. 49, 51).

[73] M. Lukáčová-Medvid'ová, I. Peshkov, and A. Thomann. "An implicit-explicit solver for a two-fluid single-temperature model". *Journal of Computational Physics* 498 (2024), p. 112696. DOI: https://doi.org/10.1016/j.jcp.2023.112696 (Cited on p. 5).

[74] M. Lukáčová-Medvid'ová, G. Puppo, and A. Thomann. "An all Mach number finite volume method for isentropic two-phase flow". *Journal of Numerical Mathematics* (2022). DOI: 10.1515/jnma-2022-0015 (Cited on p. 5).

[75] P. Maire, R. Abgrall, J. Breil, R. Loubère, and B. Rebourcet. "A nominally second-order cell-centered Lagrangian scheme for simulating elastic–plastic flows on two-dimensional unstructured grids". *Journal of Computational Physics* 235 (2013), pp. 626–665. DOI: https://doi.org/10.1016/j.jcp.2012.10.017 (Cited on pp. 42, 44, 45, 48).

[76] A. Malyshev and E. Romenskii. "Hyperbolic equations for heat transfer. Global solvability of the Cauchy problem". *Siberian Mathematical Journal* 27.5 (1986), pp. 734–740 (Cited on p. 9).

[77] I. Menshov and P. Zakharov. "On the composite Riemann problem for multi-material fluid flows". *International Journal for Numerical Methods in Fluids* 76.2 (2014), pp. 109–127. DOI: https://doi.org/10.1002/fld.3927 (Cited on p. 4).

[78] I. Müller. "A thermodynamic theory of mixtures of fluids". *Archive for Rational Mechanics and Analysis* 28.1 (1968), pp. 1–39. DOI: 10.1007/BF00281561 (Cited on pp. 3, 18).

[79] I. Müller and T. Ruggeri. *Rational Extended Thermodynamics*. Vol. 16. Springer, 1998 (Cited on pp. 3, 5, 17).

[80] C. Munz. "On the construction and comparison of two-step schemes for the Euler equations". *Notes Numer. Fluid Mech.* 14 (1986), pp. 195–217 (Cited on p. 24).

[81] S. Ndanou, N. Favrie, and S. Gavrilyuk. "Multi–solid and multi–fluid diffuse interface model: Applications to dynamic fracture and fragmentation". *Journal of Computational Physics* 295 (2015), pp. 523–555 (Cited on pp. 2, 4, 21).

[82] R. Nigmatulin. *Dynamics of Multiphase Media*. New York: Hemisphere, 1991 (Cited on pp. 3, 18).

[83] M. Nikodemou. "A unified multi-physics formulation for combustion modelling". PhD thesis. University of Cambridge, 2023. DOI: 10.17863/CAM.99670 (Cited on pp. 2, 8, 21).

[84] M. Nikodemou, L. Michael, and N. Nikiforakis. "A unified multi-phase and multi-material formulation for combustion modeling". *Physics of Fluids* 33.10 (2021). DOI: 10.1063/5.0064772 (Cited on pp. 2, 8, 21).

[85] J. Nunziato and E. Walsh. "On ideal multiphase mixtures with chemical reactions and diffusion". *Archive for Rational Mechanics and Analysis* 73.4 (1980), pp. 285–311. DOI: 10.1007/BF00247672 (Cited on p. 3).

[86] G. Oger, M. Doring, B. Alessandrini, and P. Ferrant. "Two-dimensional SPH simulations of wedge water entries". *Journal of Computational Physics* 213 (2006), pp. 803–822 (Cited on p. 53).

[87] H. Öttinger and M. Grmela. "Dynamics and thermodynamics of complex fluids. II. Illustrations of a general formalism". *Physical Review E* 56.6 (1997), pp. 6633–6655. DOI: 10.1103/PhysRevE.56.6633 (Cited on p. 3).

[88] C. Parés. "Numerical methods for nonconservative hyperbolic systems: a theoretical framework." *SIAM Journal on Numerical Analysis* 44.1 (2006), pp. 300–321. DOI: 10.1137/050628052 (Cited on pp. 4, 28, 29).

[89] S. Passman, J. Nunziato, and E. Walsh. "A Theory of Multiphase Mixtures". In: *Rational Thermodynamics*. New York, NY: Springer New York, 1984, pp. 286–325. DOI: 10.1007/978-1-4612-5206-1_15 (Cited on pp. 3, 18).

[90] M. Pavelka, V. Klika, and M. Grmela. *Multiscale Thermo-Dynamics*. Berlin, Boston: De Gruyter, 2018. DOI: 10.1515/9783110350951 (Cited on pp. 3, 13).

[91] M. Pelanti and K. Shuyue. "A numerical model for multiphase liquid-vapor-gas flows with interfaces and cavitation". *International Journal of Multiphase Flow* 113 (2019), pp. 208–230 (Cited on p. 4).

[92] I. Peshkov, W. Boscheri, R. Loubère, E. Romenski, and M. Dumbser. "Theoretical and numerical comparison of hyperelastic and hypoelastic formulations for Eulerian non–linear elastoplasticity". *Journal of Computational Physics* 387 (2019), pp. 481–521 (Cited on pp. 7, 15, 42, 44, 45, 47).

[93] I. Peshkov, M. Dumbser, W. Boscheri, E. Romenski, S. Chiocchetti, and M. Ioriatti. "Simulation of non-Newtonian viscoplastic flows with a unified first order hyperbolic model and a structure-preserving semi-implicit scheme". *Computers & Fluids* 224 (2021), p. 104963. DOI: 10.1016/j.compfluid.2021.104963 (Cited on pp. 5, 7, 15).

[94] I. Peshkov, M. Grmela, and E. Romenski. "Irreversible mechanics and thermodynamics of two-phase continua experiencing stress-induced solid–fluid transitions". *Continuum Mechanics and Thermodynamics* (2014), DOI 10.1007/s00161-014-0386–1. DOI: 10.1007/s00161-014-0386-1 (Cited on p. 33).

[95] I. Peshkov, M. Pavelka, E. Romenski, and M. Grmela. "Continuum mechanics and thermodynamics in the Hamilton and the Godunov-type formulations". *Continuum Mechanics and Thermodynamics* 30.6 (2018), pp. 1343–1378. DOI: 10.1007/s00161-018-0621-2 (Cited on pp. 2, 3, 5, 8, 13, 17, 62, 64).

[96] I. Peshkov and E. Romenski. "A hyperbolic model for viscous Newtonian flows". *Continuum Mechanics and Thermodynamics* 28.1-2 (2016), pp. 85–104. DOI: 10.1007/s00161-014-0401-6 (Cited on pp. 2, 5, 7, 9, 11, 14, 15, 21, 61).

[97] I. Peshkov, E. Romenski, and M. Pavelka. "Nonequilibrium model for compressible two-phase two-pressure flows with surface tension" (2023) (Cited on pp. 5, 61).

[98] E. Pimentel-García, M. Castro, C. Chalons, T. Morales de Luna, and C. Parés. "In-cell discontinuous reconstruction path-conservative methods for non conservative hyperbolic systems - Second-order extension". *Journal of Computational Physics* 459 (2022), p. 111152 (Cited on p. 4).

[99] S. Popinet. "Numerical Models of Surface Tension". *Annual Review of Fluid Mechanics* 50.1 (2018), pp. 49–75. DOI: 10.1146/annurev-fluid-122316-045034 (Cited on p. 4).

[100] J. Powers, D. Stewart, and H. Krier. "Theory of two-phase detonation—Part I: Modeling". *Combustion and Flame* 80.3 (1990), pp. 264–279. DOI: https://doi.org/10.1016/0010-2180(90)90104-Y (Cited on p. 3).

[101] B. Re and R. Abgrall. "A pressure-based method for weakly compressible two-phase flows under a Baer–Nunziato type model with generic equations of state and pressure and velocity disequilibrium". *Int. J. Num. Meth. Fluids* 94 (2022), pp. 1183–1232 (Cited on p. 18).

[102] L. Río-Martín and M. Dumbser. "High-order ADER Discontinuous Galerkin schemes for a symmetric hyperbolic model of compressible barotropic two-fluid flows". *Communications on Applied Mathematics and Computation* (2023). DOI: 10.1007/s42967-023-00313-6 (Cited on p. 5).

[103] E. Romenski, A. Belozerov, and I. Peshkov. "Conservative formulation for compressible multiphase flows". *Quarterly of Applied Mathematics* 74.1 (2016), pp. 113–136 (Cited on pp. 5, 8, 21, 61).

[104] E. Romenski, D. Drikakis, and E. Toro. "Conservative Models and Numerical Methods for Compressible Two-Phase Flow". *Journal of Scientific Computing* 42(1) (2010), pp. 68–95 (Cited on pp. 2, 5, 8).

[105] E. Romenski, I. Peshkov, M. Dumbser, and F. Fambri. "A new continuum model for general relativistic viscous heat-conducting media". *Philosophical Transactions of the Royal Society A: Mathematical, Physical and Engineering Sciences* 378.2170 (2020), p. 20190175. DOI: 10.1098/rsta.2019.0175 (Cited on pp. 5, 9).

[106] E. Romenski, G. Reshetova, and I. Peshkov. "Two-phase hyperbolic model for porous media saturated with a viscous fluid and its application to wavefields simulation". *Applied Mathematical Modelling* 106 (2022), pp. 567–600. DOI: 10.1016/j.apm.2022.02.021 (Cited on pp. 5, 7, 8).

[107] E. Romenski, G. Reshetova, I. Peshkov, and M. Dumbser. "Modeling wavefields in saturated elastic porous media based on thermodynamically compatible system theory for two-phase solid-fluid mixtures". *Computers & Fluids* 206 (2020), p. 104587. DOI: 10.1016/j.compfluid.2020.104587 (Cited on pp. 5, 7, 8, 61).

[108] E. Romenski, A. Resnyansky, and E. Toro. "Conservative hyperbolic formulation for compressible two-phase flow with different phase pressures and temperatures". *Quarterly of Applied Mathematics* 65.2 (2007), pp. 259–279. DOI: 10.1090/S0033-569X-07-01051-2 (Cited on pp. 2, 5, 8, 15, 19, 20, 21, 61).

[109] E. Romenski and E. Toro. "Compressible two-phase flows: Two-pressure models and numerical methods". *Comput. Fluid Dyn. J* 13.April (2004), pp. 1–30 (Cited on pp. 2, 5, 19, 20).

[110] E. Romensky. "Hyperbolic systems of thermodynamically compatible conservation laws in continuum mechanics". *Mathematical and computer modelling* 28(10) (1998), pp. 115–130 (Cited on pp. 2, 5, 8, 17).

[111] E. Romensky. "Thermodynamics and hyperbolic systems of balance laws in continuum mechanics". In: *Godunov Methods: Theory and Applications*. Ed. by E. Toro. New York: Springer US, 2001. DOI: 10.1007/978-1-4615-0663-8 (Cited on pp. 2, 5, 8, 17).

[112] S. Sambasivan, M. Shashkov, and D. Burton. "A finite volume cell-centered Lagrangian hydrodynamics approach for solids in general unstructured grids". *International Journal for Numerical Methods in Fluids* 72 (2013), pp. 770–810 (Cited on pp. 42, 44, 45).

[113] R. Saurel and R. Abgrall. “A multiphase Godunov method for compressible multifluid and multiphase flows”. *Journal of Computational Physics* 150 (1999), pp. 425–467 (Cited on p. 18).

[114] R. Saurel, O. L. Metayer, J. Massoni, and S. Gavrilyuk. “Shock jump relations for multiphase mixtures with stiff mechanical relaxation”. *Shock Waves* 16(3) (2007), pp. 209–232 (Cited on p. 19).

[115] R. Saurel and C. Pantano. “Diffuse-Interface Capturing Methods for Compressible Two-Phase Flows”. *Annual Review of Fluid Mechanics* 50.1 (2018), pp. 105–130. DOI: 10.1146/annurev-fluid-122316-050109 (Cited on p. 4).

[116] R. Saurel, F. Petitpas, and R. Berry. “Simple and efficient relaxation methods for interfaces separating compressible fluids, cavitating flows and shocks in multiphase mixtures”. *Journal of Computational Physics* 228 (2009), pp. 1678–1712 (Cited on p. 18).

[117] D. Schwendeman, C. Wahle, and A. Kapila. “The Riemann problem and a high-resolution Godunov method for a model of compressible two-phase flow”. *Journal of Computational Physics* 212 (2006), pp. 490–526 (Cited on p. 18).

[118] H. Stewart and B. Wendroff. “Two-phase flow: Models and methods”. *Journal of Computational Physics* 56.3 (1984), pp. 363–409. DOI: 10.1016/0021-9991(84)90103-7 (Cited on pp. 3, 18).

[119] M. Sýkora, M. Pavelka, I. Peshkov, P. Minakowski, V. Klika, and E. Romenski. “Comparison of the symmetric hyperbolic thermodynamically compatible framework with Hamiltonian mechanics of binary mixtures”. *Continuum Mechanics and Thermodynamics* (2024). DOI: 10.1007/s00161-024-01281-9 (Cited on p. 3).

[120] M. Tavelli, S. Chiocchetti, E. Romenski, A. Gabriel, and M. Dumbser. “Space-time adaptive ADER discontinuous Galerkin schemes for nonlinear hyperelasticity with material failure”. *Journal of Computational Physics* 422 (2020), p. 109758. DOI: 10.1016/j.jcp.2020.109758 (Cited on pp. 4, 31).

[121] M. Tavelli and M. Dumbser. “A staggered semi-implicit discontinuous Galerkin method for the two dimensional incompressible Navier–Stokes equations”. *Applied Mathematics and Computation* 248 (2014), pp. 70–92 (Cited on p. 40).

[122] M. Tavelli and M. Dumbser. “A staggered space–time discontinuous Galerkin method for the incompressible Navier–Stokes equations on two–dimensional triangular meshes”. *Computers and Fluids* 119 (2015), pp. 235–249 (Cited on pp. 38, 40).

[123] M. Tavelli and M. Dumbser. “A pressure-based semi-implicit space-time discontinuous Galerkin method on staggered unstructured meshes for the solution of the compressible Navier-Stokes equations at all Mach numbers”. *Journal of Computational Physics* 341 (2017), pp. 341–376 (Cited on p. 40).

[124] F. Thein, E. Romenski, and M. Dumbser. “Exact and Numerical Solutions of the Riemann Problem for a Conservative Model of Compressible Two-Phase Flows”. *Journal of Scientific Computing* 93 (2022), p. 83 (Cited on p. 5).

[125] A. Thomann and M. Dumbser. “Thermodynamically Compatible Discretization of a Compressible Two-Fluid Model with Two Entropy Inequalities”. *Journal of Scientific Computing* 97.1 (2023), p. 9. DOI: 10.1007/s10915-023-02321-3 (Cited on pp. 5, 15, 34, 61).

[126] E. Toro. *Riemann Solvers and Numerical Methods for Fluid Dynamics. A Practical Introduction, Third edition*. Berlin: Springer-Verlag, 2009 (Cited on pp. 4, 25, 36, 38).

[127] C. Truesdell. “Sulle basi della termomeccanica”. *Rendiconti della Classe di Scienze Fisiche, Mathematiche e Naturali* 22 (1957), p. 33 (Cited on pp. 2, 3).

[128] C. Truesdell and W. Noll. *The Non-Linear Field Theories of Mechanics*. Springer Berlin Heidelberg: Springer Berlin, Heidelberg, 2004. DOI: 10.1007/978-3-662-10388-3 (Cited on p. 3).

[129] B. van Leer. “Towards the Ultimate Conservative Difference Scheme V: A second Order sequel to Godunov’s Method”. *Journal of Computational Physics* 32 (1979), pp. 101–136 (Cited on p. 25).

[130] O. Zanotti and M. Dumbser. “Efficient conservative ADER schemes based on WENO reconstruction and space-time predictor in primitive variables”. *Computational Astrophysics and Cosmology* 3.1 (Dec. 2016), p. 1. DOI: 10.1186/s40668-015-0014-x (Cited on p. 24).

[131] C. Zhang and I. Menshov. “Using the composite Riemann problem solution for capturing interfaces in compressible two-phase flows”. *Applied Mathematics and Computation* 363 (2019), p. 124610. DOI: https://doi.org/10.1016/j.amc.2019.124610 (Cited on p. 4).

[132] C. Zhang and I. Menshov. “Eulerian Model for Simulating Multi-Fluid Flows with an Arbitrary Number of Immiscible Compressible Components”. *Journal of Scientific Computing* 83.2 (2020), p. 31 (Cited on pp. 4, 49).

[133] R. Zhao, O. Faltinsen, and J. Aarsnes. “Water entry of arbitrary two-dimensional sections with and without flow separation”. *21st Symposium on Naval Hydrodynamics* (1997) (Cited on pp. 52, 53, 54, 55).